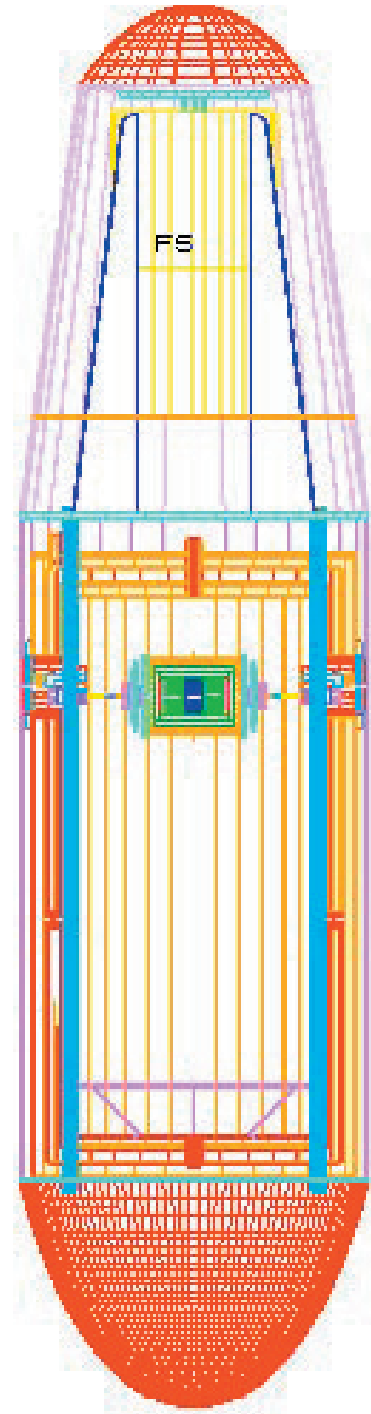# Chapter 2
Gravitation and Relativity

FS

TESTING THE EQUIVALENCE PRINCIPLE IN AN EINSTEIN ELEVATOR:

DETECTOR DYNAMICS AND GRAVITY PERTURBATIONS

E.C. Lorenzini[1,*], I.I. Shapiro[1], M.L. Cosmo[1], J. Ashenberg[1], G. Parzianello[2],

V. Iafolla[3] and S. Nozzoli[3]

[1]Harvard-Smithsonian Center for Astrophysics (CfA), Cambridge, Massachusetts;
[2]University of Padova (Padua, Italy) and CfA Visiting Student;
[3]Institute of Space Physics (Rome, Italy).
[*]Corresponding author e-mail: elorenzini@cfa.harvard.edu

Abstract

We discuss specific, recent advances in the analysis of an experiment to test the Equivalence Principle (EP) in free fall. A differential accelerometer detector with two proof masses of different materials free falls inside an evacuated capsule previously released from a stratospheric balloon. The detector spins slowly about its horizontal axis during the fall. An EP violation signal (if present) will manifest itself at the rotational frequency of the detector. The detector operates in a quiet environment as it slowly moves with respect to the co-moving capsule. There are, however, gravitational and dynamical noise contributions that need to be evaluated in order to define key requirements for this experiment. Specifically, higher-order mass moments of the capsule contribute errors to the differential acceleration output with components at the spin frequency which need to be minimized. The dynamics of the free falling detector (in its present design) has been simulated in order to estimate the tolerable errors at release which, in turn, define the release mechanism requirements. Moreover, the study of the higher-order mass moments for a worst-case position of the detector package relative to the cryostat has led to the definition of requirements on the shape and size of the proof masses.

Introduction

The scientific goal of the experiment is to test the equality of gravitational and inertial mass (i.e., to test the Principle of Equivalence) by measuring the independence of the rate of fall of bodies from their mass and composition. The experiment is accomplished by measuring the relative displacement (or equivalently acceleration) of two falling bodies of different materials which are the proof masses of a differential accelerometer. The experiment goal is to measure the Eötvös ratio $\delta g/g$ (differential acceleration/common acceleration) with an accuracy about two orders of magnitude better than presently achieved[i,ii]. The experiment is a null experiment in which a relative displacement different from zero, at the spin frequency, between the proof masses will indicate a violation of the Equivalence Principle.

In summary, the experiment consists in taking differential acceleration measurements with a high-sensitivity detector (the sensor) during free fall conditions lasting up to 28 s in a disturbance-free acceleration environment. A capsule is first released from the balloon at an altitude of typically 40 km and the detector is released from the top of the capsule immediately afterwards. During the measurement phase, the sensor free falls inside a 2-meters-long (in the vertical direction) evacuated cryostat (contained inside the capsule) that is falling simultaneously in the rarefied atmosphere[iii].

By falling in vacuum inside a co-moving capsule, the noise acceleration level can be kept to a negligible level while the signal strength in free fall, i.e., the full-strength Earth's gravity, is increased by 3 orders of magnitude with respect to the signals available to EP experiments conducted on the ground. The free fall technique, therefore, combines some of the advantages of the space-based tests with the accessibility and reusability of ground experiments.
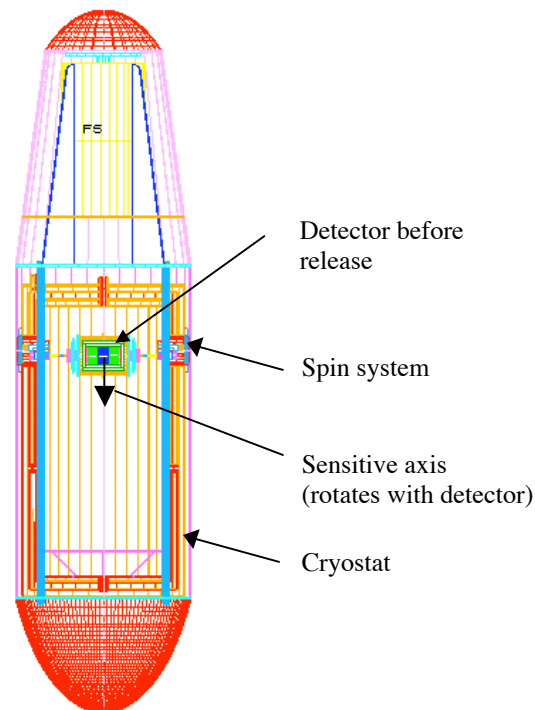

Figure 1 Schematic of capsule with detector attached (before release) to the spin up system

The detector has two sensing masses of different materials with their centers of mass (CM) as coincident as possible in order to reduce the effect of gravity gradients. The two masses are constrained in a way that they can move at low frequency along one axis (i.e., the sensitive axis that is perpendicular to the symmetry axis of the sensor) while they are rigidly constrained about the other two axes. The displacement of each sensing mass along the sensitive axis is detected by capacitive pickups which are parts of a measurement bridge.

2

One key feature is that the detector is spun before release about the symmetry axis that lies on the horizontal plane. The rotation provides the modulation (at the spin frequency) of any possible violation signal. Moreover, the spin provides gyroscopic stabilization of the detector during the fall and separates the signal from key noise components generated by the detector dynamics.

Frequency separation between the signal and the largest noise components is essential to the success of the experiment. The noise components that, unavoidably, appear at the signal frequency need to have a strength well below the detector threshold sensitivity. In the following, we analyze the detector dynamics to identify the frequencies of noise components that can be separated from the signal thanks to the appropriate selection of the inertia characteristics of the detector package. We also study the higher-order mass moments generated by the capsule mass and acting on the sensing masses. The higher-order mass moments contain some components at the signal frequency and care must be taken in designing the sensing masses in order to reduce the strength of those components to a negligible level.

<u>Analysis of Higher-order Mass Moments</u>

Overview

The sensing mass (test body), falling inside the capsule, is subjected to non-negligible gravitational attraction by the capsule. The higher-order gravitational potential plays a key role because of the elimination of the zero-order potential due to the Equivalence Principle. The model of perturbing gravitational mass consists of a spinning test body inside a capsule that is a hollow cylinder covered with flat caps. The test body is released at the symmetry axis of the cylinder, and deviates from the axis during its fall. Our goal is to compute the gravitational force and torque acting in the neighborhood of the fall trajectory. The fact that both the test mass and the capsule are closed finite bodies, increases the complexity of the problem. We are mostly concerned here with the harmonics of the force/torque at the modulation frequency as seen in the reference frame of the detector. In other words, our model should evaluate the force/torque in the rotating body frame of the sensing mass. For that purpose we built a semi-analytical model that can handle any configuration of test mass as well as any additional mass attached to the distributed mass of the capsule. Moreover, we exploited the fact that the size of the test mass is smaller than the cylinder radius to derive an asymptotic analytical solution.

There are at least three ways to approach the computation of the gravitational attraction between the capsule and the test body. The first approach is to compute the force between each capsule mass element and a test body mass element, and to perform a double summation on these forces. If N is the number of capsule mass elements, and N_B is the number of test body mass elements, then the cardinality of the computation (that drives the computational load) is $N \otimes N_B$. As it will become apparent later on, the mass discretization resolution required to the test body is very demanding and, consequently, the cardinality becomes prohibitively high with this approach. The second approach is a double integration over the bodies. The drawback of the first approach is

<div align="center">3</div>

the heavy computational effort, especially if the computation is needed as an online computation in a dynamical process. The weakness of the second approach is in the cumbersome analytical computation. The integration will require an asymptotic series expansion of complicated functions and asymptotic series introduce a truncation error into the computation. We adopted a third approach for the gravitational model.

We consider the capsule as a discrete ensemble of lumped mass, where the resultant force and torque acting on the test body are the cumulative force and torque due to the summation of all the capsule mass elements. The gravitational potential of the test body is expanded according to its increasing-order inertia characteristics. In other words, the interaction is between a finite body (the test mass) and a point mass. This approach is the result of a tradeoff between the previous approaches and its cardinality is N. The main advantage is the flexibility of modeling any capsule shape and the strongly reduced computational load.

The purpose of the following computation is to derive a closed-form analytical expressions, for the force and torque acting on the spinning test mass due to a capsule mass element.

Gravitational Model

The gravitational potential between finite size bodies, is:

$$V = -G \int_{\Re_o} \int_{\Re_B} \frac{dM_B}{r} dM_o \tag{1}$$

where $\Re_B$ is the test body (proof mass), and $\Re_0$ represents the attracting bodies, namely, the capsule or any other perturbing body.

For the purpose of simplicity we will proceed with a formulation of the test body and a single element of the attracting mass, M_i.

The gravitational potential at a representative element mass M_i due to the test body

is: $V(M_i) = -GM_i \int_{M_B} \frac{dM_B}{r}$, where $\vec{r}$ is the radius vector between a mass element

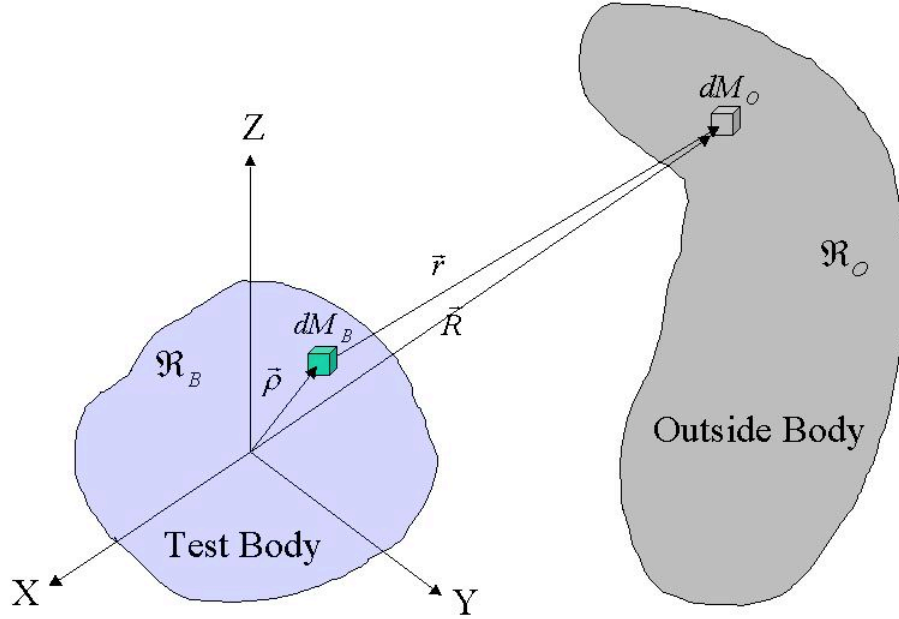of the test body and dM_o as shown in Fig. 2.

4

Figure 2 Gravitation model for test mass and outer attracting bodies

Assuming a sufficient discretization, the total force acting on the test body due to all external mass elements is $\vec{F}_B \cong \sum_{i=1}^{N} \nabla V(M_i)$, where N is the number of external mass elements. We first erect the following reference frames. The capsule frame, denoted by $\{X, Y, Z\}$ is attached to the capsule. X, Y lie on the equatorial plane and have an arbitrary azimuth while Z coincides with the symmetry axis of the capsule/cylinder. The test body frame, denoted by $\{x, y, z\}$, is attached to the test mass. The gravitational potential will be expressed in body frame. The inertia coefficients of the body are constant in this frame.

The derivation consists of the following steps: (1) substituting the inverse radius approximation into the potential; and (2) carrying out the integration. The position vectors in body frame are as follows:

$$\vec{R} = (l\, e_x + m\, e_y + n\, e_z)\, R \ \text{ and } \ \vec{\rho} = x\, e_x + y\, e_y + z\, e_z$$

where $\{e_x, e_y, e_z\}$ are body unit vectors, and $\{l, m, n\}$ are direction cosines between $\vec{R}$ and the body axes.

The resulting potential is a summation over all mass elements M_i (only the first 4 terms are shown for the sake of brevity):

5

$$V = \sum_{i=1}^{N} \{ -\frac{GM_1M_2}{R} - \frac{GM_1M_2}{R^2}[l\bar{x} + m\bar{y} + n\bar{z}]$$

$$-\frac{GM_1}{2R^3}[(3l^2-1)J_{xx} + (3m^2-1)J_{yy} + (3n^2-1)J_{zz} +$$

$$6(lm J_{xy} + ln J_{xz} + mn J_{yz})]$$

$$-\frac{GM_1}{2R^4}[l(5l^2-3)J_{xxx} + m(5m^2-3)J_{yyy} + n(5n^2-3)J_{zzz} \tag{2}$$

$$+ 3m(5l^2-1)J_{xxy} + 3n(5l^2-1)J_{xxz} + 3l(5m^2-1)J_{xyy}$$

$$+ 3n(5m^2-1)J_{yyz} + 3l(5n^2-1)J_{xzz} + 3m(5n^2-1)J_{yzz}$$

$$+ 6lmn J_{xyz}] + O(\frac{1}{R^5})\}$$

where $j_{x^p y^q z^r}$ are the inertia integrals defined as:

$$j_{x^p y^q z^r} = \int_{M_B} x^p y^q z^r \, dm \tag{3}$$

Expressions for the forces (shown in the following) are obtained by derivation of the potential. Torques (not shown here) are obtained by integrating over the proof mass the torque acting on a mass element of the body.

$$F_x = G \sum_{i=1}^{N} M_i \{ \frac{M_B l}{R_i^2} + \frac{M_B}{R_i^3}\left[(3l_i^2-1)\bar{x} + 3l_i m_i \bar{y} + 3l_i n_i \bar{z}\right]$$

$$+ \frac{1}{R_i^4}[(\frac{5}{2}\Gamma_i - I_{yy} - I_{zz} + 2I_{xx})l_i + 3m_i(5l_i^2-1)I_{xy} + 3n_i(5l_i^2-1)I_{xz} + 15l_i m_i n_i I_{yz}]$$

$$+ \frac{1}{R_i^5}[\frac{1}{2}(35l_i^4 - 30l_i^2 + 3)J_{xxx} + \frac{5}{2}(7m_i^2 - 3)l_i m_i J_{yyy} + \frac{5}{2}(7n_i^2 - 3)l_i n_i J_{zzz}$$

$$+ \frac{15}{2}(7l_i^2 - 3)l_i m_i J_{xxy} + \frac{15}{2}(7l_i^2 - 3)l_i n_i J_{xxz} + \frac{3}{2}(35l_i^2 m_i^2 - 5l_i^2 - 5m_i^2 + 1)J_{xyy}$$

$$+ \frac{15}{2}(7m_i^2 - 1)l_i n_i J_{yyz} + \frac{3}{2}(35l_i^2 n_i^2 - 5l_i^2 - 5n_i^2 + 1)J_{xzz} + \frac{15}{2}(7n_i^2 - 1)l_i m_i J_{yzz}$$

$$+ 3(7l_i^2 - 1)m_i n_i J_{xyz}] + H.O.T\}$$

6

$$F_y = G \sum_{i=1}^{N} M_i \{ \frac{M_B m_i}{R_i^2} + \frac{M_B}{R_i^3} \left[3l_i m_i \bar{x} + (3m_i^2 - 1)\bar{y} + 3m_i n_i \bar{z} \right]$$

$$+ \frac{1}{R_i^4}[(\frac{5}{2}\Gamma_i - I_{xx} - I_{zz} + 2I_{yy})m_i + 3l_i(5m_i^2 - 1)I_{xy} + 15l_i m_i n_i I_{xz} + 3n_i(5m_i^2 - 1)I_{yz}]$$

$$+ \frac{1}{R_i^5}[\frac{5}{2}(7l_i^2 - 3)l_i m_i J_{xxx} + \frac{1}{2}(35m_i^4 - 30m_i^2 + 3)J_{yyy} + \frac{5}{2}(7n_i^2 - 3)m_i n_i J_{zzz}$$

$$+ \frac{3}{2}(35l_i^2 m_i^2 - 5m_i^2 - 5l_i^2 + 1)J_{xxy} + \frac{15}{2}(7l_i^2 - 1)m_i n_i J_{xxz} + \frac{15}{2}(7m_i^2 - 3)l_i m_i J_{xyy}$$

$$+ \frac{15}{2}(7m_i^2 - 3)m_i n_i J_{yyz} + \frac{15}{2}(7n_i^2 - 1)l_i m_i J_{xzz} + \frac{3}{2}(35m_i^2 n_i^2 - 5m_i^2 - 5n_i^2 + 1)J_{yzz}$$

$$+ 3(7m_i^2 - 1)l_i n_i J_{xyz}] + H.O.T\}$$

(4)

$$F_z = G \sum_{i=1}^{N} M_i \{ \frac{M_B l}{R_i^2} + \frac{M_B}{R_i^3} \left[3l_i n_i \bar{x} + 3m_i n_i \bar{y} + 3(n_i^2 - 1)\bar{z} \right]$$

$$+ \frac{1}{R_i^4}[(\frac{5}{2}\Gamma_i - I_{xx} - I_{yy} + 2I_{zz})n_i + 15l_i m_i n_i I_{xy} + 3l_i(5n_i^2 - 1)I_{xz} + 3m_i(5n_i^2 - 1)I_{yz}]$$

$$+ \frac{1}{R_i^5}[\frac{5}{2}(7l_i^2 - 3)l_i n_i J_{xxx} + \frac{5}{2}(7m_i^2 - 3)m_i n_i J_{yyy} + \frac{1}{2}(35n_i^4 - 30n_i^2 + 3)J_{zzz}$$

$$+ \frac{15}{2}(7l_i^2 - 1)m_i n_i J_{xxy} + \frac{3}{2}(35l_i^2 n_i^2 - 5l_i^2 - 5n_i^2 + 1)J_{xxz} + \frac{15}{2}(7m_i^2 - 1)l_i n_i J_{xyy}$$

$$+ \frac{3}{2}(35m_i^2 n_i^2 - 5m_i^2 - 5n_i^2 + 1)J_{yyz} + \frac{15}{2}(7n_i^2 - 1)l_i n_i J_{xzz} + \frac{15}{2}(7n_i^2 - 3)m_i n_i J_{yzz}$$

$$+ 3(7n_i^2 - 1)l_i m_i J_{xyz}] + H.O.T\}$$

where H.O.T stands for higher-order terms and

$$\Gamma_i = (I_{yy} + I_{zz} - 2I_{xx})l_i^2 + (I_{xx} + I_{zz} - 2I_{yy})m_i^2 + (I_{xx} + I_{yy} - 2I_{zz})n_i^2$$

Note that the force has the following order of magnitude:

$$F \propto \sum_i G \frac{M_i M_B}{R_i^2} \{O(1) + O(\frac{\bar{\rho}}{R_i}) + O(\frac{L_B^2}{R_i^2}) + O(\frac{L_B^3}{R_i^3}) + H.O.T\}$$

Where L_B is a characteristic length of the test body with $\frac{L_B}{R_i} \ll 1$, and $\frac{\bar{\rho}}{R_i} \ll 1$.

Minimizing the higher-order effects

The goal is to minimize the gravitational forces acting on the test mass. The force equations reveal that the dominant term is the term corresponding to the second-order inertia. The offset term (dipole) is equal to zero for a reference frame centered at the body CM (see also later on). The direct way to minimize the forces is to require equal second-order moments of inertia. Then, the residual forces are due to mass imperfections and to higher-order (and smaller strength) inertia integrals. The purpose of the following discussion is to explore the effect of each term for a spinning test body.

First, we evaluate the mixed-inertia terms due to an imperfection. We assume that the imperfection is due to a disturbance in mass and/or length. The nominal test body could be a perfect cylinder, with radius R_B and length L_B. In order to minimize the force we require that $I_{XX} = I_{YY} = I_{ZZ}$. This constraint translates into a given aspect ratio of the cylinder as follows: $L_B = \sqrt{3}\,R_B$. Given the mass density, the mass or the size of the cylinder are now functions of a single free parameter. For example, given the mass, M_B, and the density, ρ_B, the length is: $L_B = \left(\dfrac{3M_B}{\pi \rho_B}\right)^{\frac{1}{3}}$

The similarity dimension of the k-order inertia is $[I] = \left[ML^k\right]$. Thus, the perturbed k-order inertia is $\delta I = L^k \delta M + kML^{k-1}\delta L$, or

$$\left[\frac{\delta I}{I}\right] = \left[\frac{\delta M}{M}\right] + k\left[\frac{\delta L}{L}\right]$$

Next, we consider the effect of the spin. The test body is spinning about its x-axis with a frequency that will be regarded as a fundamental frequency, or P1 (period one). We are primarily concerned with P1 because it is the frequency of the measured signal. For this purpose, we will analyze F_y by substituting the direction cosines, shown below, into the force expression.

The periodicity in time is introduced through the direction cosines that represent the orientation of the body frame relative to the capsule frame. The transformation between the two is:

$$\begin{bmatrix} x \\ y \\ z \end{bmatrix} = \begin{bmatrix} 1 & 0 & 0 \\ 0 & c\theta & s\theta \\ 0 & -s\theta & c\theta \end{bmatrix}\begin{bmatrix} X \\ Y \\ Z \end{bmatrix} \tag{5}$$

The resulting direction cosines are:

8

$$l = \frac{x}{R} = \frac{X}{R} \quad (independent \ of \ \theta)$$

$$m = \frac{y}{R} = \frac{Y c\theta + Z s\theta}{R} \tag{6}$$

$$n = \frac{z}{R} = \frac{-Y s\theta + Z c\theta}{R}$$

l becomes a cyclic function only if the body deviates from the X-axis.
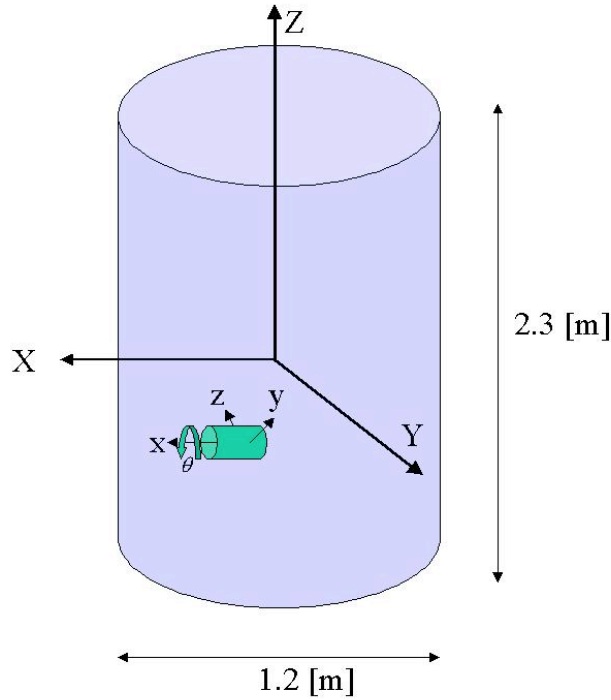

Figure 3 Reference frames

We compute the forces and torques acting on an imperfect proof mass placed at the worst location expected inside the capsule for conservative value of the wind shear (that is a point at –0.5 m below the capsule equator and 0.1 m off the centerline. The capsule consists of a hollow cylinder, covered by two flat caps with a total mass of 500 kg. The test body mass is 1 kg with sizes: $R_B = 0.0412\,m$ and $L_B = 0.0713\,m$. The geometrical and mass inhomogeneity errors, based on realistic assumptions, are: $\delta L/L = 10^{-4}$ and $\delta M/M = 10^{-4}$.

In the following plots (Figs. 4 and 5) we also show non-zero dipole terms (first-order inertia) to represent the fact the CM of one proof mass does not coincide with the CM of the other, thereby originating a non-null (gravity gradient) term when the difference of accelerations is taken between the two proof masses.
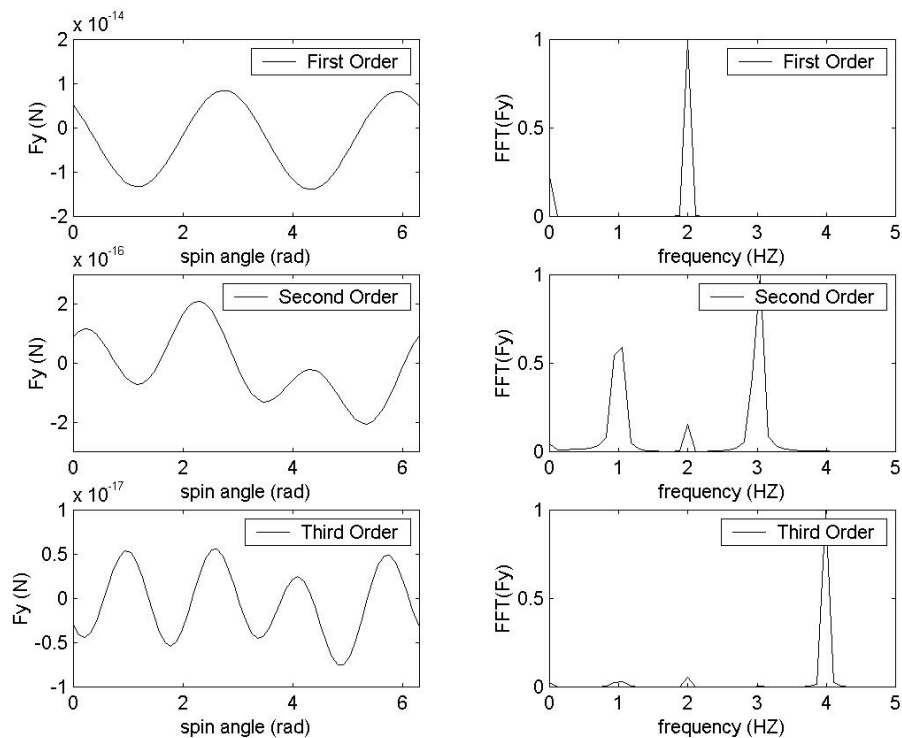
9

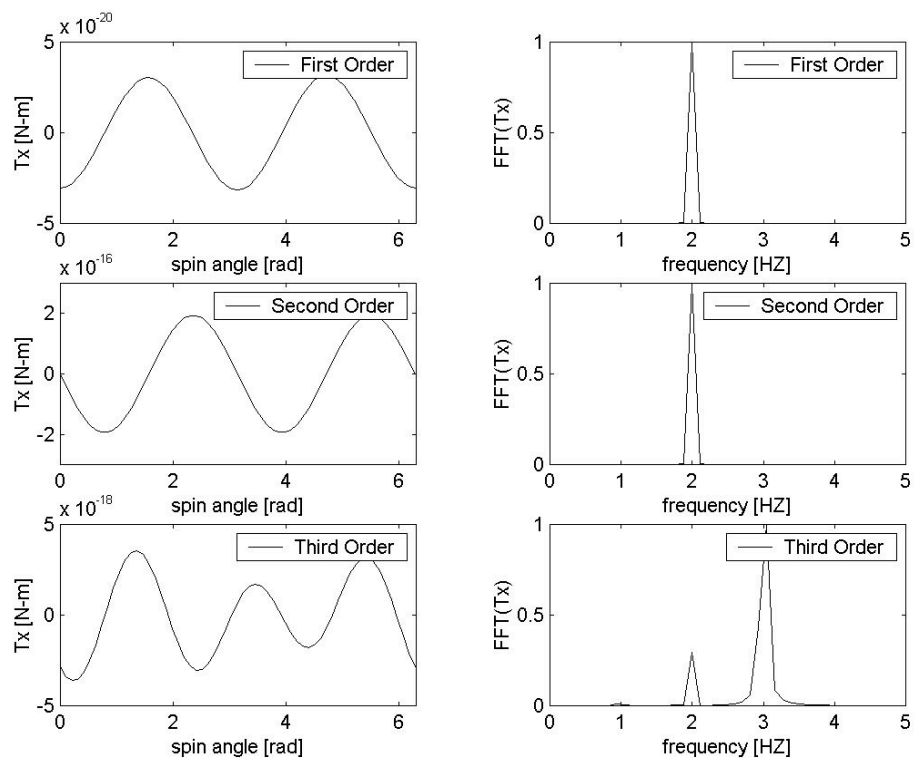**Figure 4** Ordered forces and spectra at expected worst location within the capsule

Figure 5 Ordered torques and spectra at expected worst location within the capsule

10

11

Similarity analysis

Another important issue is the role played by the test body mass and size. For this purpose we perform a similarity analysis, as shown in the following. We have formulated the gravitational potential as an asymptotic series in $1/R^n$. Each term in the series has an inertial tensor of degree $n - 1$. For example, the first term is of order n = 1 and its inertia tensor is of order 0 (the test body mass). The third term is of degree n = 3 and its inertia tensor is of order 2. This non-uniformity, however, introduces a problem when one computes the forces for a particular test mass and wants to deduct the forces for a different size of test mass. Mathematically speaking, if $F(M_{B1})$ and $F(M_{B2})$ are the forces due to two different test masses, then the ratio between the forces is not a homogeneous function, that is, $F(M_{B1})/F(M_{B2}) \neq g((M_{B1}/M_{B2})^m)$ where g is a function and m is the degree of the homogeneity. Note however that each term of the series is homogeneous by itself. For example, the first term is homogeneous of degree one, that is, the ratio between forces equals the ratio between the masses.

We will distinguish between two situations. The first situation is when the difference in masses is due to a different density. Since the forces are homogeneous of degree one in density, the ratio between the forces is equal to the ratio between the masses and the acceleration is constant. In a more interesting situation the density is the same, and the different mass is due to different sizes. In this case we need to apply a different similarity to each term. Let L and M be scaling factors for the length and the mass, respectively. If the density of different test bodies is the same, then $L \propto M^{1/3}$. Let $m = n - 1$ be the order of the moment of inertia, then its similarity dimension is $L^m M$, that is, $M^{1+m/3}$ or L^{m+3}. The acceleration similarity is $M^{m/3}$ or L^m. The following table summarizes the similarity dimension for each term in the potential.

Table 1 Similarity relations for the gravitational potential term

Potential Order $n;\ 1/R^n$	Inertia Order $m = n - 1$	Inertia Similarity	Acceleration Similarity
1	0	$M\quad (L^3)$	$1\quad (1)$
2	1	$M^{4/3}\ (L^4)$	$M^{1/3}\ (L)$
3	2	$M^{5/3}\ (L^5)$	$M^{2/3}\ (L^2)$
4	3	$M^2\quad (L^6)$	$M\quad (L^3)$
5	4	$M^{7/3}\ (L^7)$	$M^{4/3}\ (L^4)$

To summarize, given the force (or the acceleration) on a particular test body, we can deduct the force (acceleration) on another geometrically-scaled test mass. The acceleration ratio (of two different test masses with the same density) versus similarity dimensions (i.e., mass and length) is illustrated in Fig. 5.
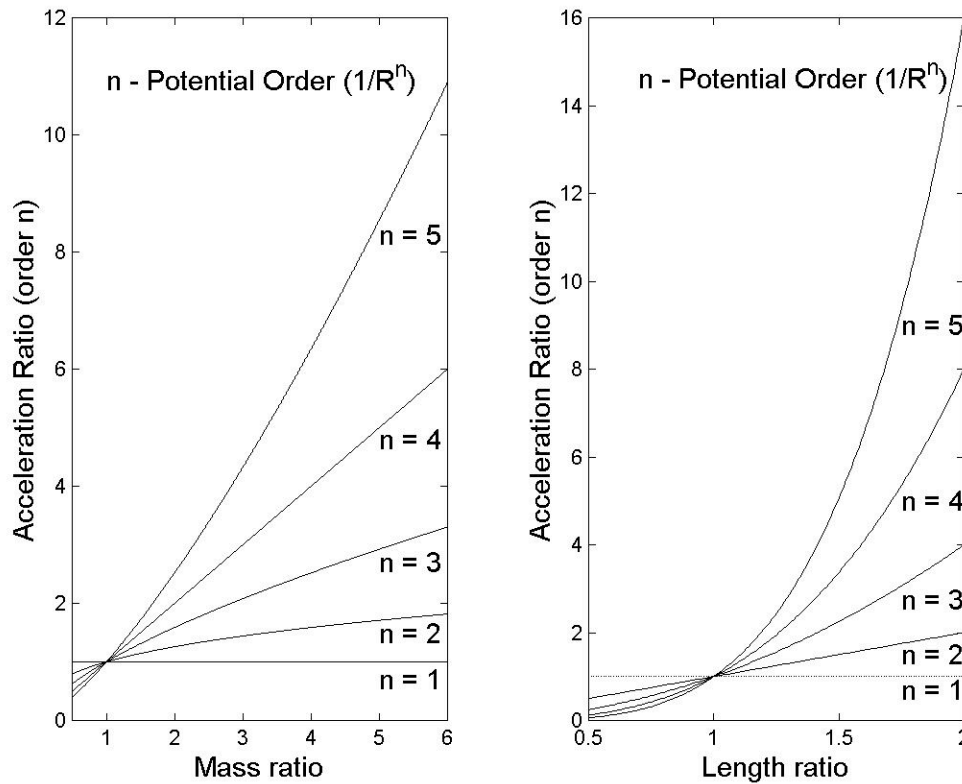
11

Figure 6 Scaling of test mass acceleration for masses with same density

The maximum potential order considered in our analysis is the hexadecapole (n = 5) which involves the fourth-order inertia integrals. We computed numerically the forces associated with the hexadecapole for a body with equal second-order inertia integrals (in order to minimize the quadrupole term). The results show that, at the worst expected location inside the capsule, the maximum acceleration associated with the hexadecapole term for a 1-kg proof mass is less than 10^{-16} g. In other words, for the accuracy goal of this experiment there is no need for belted cylinders[iv] (which would reduce the hexadecapole component even further). Proof masses with equal second-order inertia integrals (or alternatively moments of inertia), construction accuracy of order ten microns, and sizes smaller than about 10 cm are sufficient to make the contributions of all the higher-order gravity terms negligible.

<u>Detector Dynamics</u>

The instrument package dynamics also affects the differential accelerometer output. We derive the differential equations of motion for the detector in free fall (without gravity perturbations for the time being) and carry out numerical integrations for cases of interest. Those cases are associated with non-null offset positions of the centers of mass of the proof masses with respect to the CM of the instrument package and initial rotational velocity errors orthogonal to the spin velocity in order to evaluate the influence of those parameters on the differential output of the accelerometer.

Equations of motion

The sensor in its current, preliminary design (see Fig. 7) is composed of two sensing masses (A and B) having the CMs as coincident as possible with the CM of the external case. One proof mass has a dumbbell shape, while the other is a hollow cylinder. These two masses are constrained to the case C by means of elastic springs and they can pivot about an axis that is parallel to the axis of symmetry of the sensor. The whole detector is spun about the symmetry axis x.
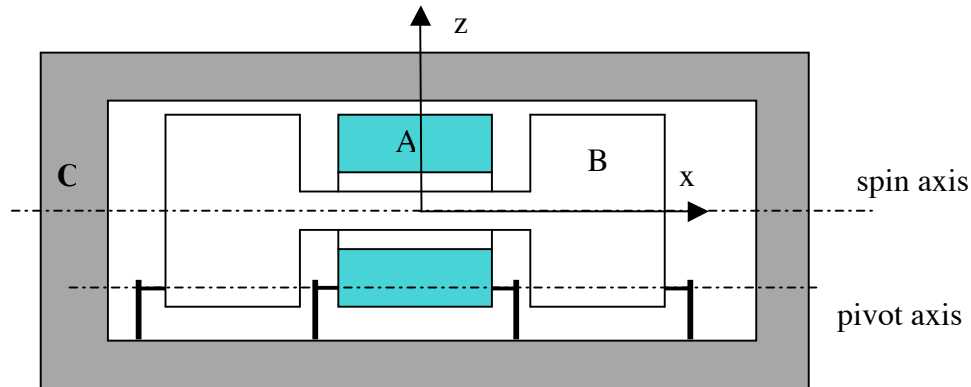

Figure 7 Schematic of three-body sensor

The motion of the sensor is essentially a rotation of the sensing masses about the pivot axis. The translational motion of the sensing masses, which depends on the high lateral stiffness of the springs is much smaller than the rotational motion. A rotation of the proof mass causes a variation of the distance between the sensing mass and the external case that changes the output capacitance.

Each body is modeled with six degrees of freedom, i.e., three translations and three rotations defined by Euler's angles. Elastic forces and torques are applied to each proof mass at the attachment points of the constraining springs. The transformation matrices have been written for each body in order to develop the equations of motion for the different bodies. The body coordinate systems are centered in the body's geometrical center, and are fixed with each body. The position of the CM is defined by three coordinates (x_{CMA}, y_{CMA}, z_{CMA} for body A) in the body reference frame. Each body frame has the x axis along the axis of symmetry which is also the spin axis. The y and z axes are radial axes that rotate with the body. The y axis is the sensitive axis of the accelerometer.

Translational accelerations

In the following we describe the procedure for deriving the equations of motion of one proof mass (A). The extension to a second proof mass is straight forward [v]. The CM vector in each body's reference frame is:

13

14

Body A: $\{r_A\} = \{x_{CMA} \ y_{CMA} \ z_{CMA}\}^T$

Body C: $\{r_C\} = \{x_{CMC} \ y_{CMC} \ z_{CMC}\}^T$

The translational acceleration expressed in the inertial reference is obtained by using the formula:

$$\{a_A\} = \left[\ddot{R}_{A0}\right] \cdot \{r_A\} + 2\left[\dot{R}_{A0}\right] \cdot \{\dot{r}_A\} + \left[R_{A0}\right] \cdot \{\ddot{r}_A\} + \left\{\ddot{R}_A^0\right\} \tag{7}$$

where $\{a_A\}$ is the acceleration of body A in the inertial frame, $[R_{A0}]$ is the rotation matrix from A to inertial frame, $\{r_A\}$ is the coordinates vector of body A CM in the A frame, $\{R_A^0\}$ is the translation vector expressed in inertial coordinates, and ($\cdot$) indicates matrix multiplication. Same-structure equations are used for the additional bodies.

Elastic Forces

To evaluate the elastic forces we define first the points where the springs are attached to each body. The position of these points are expressed in body frame. The distance between connected points is then computed from the actual position during the motion, projected in the A frame, and multiplied by the stiffness vector $\{k_{xA}, k_{yA}, k_{zA}\}$. By following this procedure, it is possible to assign different stiffness to each degree of freedom. The elastic forces are then projected in the inertial coordinate system as follows

$\{F_{1A}\} = [R_{A0}] \cdot ([K] \cdot (\{p_{A1}\} - [T_{0A}] \cdot \{T_{C0} \cdot p_{C1}\} - \{l_1\}))$

$\{F_{2A}\} = [R_{A0}] \cdot ([K] \cdot (\{p_{A2}\} - [T_{0A}] \cdot \{T_{C0} \cdot p_{C2}\} - \{l_2\}))$ (8)

$\{F_A\} = \{F_{1A}\} + \{F_{2A}\}$

where $[K]$ is the spring stiffness matrix, $\{p_A\}$ and $\{p_C\}$ are the vectors that define the positions of the spring attachment points, and $\{l_1\}$ and $\{l_2\}$ are the natural lengths of the springs. The operator "$T_{0A}.x$" indicates the combination of a multiplication by the rotation matrix $[R_{0A}]$ applied to the vector $\{x\}$ plus the translation of the vector $\{R_A^A\}$ which yields:

$\{T_{0A}.x\} = [R_{0A}] \cdot \{x\} + \{R_A^A\}$

The expression $T_{0A}.(T_{C0}.p_{C1})$ projects the coordinates of the point p_{C1} (expressed in the body C frame) onto the body A coordinate system. Subsequently, the force is projected onto the inertial frame using the $[R_{A0}]$ matrix. A similar procedure is used to evaluate the forces acting on any other body pairs.

The equations of translational motion for the two bodies A and C finally yield :

$m_A \{a_A\} - \{F_A\} = 0$

$m_C \{a_C\} - \{F_C\} = 0$ (9)

14

where m_A and m_C are the masses of body A and C, a_A and a_C the accelerations, and F_A and F_C the elastic forces:

$$\{F_A\} = \{F_{1A}\} + \{F_{2A}\}$$

$$\{F_C\} = \{F_{1C}\} + \{F_{2C}\}$$

The subscripts 1 and 2 identify the two springs that connect body A to C.

Rotational accelerations:

The angular velocity of each body is computed by using the rotation matrices that transform the coordinate system from the inertial to the body frame and, conversely, through the opposite transformation. The rotational velocity matrices of bodies A and C are derived by using the Cartan's formula as follows:

$$[\omega_A] = [R_{0A}] \cdot [\dot{R}_{A0}]$$
$$[\omega_C] = [R_{0C}] \cdot [\dot{R}_{C0}]$$

(10)

where $[R_{0A}]$ and $[R_{A0}]$ are the rotation matrices from the inertial coordinate system (denoted by 0) to the body reference frame of A and vice-versa. $[R_{0C}]$ and $[R_{C0}]$ are the correspondent matrices for body C. It should be noted that the former expression lead to the skew symmetric matrix of the angular velocity from which the components of the angular velocity vector $\{\omega_A\}$ can be readily extracted.

Elastic torques

The elastic torques acting on each body are computed by using the expressions for the locations of the attachment points and elastic forces previously defined. The expressions of the torques in the respective body reference frames are as follows:

$$\{T_A\} = \{p_{A1}\} \times ([R_{0A}] \cdot \{F_{1A}\}) + \{p_{A2}\} \times ([R_{0A}] \cdot \{F_{2A}\})$$

(11)

$$\{T_C\} = \{p_{C1}\} \times ([R_{0C}] \cdot \{F_{1C}\}) + \{p_{C2}\} \times ([R_{0C}] \cdot \{F_{2C}\})$$

where $\times$ indicates the external product of vectors.

Invoking Euler's equations, the rotational equations of motion yield:

$$[I_A] \cdot \{\dot{\omega}_A\} + [\omega_A] \cdot [I_A] \cdot \{\omega_A\} - \{T_A\} = 0$$
$$[I_C] \cdot \{\dot{\omega}_C\} + [\omega_C] \cdot [I_C] \cdot \{\omega_C\} - \{T_C\} = 0$$

(12)

where $\{\omega_A\}$ and $[\omega_C]$ represent the angular velocity vector and matrix, respectively, for body A (and similarly for body C). $[I_A]$ and $[I_C]$ are the inertia matrices for body A and C which, assuming principal axes, have diagonal forms. The equations of motion for the complete three-body detector are evaluated in the same way as for the two-body example

15

used previously leading to 3 vector equations for the rotational dynamics and 3 equations for the translational dynamics.

Numerical cases

Figure 8 shows the configuration of the 3-body sensor utilized for the numerical cases and the positions of the attachment points for the three-body sensor.
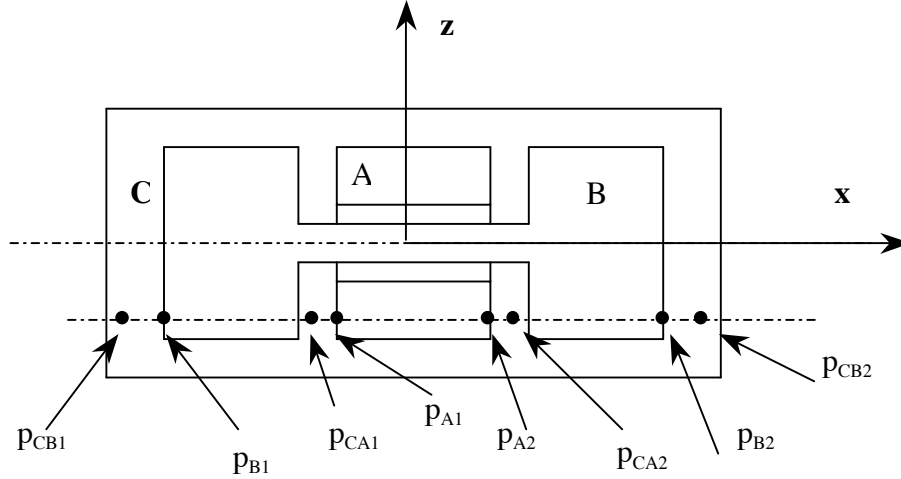

Figure 8 Attachment points of the proof masses

The points p_{CA1}, p_{CA2}, p_{CB1} and p_{CB2} are the points of the external body C connected to the points p_{A1}, p_{A2}, p_{B1}, p_{B2}, respectively. In this detector configuration, four springs are used to connect the two bodies to the external case (i.e., two springs per proof mass). The numerical value adopted for the numerical case shown in the following are as follows:

$m_A = 1$ kg, $m_B = 1$ kg, $m_C = 30$ kg;
$I_{Ax} = I_{Ay} = I_{Az} = 0.17$ kg-m^2; $I_{Bx} = I_{By} = I_{Bz} = 0.17$ kg-m^2;
$I_{Cx} = 0.95$ kg-m^2, $I_{Cy} = I_{Cz} = 1.46$ kg-m^2;
$k_{A1x} = 45000$ N/m, $k_{A1y} = k_{A1z} = 35000$ N/m;
$k_{A2x} = 45000$ N/m, $k_{A2y} = k_{A2z} = 35000$ N/m;
$k_{A\theta x} = 61.68$ Nm/rad, $k_{A\theta y} = k_{A\theta z} = 1000$ Nm/rad;
$k_{B1x} = 45000$ N/m, $k_{B1y} = k_{B1z} = 35000$ N/m;
$k_{B2x} = 45000$ N/m, $k_{B2y} = k_{B2z} = 35000$ N/m;
$k_{B\theta x} = 61.68$ Nm/rad, $k_{B\theta y} = k_{B\theta z} = 1000$ Nm/rad.

The initial conditions at release are: spin rate $\omega_x = 1.885$ rad/s (0.3 Hz), angular error at release $\omega_y = 10^{-2}$ rad/s; and initial nutation angle = 0. The CM offset errors are (with the reference frame placed at the geometrical center of body C):

$x_{CMA} = 10^{-6}$ m, $y_{CMA} = 0$, $z_{CMA} = 10^{-6}$ m;
$x_{CMB} = 0$, $y_{CMB} = 0$, $z_{CMB} = 0$;
$x_{CMC} = 0$, $y_{CMC} = 0$, $z_{CMC} = 0$

16

From the point of view of the rigid-body dynamics, a detector with the above inertia characteristics is a minor-inertia-axis spinner that exhibits a prograde precession.

The natural elastic frequency of the detector are shown in Figure 9. The lowest frequency (at 2.999 Hz) corresponds to the differential torsional mode of the proof masses while the next one (at 3.486 Hz) corresponds to the common-mode torsional frequency.

$$
\begin{array}{ll}
2.999 & 42.108 \\
3.486 & 42.554 \\
4.349 & 43.489 \\
4.399 & 44.075 \\
26.779 & 48.344 \\
27.217 & 50.062
\end{array}
$$

Torsional differential mode

Torsional common mode

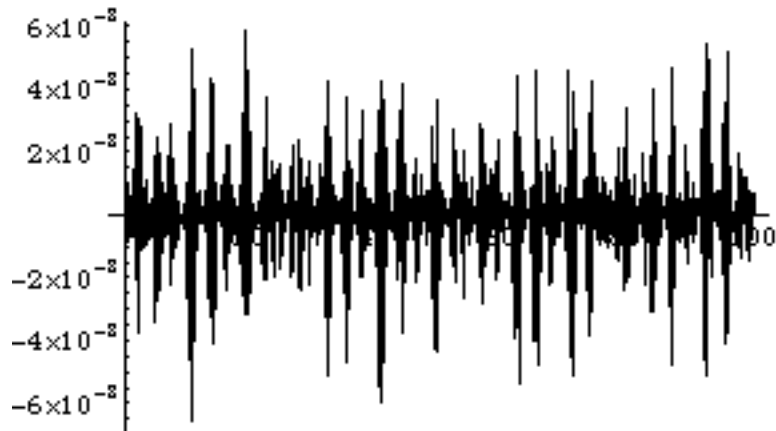**Figure 9** Natural frequencies

Figure 10 $y_A - y_B$ (m) in body frame vs. time (s)

17

18
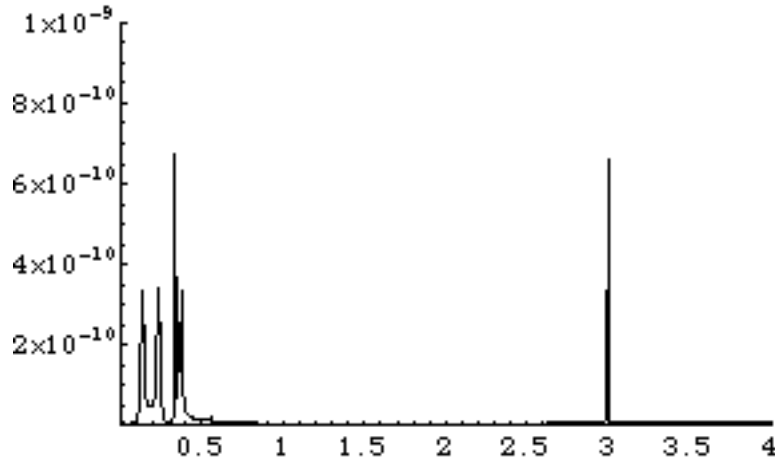
Figure 11 FFT of y_A - y_B (m) vs. frequency (Hz)
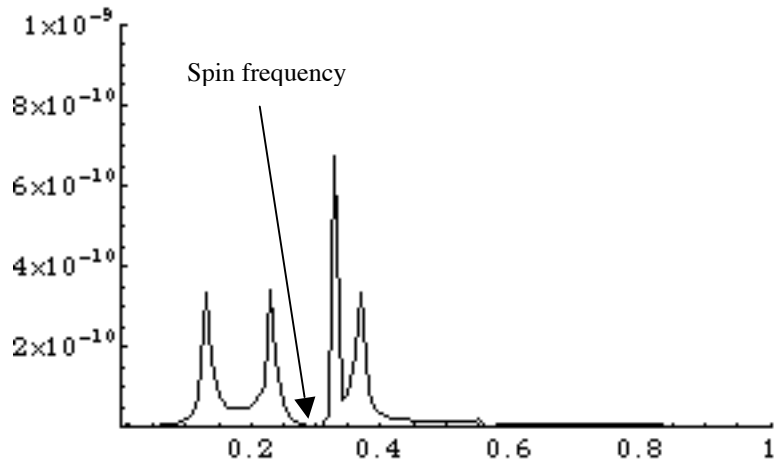
Figure 12 Zoom of y_A - y_B (m) FFT vs. frequency (Hz)

Figure 10 is a time profile of the differential displacement between the two proof masses, that is measured by the capacitive pickups. The displacement is then converted into acceleration through the accelerometer's transfer function. The initial conditions adopted for release are conservatively large and no post-release phase with oscillation damping was included in this simulation leading to conservative values of the differential displacements. Here we are mostly concerned with the frequency content of the differential displacement which is shown in Fig. 11 and, with an expanded view, in Fig. 12. Figure 11 shows the separation between the oscillations related to the rigid-body dynamics of the instrument package (at low frequency) and the first elastic frequency of the accelerometer. More importantly, Fig. 12 shows that the precession frequency can be chosen so that the harmonics related to the rigid-body dynamics do not overlap with the spin frequency (which is also the signal frequency).

The precession of the instrument package will be caused by an angular rate error (perpendicular to the spin axis) at release or an imperfect inertial balancing of the instrument package. Effects of the precession are detected by the accelerometer if the centers of mass of the proof masses do not coincide with the center of mass of the instrument package. If we choose the moments of inertia of the instrument package so that the precession frequency is non-commensurate with the spin frequency, then there are no dynamics-related harmonics at the signal frequency. Consequently, we must simply guarantee that the precession-related accelerations are smaller than the end-of scale of the detector. These conditions are met for a prograde precession (minor-axis spinner), angular rate errors at release smaller than about 0.1 deg/s, and realistic construction accuracies of the detector.

Conclusions

Our analysis concludes that the gravitational perturbations, acting on the test masses and due to the capsule gravity, can be reduced to within the limit required by the experiment if the test mass design abides to simple rules as follows:

a) The test masses must be smaller than a characteristic size of about 10 cm;
b) The second order principal moments of inertia must be equal within construction tolerances ($\delta L/L < 10^{-4}$);
c) The density uniformity of the test mass must be within 0.01% ($\delta M/M < 10^{-4}$).

There is no need for belted cylinders (used in the STEP satellite experiment) for the accuracy goal of our experiment.

With reference to the detector free-fall dynamics, the ratio of the moments of inertia of the instrument package must be such that the body precession frequency is non-commensurate with the spin frequency. Similarly, none of the elastic frequencies of the detector must overlap with the spin frequency. These conditions guarantee that no acceleration components related to the detector elastic and rigid-body dynamics overlap with the signal frequency.

Acknowledgements

References

[i] Baessler, S., B. Heckel , E. Adelberger, J. Gundlack , U. Schmidt and E. Swanson, *Phys Rev Lett.,* Vol. 83, 1 Nov. 1999.

[ii] Williams, J.G., X.X. Newhall and J.O. Dickey (1996), Relativity parameters determined from lunar laser ranging, *Phys. Rev. D*, 53, 6730.

[iii] Lorenzini, E.C., I.I. Shapiro, F. Fuligni, V. Iafolla, M.L. Cosmo, M.D. Grossi, P.N. Cheimets and J.B. Zielinski, "Test of the Weak-Equivalence Principle in an Einstein Elevator." Il Nuovo Cimento, Vol. 109B, No. 11, 1994.

[iv] Lockerbie, N.A., A.V. Veryaskin and X. Xu, "Differential gravitational coupling between cylindrically-symmetric, concentric test masse and arbitrary gravitational source: relevance to the STEP experiment." Classic and Quantum Gravity, Vol. 10, 2419-2430, 1993.

[v] Shapiro, I.I., et al. "Test of the Equivalence Principle in an Einstein Elevator." Annual Report#2, NASA Grant NAG8-1780, June 2003.

Engineering Developments for the Primary Atomic Reference Clock in Space (PARCS)

April 16, 2003

Dave Brinza
Jet Propulsion Laboratory, California Institute of Technology

Measurement of the Aberration of Gravity Using Jupiter's Motion

Edward B. Fomalont
National Radio Astronomy Observatory

On September 8, 2002 Jupiter passed within 3.7' of the bright radio source, J0842+1835. The deflection predicted by General Relativity (GR) of this source at closest approach contains two major terms: an outward radial deflection from Jupiter of 1190 μarcsec, and a deflection of 51 μarcsec associated with the aberration of gravity. We used the Very Long Baseline Array with the Effelsberg telescope to measure the position of J0842+1835 with respect to two quasars a few degrees away during the period of September 4-12. With the use of two quasars on opposites sides of the radio source, we removed most of the tropospheric delay variations, and obtained the deflection of J0842+1835 on September 8 to an accuracy <10 μarcsec. The aberrational part of the deflection that we measured is 0.98 +/- 0.19 times that predicted by GR. The speed of gravity associated with the measured aberration of the gravitational field of Jupiter is (1.06 +\- 0.21) times the speed of light.

Science Goals of the Primary Atomic Reference Clock in Space (PARCS) Experiment.

N. ASHBY

Department of Physics, University of Colorado, Boulder, CO 80309-0390 USA
E-mail: n_ashby@mobek.colorado.edu

The PARCS (Primary Atomic Reference Clock in Space) experiment will use a laser-cooled Cesium atomic clock operating in the microgravity environment aboard the International Space Station (ISS) to provide both advanced tests of gravitational theory and to demonstrate a new cold-atom clock technology for space. PARCS is a joint project of the National Institute of Standards and Technology (NIST), NASA's Jet Propulsion Laboratory (JPL), and the University of Colorado (CU). This paper concentrates on the scientific goals of the PARCS mission. The microgravity space environment allows laser-cooled Cs atoms to have Ramsey times in excess of those feasible on Earth, resulting in improved clock performance. Clock stabilities of 5×10^{-14} at one second, and accuracies better than 10^{-16} are projected. The relativistic frequency shift should be measureable at least 35 times better than the previous best, Gravity Probe A.[1] PARCS is scheduled for launch in 2007 and will probably fly with the Stanford Superconducting Microwave Oscillator (SUMO), which will allow a Kennedy-Thorndike type experiment with an improvement of about three orders of magnitude compared to previous best results. PARCS will also provide a much-improved realization of the second, and a stable time reference in space. Significant improvements in testing fundamental assumptions of relativity theory, and in testing non-metric theories of gravity, are expected.

1 Introduction

The PARCS laser-cooled atomic clock takes advantage of the microgravity environment of space to achieve improvements in clock performance. We describe here the scientific and technical measurements to be performed with PARCS.

1.1 Gravitational Measurements

Relativity predicts how clocks behave while moving or in varying gravitational fields. The PARCS clock will be used to test such predictions. Improvements in relativistic frequency shift measurements by nearly two orders of magnitude, and improvements in Kennedy-Thorndike type tests at an even higher level are expected. Earth-based tests of Local Position Invariance (LPI) have recently improved significantly.[2] Space-based tests of LPI therefore no longer offer important improvements, but can complement such earth-based tests with clocks of different structures, in a different environment. These measurements

1

provide a basis for possible future gravitational experiments in highly elliptical earth orbit or for a solar probe.

1.2 Other Technical Measurements

The PARCS clock will realize the second's definition approximately ten times more accurately than that now done on earth. It can provide accurate time interval and frequency signals to laboratories worldwide, thus contributing to the coordination of clocks maintained by standards laboratories around the world. Since the ISS will be above the troposphere and part of the ionosphere, propagation-delay variations for signals traveling between GPS satellites and the ISS will be smaller than those observed on earth. PARCS provides an opportunity to study the clocks, ephemerides, and propagation delay mechanisms in GPS with high precision.

1.3 Atomic Clocks in Microgravity

Earth-based clocks using neutral atoms are limited in accuracy by strong gravitational forces which pull atoms downward out of the apparatus and limit the interaction time over which their resonance frequency can be measured. On earth this time limit, attained in laser-cooled cesium-fountain clocks, is about one second.[3] In the ISS microgravity environment, atom-observation time will be increased by an order of magnitude or more. The resonance linewidth decreases as observation time increases, which simplifies locating the center of the resonance. Many systematic frequency shifts scale as the observation time, so accuracy is improved. We project a fractional frequency uncertainty of 5×10^{-17} (for an averaging time of the order of 10 days) for PARCS. The best earth-based atomic clocks have an uncertainty of order 1×10^{-15} [3,4,5].

The best configuration for a very slow-atom clock in space is the same as that of the traditional atomic-beam clock, but the space clock will involve balls of laser-cooled atoms rather than a continuous beam of thermal atoms. At the projected stability $\sigma_y(\tau) = 5 \times 10^{-14} \tau^{-1/2}$, the projected accuracy of the PARCS clock cannot be achieved without the ISS microgravity environment.

1.4 Concurrent Flight with Other Experiments

Concurrent flight with other clock experiments would provide opportunities for useful comparisons among clocks of different structures. Stanford's superconducting microwave oscillator (SUMO) is scheduled to fly with PARCS. Other possibilities include RACE, a rubidium atomic-clock experiment; ACES,
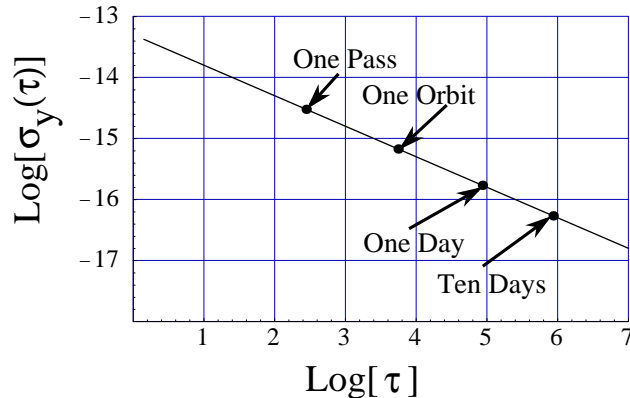
2

Figure 1: Allan deviation of the PARCS cesium clock showing averaging times τ (in seconds) needed to achieve various measurement uncertainties.

Europe's Atomic Clock Ensemble in Space; the cooled-sapphire oscillators developed at JPL and the University of Western Australia; and the linear-ion clock developed at JPL. In particular, concurrent flight of PARCS and SUMO will allow a Kennedy-Thorndike experiment with a projected performance 770 times greater than previously achieved on earth. A slight improvement in the Michelson-Morley experiment can also be achieved.

2 Experimental Objectives

Relativistic effects on clocks in low-altitude earth orbits can be characterized by the orders of magnitude of the fractional frequency shift they cause. For example, first-order Doppler shifts are of order $v/c \approx 10^{-5}$ for an orbiting clock, where v is the spacecraft speed in a local, freely-falling, earth-centered inertial frame and c is the defined speed of light. If Φ represents the Newtonian gravitational potential at the location of the clock, then gravitational frequency shifts and second-order Doppler shifts are of order $\Phi/c^2 \approx (v/c)^2 \approx 10^{-10}$. The data analysis technique that is planned for PARCS is discussed in the Appendix. It uses only even-order terms; fortunately fourth-order terms are negligible. Fig. 1 shows the projected Allan Deviation of PARCS as a function of averaging time τ. The absolute uncertainty is projected to be 5×10^{-17}, after about 12 days of averaging. We assume a time-transfer uncertainty (to the earth) with a stability of 220 ps over at least 12 days. We assume the following orbital parameters: altitude 400 km, inclination 51.6°, and eccentricity 0.001. Then one pass over a fixed ground station takes about 400 s. The orbital period

3

is about 5500 s, and during 1 day the satellite will be in position to exchange direct transmission with a single ground-based reference during four or five passes. During a single pass, the time available for direct frequency comparison with a ground-based reference clock is not sufficient to realize the full capability of the PARCS clock. Frequency comparisons are instead expected to use GPS satellites as intermediaries, which do not require such line-of-sight exchange.

2.1 Measurement of the Gravitational Frequency Shift

Here the space-borne clock's frequency is compared with the frequency of a clock on the earth employing a measurement of the accumulated phase of the orbiting clock (see Appendix). Accumulated phase measurements make best use of the long-term stability of the space-borne clock.

The ISS altitude is only about 400 km, so the second-order Doppler shift is the dominant contribution to the net frequency shift. The fractional frequency shift due to second-order Doppler (time dilation) is approximately 3×10^{-10}, while that due to gravitation is about 4×10^{-11}. Significant contributions come from the monopole potential of the earth, the quadrupole moment ($\approx 3 \times 10^{-14}$) and a few higher moments. The Stokes coefficients are known sufficiently well known[6] that uncertainties in a frequency-shift test, arising from uncertainties in the Stokes coefficients, are negligible.

One pass is too brief to yield scientifically significant new results with direct frequency comparison to an earth-bound standard. However, with the accumulated-phase measurement method, the long-term stability of the clock can be used to advantage, since many passes over the ground station, lasting for days, are available for the measurement. Fig. 2 shows the results of a covariance analysis for this experiment in which time transfer errors, clock stability, tracking errors, and inaccuracy of the ground clock used for comparison have been accounted for. If the experiment lasts only a few hundred seconds, the uncertainty in determining the fractional frequency shift is dominated by the time-transfer uncertainties. Eventually these become small compared to clock instabilities. At long times, the uncertainty of less than 2 parts per million is dominated by the inaccuracy of the ground clock (frequency uncertainty of 5×10^{-16}). The level at which the corresponding test of GR was achieved in Gravity Probe A was 70 parts per million,[1] so the proposed experiment should result in improvement of measurement of the total gravitational frequency shift by between one and two orders of magnitude. To obtain this result, satellite position uncertainties of less than 50 cm must be achieved.
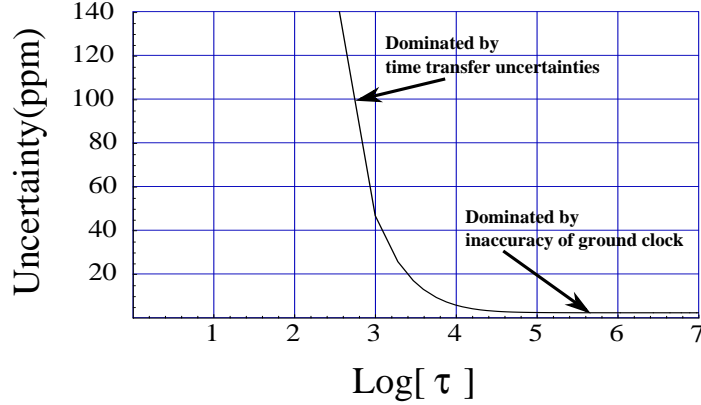
4

Figure 2: The total measurement uncertainty as a function of averaging time τ (in seconds) for the total frequency shift using the accumulated-phase measurement method. Beyond about 10^5 seconds, the uncertainty in the measurement drops below a value of 2 ppm.

2.2 Second-Order Doppler Shift

Measurement of the second-order Doppler shift would test Local Lorentz Invariance (LLI), at an uncertainty comparable to that of the best previous test. In the Mansouri-Sexl test theory of special relativity,[7] the time dilation terms are multiplied by a coefficient α, where it is currently known that $\alpha = -1/2 \pm (1 \times 10^{-6})$, a result obtained using fast ^{20}Ne atoms.[8] This experiment will probe the effect in a different parameter range.

2.3 Test of Local Position Invariance (LPI)

LPI implies that two clocks of different structure but equal frequencies should suffer identical frequency shifts when moved together through a gravitational field. For such tests the longer-term stability of the clocks is relevant, rather than accuracy. The same control of systematic effects that yields high accuracy also leads to high stability. LPI can still be tested with stable, (but possibly inaccurate) clocks by studying variations in frequency differences as the orbit radius and orbital speed vary. A highly eccentric orbit is most desirable. If LPI is violated, then for nearby clocks A and B $\Delta f/f = c_{AB}\Delta\Phi/c^2$, where $\Delta\Phi$ is the change in the gravitational potential of the clocks, $\delta f = f_A - f_B$, and $f = f_A \approx f_B$. In general relativity (GR) the coefficient c_{AB} is exactly zero. A recent experiment, lasting many months, made use of variations in the sun's potential arising from earth's orbital eccentricity.[2] An upper limit $c_{AB} \leq$

5

2.1×10^{-5} was obtained, a significant improvement over the previous best[9]. For a clock on the ISS, one may expect a variation in earth's gravitational potential of $\approx \delta\Phi/c^2 \approx 1.3 \times 10^{-12}$. If the comparison between clocks can be performed at the full stabilities of PARCS and SUMO, then the value of c_{AB} can be tested in 30 days at a level such that the error in c_{AB} is

$$\Delta c_{AB} < 9 \times 10^{-6}\,. \tag{1}$$

This is only a small improvement, but complements the earth-based experiments by using clocks of markedly different internal structure. A larger orbital eccentricity for the ISS would benefit this comparison even more.

2.4 Kennedy-Thorndike Experiment

For this experiment, the laser-cooled cesium clock is compared to a clock (such as SUMO) with a resonance based on the length of the oscillator cavity. This oscillator is analogous to an arm of an optical interferometer. As the spacecraft turns, the oscillator cavity turns, and the frequency of the resonance could be influenced by any spatial anisotropy in the speed of light. In contrast, the cesium frequency is not expected to change since any cavity pulling associated with changes in the microwave cavity of this clock is negligible. Comparison of the cesium frequency with that of SUMO thus tests for spatial anisotropy.

Mansouri and Sexl's [7] theory provides a basis for analysis of interferometer experiments testing local Lorentz invariance. Stability, not accuracy, of the laser-cooled clock for an orbital period is crucial in performing such tests. Also, one can hope to reach a precision better than the absolute uncertainty of the clock (5×10^{-17}) because the signals have a characteristic signature due to orbital motion that can be used to average down the noise over many orbits.

Assuming the existence of a preferred frame (e.g., one at rest with respect to the cosmic microwave background radiation), in which the speed of light is isotropic, then in a laboratory moving with velocity $\mathbf{v}$ relative to this frame, the two-way speed of light propagating at angle θ from $\mathbf{v}$ is given by

$$c(\theta)/c = 1 + (1/2 - \beta + \delta)v^2/c^2 \sin^2\theta + (\beta - \alpha - 1)v^2/c^2\,, \tag{2}$$

where α, β, and δ are parameters (to be studied experimentally) introduced in the Mansouri and Sexl test theory. In special relativity the time dilation parameter $\alpha = -1/2$; the Lorentz contraction parameter $\beta = 1/2$; and $\delta = 0$. (δ describes contraction normal to $\mathbf{v}$.) The light speed $c(\theta)$ in Eq. (2) determines the frequencies of a local cavity oscillator of fixed length L.

6

The parameter $(\beta - \alpha - 1)$ is measured in a Kennedy-Thorndike experiment. The square of the clock's velocity relative to the preferred frame should be

$$\mathbf{v}^2 = (\mathbf{v}_{sun} + \mathbf{v}_{earth} + \mathbf{v}_{sat})^2 \tag{3}$$

where the terms on the right side of Eq. (3) are respectively, the velocity of the sun relative to the preferred frame (which could be taken to be 377 km/s derived from the anisotropy of the cosmic background blackbody radiation), plus the velocity of the earth relative to the sun, plus the velocity of the satellite relative to earth. The coefficient of the last term in Eq. (2) can be quite significant. One contribution to the fractional frequency shift of the cavity oscillator is a cross term in the expansion of Eq. (3), giving rise to

$$\frac{\Delta f}{f} = (\beta - \alpha - 1)\frac{2\mathbf{v}_{sun} \cdot \mathbf{v}_{sat}}{c^2} . \tag{4}$$

The time signature of such a term is highly correlated with that of the change of potential which is of interest in testing LPI. There it is the change in the earth's (or the sun's) gravitational potential that drives the effect. Here, it is the orientation of $\mathbf{v}_{sat}$ relative to $\mathbf{v}_{sun}$ that drives the effect. These two relativistic effects should be separable since they differ in phase.

Currently, the combination of parameters $(\beta - \alpha - 1)$ is only known experimentally to be $< 6.6 \times 10^{-5}$.[10] If an upper limit of 5×10^{-16} (assumed stability of the cavity oscillator at 5500 s) can be put on the frequency change of Eq. (4), and we assume that $\mathbf{v}_{sun} \approx 377$ km/s, then a limit of order $(\beta - \alpha - 1) < 9 \times 10^{-10}$ results, an improvement by almost three orders of magnitude. A limit on α provides independent confirmation of the special relativity predictions of time dilation. Smaller upper limits on the parameters α, β, and δ will help in eliminating some preferred frame theories.

2.5 Michelson-Morley (MM) Experiment

In a MM type experiment, the θ-dependent term in Eq. (2) is measured. This can be done using the slow rotation of the spacecraft in its orbit, which naturally changes while the laser-cooled cesium clock provides frequency memory. The fractional frequency shift for a 90° rotation starting from θ_0 is $(1/2 - \beta + \delta)v^2/c^2 \cos(2\theta_0)$. One cross-term in the expansion of v^2 varies with the orbital period. Placing an upper limit of 5×10^{-17} on such a term would lead to $(1/2 - \beta + \delta) < 1.5 \times 10^{-9}$, slightly better than the previous best result.[11] This experiment has the advantage of a much larger orbital velocity than the velocity due to earth rotation in an earth-bound experiment.

7

Table 1: Summary of science objectives for the PARCS mission

Measurement/Test	Expected Uncertainty	Previous Best Uncertainty	Improvement (Ratio)
Net Frequency Shift, $\Delta f/f$	1.7×10^{-6}	70×10^{-6}	35
Gravitational Frequency Shift, $\Delta f/f$	12×10^{-6}	140×10^{-6}	12
Kennedy-Thorndike, $\beta - \alpha - 1$	9×10^{-10}	6.9×10^{-7}	770
Local Position Invariance, c_{AB}	9×10^{-6}	2.1×10^{-5}	2.3
Michelson-Morley, $\frac{1}{2} - \beta + \delta$	5×10^{-10}	5×10^{-9}	10
Atom Drift Time, s	10	1	10
Most Accurate Space Clock, $\Delta f/f$	5×10^{-17}	1×10^{-12}	20,000
Realization of the Second, $\Delta f/f$	5×10^{-17}	1.2×10^{-15}	24

2.6 Realization of the Second

In an earth-based cesium clock, gravity simply pulls the atoms out of the apparatus. The linewidth of the observed transition is then broader, limiting the determination of the resonance center. Also, the atoms in an earth-based clock must move at higher velocities relative to the clock enclosure where the Doppler shift and several other velocity-dependent systematic shifts are larger and more difficult to evaluate. In microgravity, atoms can be launched much more slowly, increasing the observation time by an order of magnitude and reducing the uncertainty in realization of the second by a comparable amount.

2.7 The $TH - \epsilon\mu$ Theory of Lightman and Lee

In the $TH - \epsilon\mu$ theory, charged massive particles in a spherically symmetric gravitational field couple to "gravitationally modified" electromagnetic field equations. To leading order, predictions of gravitational frequency shifts and violations of LPI are expressed through two parameters Γ_0 and Λ_0.[12,13] For example, when comparing the frequencies of a superconducting cavity-stabilized clock and a Hydrogen maser moving together through a varying gravitational potential, $c_{AB} = 3(\Gamma_0 - \Lambda_0)/2$. For clocks at different locations, $\Delta f/f = (1 - 3\Gamma_0 + \Lambda_0)\Delta\Phi/c^2$. The PARCS measurements should give significantly improved upper limits on these two linear combinations of parameters.
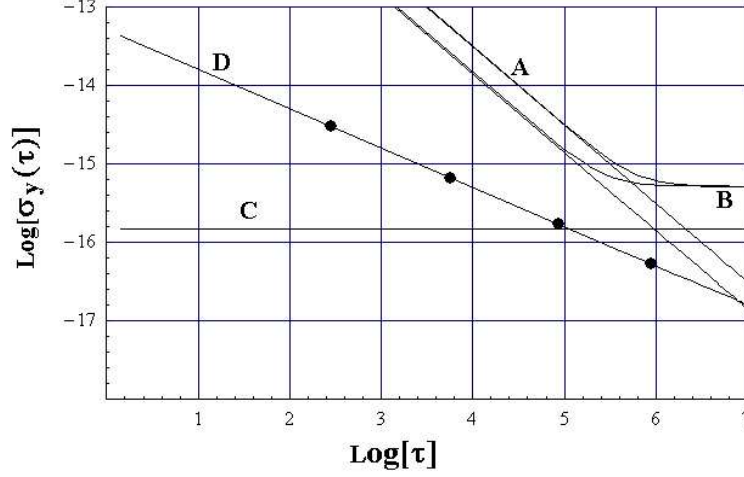
8

Figure 3: Allan variance plot of the stability limits for PARCS. See the text for a description of the different curves. The long-term limit of curve B is determined by the inaccuracy of the ground clock.

2.8 Realization of the Second

In an earth-based cesium clock, gravity simply pulls the atoms out of the apparatus. The linewidth of the observed transition is then broader, limiting the determination of the resonance center. Also, the atoms in an earth-based clock must move at higher velocities relative to the clock enclosure where the Doppler shift and several other velocity-dependent systematic shifts are larger and more difficult to evaluate. In microgravity, atoms can be launched much more slowly, increasing the observation time by an order of magnitude and reducing the uncertainty in realization of the second by a comparable amount.

It is difficult to transfer frequency between laboratories at the accuracy of the best earth-bound standards, so real-time access to the highest accuracy frequency references is limited. PARCS should outperform its earth-based counterparts by an order of magnitude. The best current realization of the second on earth has an uncertainty of 1.4×10^{-15} [3]. The projected uncertainty for the proposed space clock is 5×10^{-17}. Transfer of the second at this accuracy assumes that GR is correct, in order to correct for clock frequency shifts. At this level, uncertainties in our knowledge of the gravitational potential will contribute a few parts in 10^{17} to the overall uncertainty; spacecraft position and velocity will have to be known to 10 cm and 0.12 mm/s, respectively.

Fig. 3 shows stabilities of the critical components of PARCS. The projected

9

clock stability is curve D. The straight curve A shows the frequency-transfer limitation at short integration times, consistent with time transfer at an uncertainty of 220 ps. (The unlabelled curve shows the effect of time transfer at an uncertainty level of 100 ps.) Curve C shows the uncertainty in calculated net frequency shift contributed by position uncertainty alone, from spacecraft tracking at the 1 m level for position and 0.0013 mm/sec level for velocity. The composite uncertainty is given by curve B, where the limit of 5×10^{-16} is due to estimated inaccuracy of the ground clock. The measurement objective for $\Delta f/f$ is achieved in 12 days. Curve D shows the full uncertainty of the space clock being achieved at about 30 days.

2.9   Analyses of GPS Satellite Signals

The ISS is above the troposphere and most of the ionosphere, so the PARCS mission affords the opportunity of viewing GPS satellite signals from a different vantage point. Observations will be limited primarily by the high speed of the ISS and multipath effects associated with signal reflections off ISS structures. Analyses of GPS signals could add to our understanding of the system. When more than four GPS satellites are observed from a receiver with a very stable time base, the navigation equations are highly constrained; this can be turned around to study a particular satellite. Issues of possible interest in GPS include temperature and attitude dependencies of transmitter phase centers.

3   SUMMARY–SCIENCE OBJECTIVES

Table 1 summarizes the scientific objectives for PARCS . These involve the SUMO oscillator that can support a clock stability of $5 \times 10^{-14}\tau^{-1/2}$ and can be used for the on-board, two-clock (LPI) experiments. These results could be enhanced by the concurrent flight of one or more of the clocks being developed elsewhere. If PARCS flies concurrently with SUMO as currently planned, bo the Kennedy-Thorndike (improvement factor 770) and Michelson-Morley experiments (improvement factor 10) can be performed. The objectives and the science requirements for the proposed flight have been dictated primarily by the time-transfer stability considerations shown in Fig. 3.

Appendix

<div align="center">

**Transformation of second-order Doppler shift
of a space-borne atomic clock**
</div>

This Appendix describes an alternative treatment of the second-order Doppler shift contribution to orbiting clock frequency shift. Over long integration times,

<div align="center">

10
</div>

systematic errors in the determination of orbiting clock velocity are a major source of uncertainties in comparing proper time predictions with observation. Such errors can be greatly reduced by transforming this frequency shift contribution into an alternative form appropriate for a satellite in nearly free fall, in which the terms can be evaluated with less uncertainty. This approach has been adopted as the principal method of data analysis for PARCS. Accumulated phase involves integration of the second-order Doppler shift contribution over coordinate time. Velocity is a coordinate time derivative, so this term may be evaluated by integration by parts. The metric of GR, valid to order c^{-2} in the neighborhood of the earth is:[14]

$$ds^2 = g_{\mu\nu}dx^\mu dx^\nu = \left[1 + \alpha_G \frac{2(\Phi - \Phi_0)}{c^2}\right](cdt)^2 - \alpha_D \left[1 + \frac{2\Phi}{c^2}\right](dx^2 + dy^2 + dz^2) \tag{5}$$

where dt is the increment of coordinate time, Φ is the Newtonian gravitational potential, and we have inserted coefficients α_G and α_D (which are exactly equal to unity in GR) to identify the sources of various contributions. Φ_0 is the effective gravitational potential on the earth's rotating geoid. For an orbiting clock in free fall, the equations of motion are

$$\frac{d^2 x^\alpha}{ds^2} + \Gamma^\alpha_{\mu\nu} \frac{dx^\mu}{ds} \frac{dx^\nu}{ds} = \left[\frac{d^2 x^\alpha}{ds^2}\right]_{NG}. \tag{6}$$

where $\Gamma^\alpha_{\mu\nu}$ is the Christoffel symbol of the second kind. The subscript "NG" means the non-gravitational part of the acceleration. If the orbiting satellite is in free fall the right-hand side of the above equation is zero. These equations reduce approximately, in the Newtonian or classical limit, to

$$\alpha_D \frac{d\mathbf{v}}{dt} + \alpha_G \nabla \Phi = \left.\frac{d\mathbf{v}}{dt}\right|_{NG}. \tag{7}$$

This shows that the gravitational part of acceleration is related to the gradient of the potential through the coefficient ratio α_G/α_D.

Let τ_B and τ_B be proper times elapsed on the orbiting clock and the earth-fixed reference clock, respectively, between coordinate times t_1 and t_2. The fractional time difference observable is

$$\frac{\Delta\tau}{\tau} = \frac{\tau_B - \tau_A}{\tau_A} = \frac{\alpha_G}{\tau_A} \int_{t_1}^{t_2} dt \left[\frac{\Phi_B - \Phi_A}{c^2}\right] - \frac{\alpha_D}{\tau_A} \int_{t_1}^{t_2} dt \left[\frac{v_B^2 - v_A^2}{2c^2}\right]. \tag{8}$$

The largest contribution to measurement uncertainty of this observable comes from the second-order Doppler shift term $\int v_B^2 dt$. Transforming this term by

11

integration by parts, using Eq. (7), gives

$$
\begin{aligned}
\frac{\tau_B - \tau_A}{\tau_A} =\ & \frac{\alpha_G}{\tau_A} \int_{t_1}^{t_2} dt \left[\frac{\Phi_B - \frac{1}{2}\mathbf{r}_B \cdot \nabla\Phi_B - \Phi_A}{c^2} \right] + \frac{\alpha_D}{\tau_A} \int_{t_1}^{t_2} dt \left[\frac{v_A^2}{2c^2} \right] \\
& - \frac{\alpha_D}{2c^2 \tau_A} \mathbf{r}_B \cdot \mathbf{v}_B \Big|_{t_1}^{t_2} + \frac{\alpha_D}{2c^2 \tau_A} \int_{t_1}^{t_2} dt \left[\mathbf{r}_B \cdot \mathbf{a}_B \right] \Bigg|_{NG} .
\end{aligned}
\tag{9}
$$

Mathematically, this transformation is exact. The boundary terms involve the dot products of the position and velocity evaluated at times t_1 and t_2. These contributions can be made small. The dot product $\mathbf{r} \cdot \mathbf{v}$ is proportional to the orbital eccentricity and for the planned space station orbit the eccentricity will be in the neighborhood of 0.001. Also, it is possible to select starting and ending points for the experiment for which either the dot product vanishes, such as at apogee, or for which the upper boundary term cancels the lower boundary term. Finally, the boundary term is divided by τ_A and decreases with integration time. For long integration times, this term does not contribute significantly to uncertainties in the prediction of the observable. For integration times as short as one orbital period, if velocity can be measured to better than 1 mm/s and position to better than 1 m, the contribution to the fractional error from one such boundary term is less than 5×10^{-17}.

Second, the non-gravitational acceleration aboard the ISS is projected to be less than about 3×10^{-6} g or 3×10^{-5} m/s^2. The contribution of the uncertainty in this term to the net fractional uncertainty can be reduced to negligible levels by monitoring the non-gravitational acceleration to an accuracy of 400×10^{-9} g. This is well within the expected capabilities of the MAMS (Microgravity Acceleration Measurement System) accelerometers, which is already operating on the ISS. A third contribution is proportional to the time integral of $\mathbf{r}_B \cdot \nabla\Phi_B$. Here it is position errors rather than velocity errors that give rise to uncertainties. This term involves the gravitational coefficient α_G and demonstrates that testing the total accumulated phase shift tests the term proportional to α_G in the metric, which is responsible for the gravitational part of the frequency shift.

Thus errors in predicting the accumulated phase arise from clock instabilities, inaccuracy of the ground clock, time transfer (errors in t_1 and t_2), errors in position and velocity determination of B and A. A similar transformation of the second-order Doppler term $\int dt v_A^2/(2c^2)$ is not necessary. Fig. 3 illustrates application of the integration-by-parts method.

Acknowledgments

12

References

1. Vessot, R.F.C., and M.W. Levine (1979), Gen. Rel. Grav., **10**, pp. 181-204.
2. Bauch, A., and S. Weyers, Phys. Rev. D65, (2002), 081101(R).
3. Jefferts, S.R., D.M. Meekhof, J. Shirley, T.E. Parker, C. Nelson, F. Levi, G. Costanzo, A. De Marchi, R.E. Drullinger, L. Hollberg, W.D. Lee, and F.L. Walls, "Accuracy evaluation of NIST-F1," Metrologia, Dec. 1 (2002).
4. Bauch, A. B. Fischer, T. Heindorff, and R. Schröder (1999), "Recent results of PTB's primary clock CS1," Proc. 1999 Joint Meeting of Eur. Freq. and Time Forum Symp. on Freq. Control, IEEE Cat. No. 99CH36313, pp. 43-46.
5. Ghezali, Ph. Laurent, et. al., (1998), "The accuracy evaluation of the LPTF cesium fountain frequency standard at the 10^{-15} level and future prospects," 12th Eur. Freq. and Time Forum, Warszawa, 10-12 March, 1998, pp. 54.
6. Lemoine, F.G., et. al., "The Development of the Joint NASA GSFC and the National Imagery and Mapping Agency Geopotential Model EGM96," NASA/TP–1998-206861, July 1998, Goddard Space Flight Center, Greenbelt, MD 20771.
7. Mansouri, R., and R.U. Sexl (1977), Gen. Rel. Grav., 8, pp. 515-524.
8. Riis, E., L.A. Andersen, H. Bjerre, O. Poulsen, S.A. Lee, and J.L. Hall (1988), Phys. Rev. Lett., 60, pp. 81-84.
9. Prestage, J.D., R.L. Tjoelker, and L. Maleki (1995), Phys. Rev. Lett., 74, pp. 3511-3514.
10. Hils, D., and J.L. Hall (1990), Phys. Rev. Lett., 64, pp. 1697-1701.
11. Brillet, A., and J.L. Hall (1979), Phys. Rev. Lett., 42, pp. 549-552.
12. Lightman, A., and D. L. Lee (1973), *Phys. Rev.* D**8**, pp. 364-376.
13. Will, C. M., *Theory and experiment in gravitational physics*, (1981), Cambridge University Press, New York , pp. 45-64.
14. Ashby, N., and J.J. Spilker, Jr. (1996) "Introduction to relativistic effects in the global Positioning system," Chap. 18 in *Global Positioning System, Theory and Applications*, vol. I (Institute of Aeronautics and Astronautics, Inc.), pp. 623-698.

13

Improving the Accuracy of Lunar Laser Ranging Tests of Gravitational Theory: Modeling and Future Directions

James G. Williams, Slava Turyshev, and Jean O. Dickey
Jet Propulsion Laboratory, California Institute of Technology, Pasadena, CA 91109

April 16, 2003

Accurate analysis of precision ranges to the Moon have provided several tests of gravitational theory: the equivalence principle, geodetic precession, PPN parameters β and γ, and the constancy of the gravitational constant G. Other possible tests include the inverse square law at 20,000 km length scales and the PPN parameter α_1. The uncertainties of these tests have decreased as data accuracies have improved and data time span has lengthened. We are exploring the modeling improvements necessary to proceed from cm to mm range accuracies. Looking to future exploration, what characteristics are desired for the next generation of ranging devices, what fundamental questions can be investigated, and what are the challenges for modeling and data analysis?

The Multipole Structure of Earth's STEP Signal

Kenneth Nordtvedt
Northwest Analysis
118 Sourdough Ridge Road, Bozeman MT 59715 USA
kennordtvedt@imt.net

March 25, 2004

Abstract

If there is an interaction in physical law which differentially accelerates the test bodies in a STEP satellite, then the different elements that compose the Earth will most likely have source strengths for this interaction which are not proportional to their mass densities. The rotational flattening of Earth and geographical irregularities of our planet's crust then produces a multipole structure for the Equivalence Principle violating force field which differs from the multipole structure of Earth's ordinary gravity field. Measuring these differences yields key information about the new interaction in physical law which is not attainable by solely measuring differences of test body accelerations.

Introduction

The purpose of a Space Test of the Equivalence Principle (STEP) is to measure with extremely high precision any differences between the acceleration of different materials (elements of the periodic table). Any difference will most likely be the result of a previously undetected, long range force field in physical law, which acting between objects leads to an interaction energy between each pair of source elements of the form

$$V(\vec{r}_{ij}) \; = \; - \frac{G\,M_i M_j}{R_{ij}} \; \pm \; \frac{K_i K_j}{R_{ij}} \, exp(-\mu R_{ij})$$

with the new interaction's coupling strengths K_i being different than bodies' mass-energies; and μ being a possible Yukawa inverse range parameter related to the *mass* of the boson field particle responsible for the new interaction. If the new field is *massless* then its spatial dependence is inverse square just as Newtonian gravity. Letting $\kappa_e(\vec{r})$ be the source density in Earth pertinent to this new interaction, then two experimental test bodies would fall toward Earth with rate differences given by

$$\frac{|\vec{a}_i - \vec{a}_j|}{\vec{g}_e} \; = \; \left(\frac{K_1}{M_1} - \frac{K_2}{M_2} \right) \frac{1}{GM_e} \vec{\nabla} \int \frac{\kappa_e(\vec{r'})}{|\vec{r} - \vec{r'}|} \, d^3 r'$$

1

Normally a STEP experiment views its role as just measuring the different K_i/M_i ratios of different materials. This note highlights some interesting further possibilities for the experiment which depend on details of the source integral in this fundamental equation. A generalization of Newton's law of action and reaction usually manifests itself in field theory based interactions, particularly at the static limit. So if objects respond to a force field with coupling strength different than their masses, then objects generally are sources for this force field with strengths different than their masses. So a non-spherically symmetric Earth (in shape and composition) can have novel features in its Equivalence Principle violating (EPV) force field [1].

The Earth's ordinary Newtonian gravitational potential and (EPV) potential can both be expanded in spherical harmonics which reflect the deviations from perfect spherical symmetry of the Earth

$$U(\vec{r}) \quad = \quad G \int \frac{\rho(\vec{r}')}{|\vec{r} - \vec{r}'|} \, d^3r' \;\; = \;\; \frac{GM}{r} \left(1 + \sum_{l=2}^{\infty} \sum_{m=-l}^{m=l} \left(\frac{r_e}{r} \right)^l J_{lm} Y_{lm}(\theta, \phi) \right) \tag{1}$$

$$K(\vec{r}) \quad = \quad \int \frac{\kappa_e(\vec{r}')}{|\vec{r} - \vec{r}'|} \, d^3r' \;\; = \;\; \frac{K}{r} \left(1 + \frac{\vec{d} \cdot \hat{r}}{r} + \sum_{l=2}^{\infty} \sum_{m=-l}^{l} \left(\frac{r_e}{r} \right)^l K_{lm} Y_{lm}(\theta, \phi) \right) \tag{2}$$

Three things should be observed about the expansion for the EPV potential: 1) Since the center of mass-energy has been chosen as origin of the coordinate frame, the mass dipole term vanishes in expansion for $U(\vec{r})$, but generally there will be a dipole term in the potential $K(\vec{r})$; 2) because of the rotational flattening of Earth there will be substantial quadrupole moments J_{20} and K_{20} for the two potentials. Because the Earth's core material and mantel material may havea different ratio of source strength densities for generating the EPV interaction than their mass density ratio, K_{20} will differ from the well-measured J_{20} moment of the Earth; 3) while Earth's mulitipoles other than J_{20} are very small in spite of irregular distributions of high mountains, plains, and deep ocean basins, probably due to the approximate isostacy of the Earth's crust, this isostacy will not so suppress the multipoles in the EPV potential.

Quadrupole Moments

One third the mass of Earth is in its iron-dominated core while the remaining mantle and crustal materials of Earth are composed of relatively low-Z elements. Because the Earth is rotatonally flattened as shown in Figure (1), the matter distributions will produce significant quadrupole moment parameters J_{20} and K_{20}. And because these quadrupole moment integrals for a body weight each differential of matter by the square of distance from the center, the mantle material of Earth contributes more strongly to these moments than their fractional mass fraction. If these two parts of Earth have different ratios in their strengths for producing ordinary gravity and the EPV force field, then the difference between the two quadrupole moment parameters can be estimated to be

$$1 - \frac{K_{20}}{J_{20}} \quad \cong \quad \frac{\kappa_{core}/\rho_{core} - \kappa_m/\rho_m}{\kappa_{core}/\rho_{core} + (M_m/M_{core}) \, \kappa_m/\rho_m} \left(\frac{I_m - f \, (M_m/M_{core}) \, I_{core}}{I_m + f \, I_{core}} \right)$$

$$\cong \quad \frac{\kappa_{core}/\rho_{core} - \kappa_m/\rho_m}{\kappa_{core}/\rho_{core} + 2\kappa_m/\rho_m}$$

with f being the ratio of the core's flattening ratio to that of the mantle. A measurement of K_{20} is seen to involve the sum of κ/ρ ratios as well as the difference. No number of STEP measurements of only differences
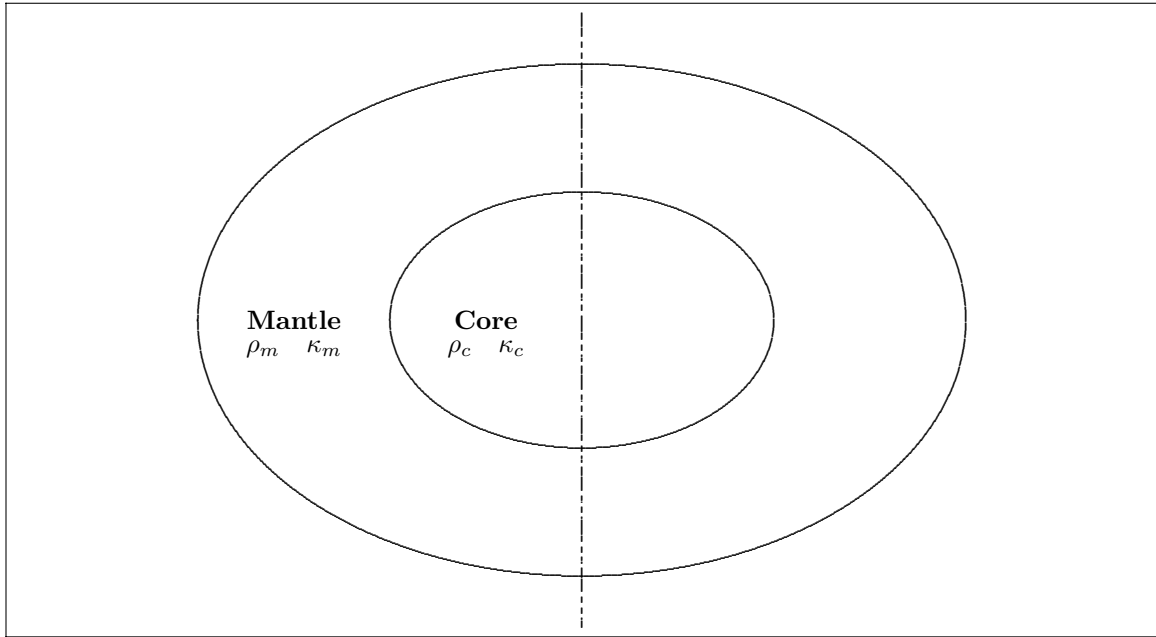
2

Figure 1: The rotationally flattened Earth is shown with its two main material components — core and mantle/crust. When these two components of Earth have different ratios in the source density strengths for ordinary gravity and the EPV force field, $\kappa_m/\rho_m \neq \kappa_c/\rho_c$, the quadrupole parameter K_{20} will differ from gravity's J_{20}.

in the K/M ratios will yield information on the total strength of the new interaction, so this is vital, new information.

EPV Dipole Moment

The Earth's crust is rather irregular in its composition and thickness, being just a few kilometers thick beneath deep ocean basins and tens of kilometers thick beneath high mountains and plateaus — and it is dynamic, albeit on long geologic time scales, as it tends to reach isostatic equilibrium in which the total weight of the crustal material displaces equal weight of heavier mantle material. The crust approximately floats. This explains the small size of the Earth's gravitational mulitpoles; about just the same amount of mantle mass is displaced at any location as there is crustal mass there. But if the crustal material has ratio of strengths κ_{cr}/ρ_{cr} which differs from that of the displaced mantle material, then the dipole moment parameter that appears in the potential expansion, Equation () [2], will be given by

$$\vec{d} \cong \frac{r_e^3}{K} \int \left(\kappa_{cr} - \rho_{cr} \frac{\kappa_m}{\rho_m} \right) h(\theta, \phi) \hat{r} \, d\Omega \cong 3 \frac{\kappa_{cr} - \rho_{cr} \kappa_m / \rho_m}{\kappa_m (1 - \xi) + \xi \kappa_c} \int h(\theta, \phi) \hat{r} \, d\Omega / 4\pi$$

with $h(\theta, \phi)$ being the location-dependent thickness of the crust (plus ocean), $\hat{r}$ being unit vector to surface location, $d\Omega$ being solid angle differential, and ξ being volume fraction of the Earth's core. If only these dipole and quadrupole modifications of the EPV force field are then considered, the field that drives differential accelerations of test bodies on the STEP spacecraft will have the form

$$\vec{a} = -\frac{K}{r^2} \left(\hat{r} - \frac{\vec{d} - 3\vec{d} \cdot \hat{r} \hat{r}}{r} + \frac{3}{2} K_{20} \frac{r_e^2}{r^2} \left((1 - 5 \cos^2 \theta) \hat{r} + 2 \cos \theta \, \hat{z} \right) \right)$$

with the dipole vector $\vec{d}(t)$ being fixed with the rotating Earth and therefore presenting a time-dependence in its equatorial plane components. Measurement of the global EPV parameters, $\vec{d}$ and K_{20} will be facilitated because the signals they produce in differentially accelerating the test bodies in the STEP satellite will generally have different frequencies than the dominant monopolar EPV signal proportional to K.

The Low Altitude STEP Signal Approximation

In order to maximize the strength of the EPV signal originating from Earth's matter, the orbit of a STEP satellite will be as close to Earth as drag considerations permit. So it is appropriate to formulate a low altitude expression for the EPV signal. As illustrated in Figure 2, a satellite is considered which has altitude $\rho << r$ above the Earth's surface. A coordinate system is chosen whose pole, $x = 1 - \cos \theta = 0$, is beneath the instantaneous position of the satellite. Over the entire surface of the Earth there is an inhomogeneous source of the EPV signal proportional to the thickness of the crust, $h(x, \phi)$, and the differences between the crustal materials' EPV source strength and that of the displaced denser mantle material, $\sigma(x, \phi) = \kappa_{cr} - \kappa_m \rho_{cr} / \rho_m$. The vertical and horizontal components of the EPV signal at the satellite can then be expressed as integrals over the Earth's surface.

$$\delta k_v = \int_0^2 \frac{r^2 (\rho + rx)}{(2r (r + \rho) x + \rho^2)^{3/2}} \, dx \int_0^{2\pi} \sigma(x, \phi) \, d\phi$$
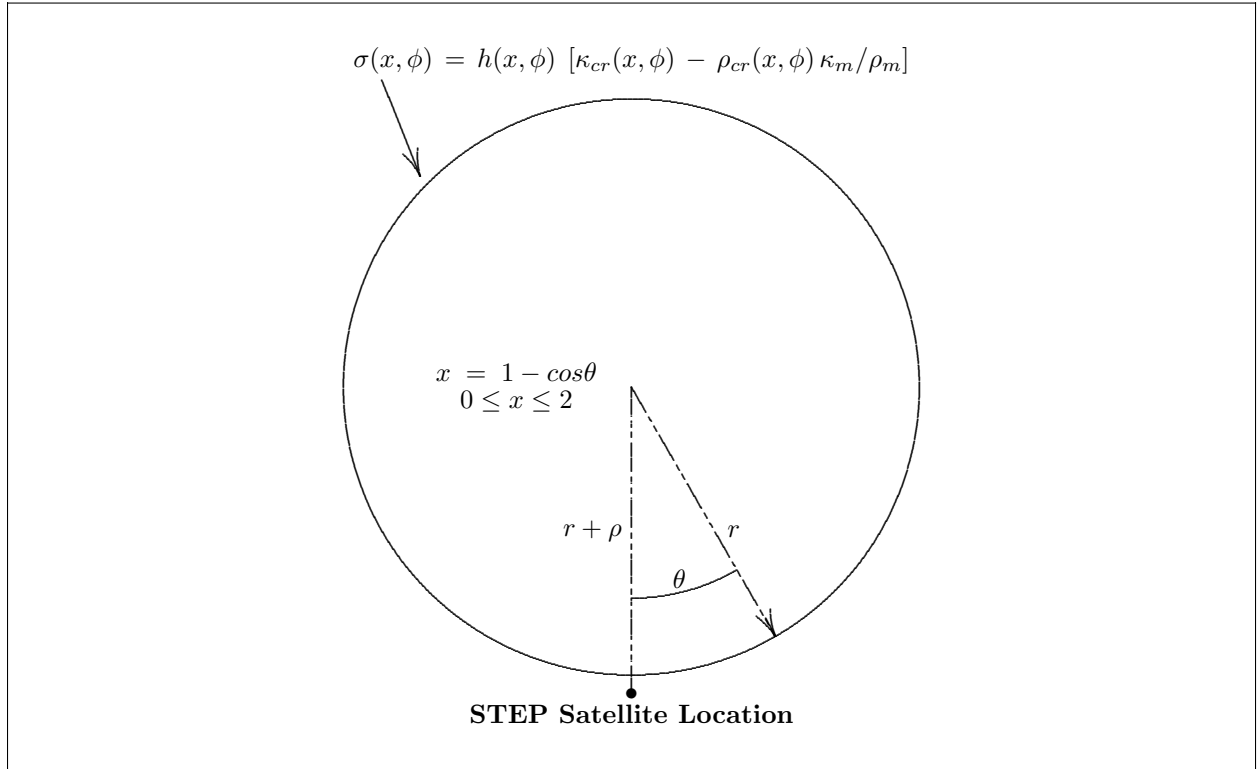
4

Figure 2: For a low altitude STEP satellite, the vertical component of the EPV signal is found to be in part proportional to the source strength of the new EPV interaction directly below the satellite. There is also, in general, a global contribution from the entire surface of the Earth, and there is a horizontal component of the EPV signal which is also determined by aglobal integral.

5

$$\delta \vec{k}_h \ = \ \int_0^2 \frac{r^3 \sqrt{2x - x^2}}{(2r\,(r\,+\,\rho)\,x\,+\,\rho^2)^{3/2}} \ dx \ \int_0^{2\pi} \sigma(x, \phi)\,\hat{u}(\phi)\,d\phi$$

which in the limit of a low altitude satellite take the form

$$\delta k_v \ = \ 2\pi\,\sigma(0) \ + \ \int_0^2 \frac{1}{\sqrt{8x}} \ dx \int_0^{2\pi} \sigma(x, \phi)\,d\phi$$

$$\delta \vec{k}_h \ = \ \int_0^2 \frac{\sqrt{1 - x/2}}{2x} \ dx \int_0^{2\pi} \sigma(x, \phi)\,\hat{u}(\phi)\,d\phi$$

with $\sigma(0)$ is the EPV source strength directly beneath the spacecraft. All components of the EPV signal, however, also receive contributions from global integrals over the entire Earth surface. As the STEP satellite tracks over the entire Earth's surface in the course of its entire mission and many hundreds of orbits, a robust EPV should map out the geographic distribution of the Earth surface's source strength for this new interaction.

References

[1] Nordtvedt K (2000) STEP's equivalence principle violating force field due to non-spherical Earth *Class. Quantum Grav.* **17** 2531-2536

[2] Nordtvedt K (2001) Earth's equivalence principle violating multipoles: more science from a robust violation signal in STEP *Class. Quantum Grav.* **18** 2467-2473

6

General Relativistic Theory of the VLBI Time Delay in the Gravitational Field of Moving Bodies

Sergei Kopeikin
University of Missouri-Columbia

The general relativistic theory of the gravitational VLBI experiment conducted on September 8, 2002 by Fomalont and Kopeikin is explained. Equations of radio waves (light) propagating from the quasar to the observer are integrated in the time-dependent gravitational field of the solar system by making use of either retarded or advanced solutions of the Einstein field equations. This mathematical technique separates explicitly the effects associated with the propagation of gravity from those associated with light in the integral expression for the relativistic VLBI time delay of light. We prove that the relativistic correction to the Shapiro time delay, discovered by Kopeikin (ApJ, 556, L1, 2001), changes sign if one retains direction of the light propagation but replaces the retarded for the advanced solution of the Einstein equations. Hence, this correction is associated with the propagation of gravity. The VLBI observation measured its speed, and that the retarded solution is the correct one.

Experimental investigations of the electromagnetic vacuum:
Can we weigh the vacuum?

April 14, 2003

Lute Maleki

Jet Propulsion Laboratory, California Institute of Technology

ISLES: Probing Extra Dimensions Using a Superconducting Accelerometer

Ho Jung Paik, M. Vol Moody, and Violeta A. Prieto-Gortcheva
Department of Physics, University of Maryland, College Park, MD 20742

In string theories, extra dimensions must be compactified. The possibility that gravity can have large radii of compactification leads to a violation of the inverse square law at submillimeter distances. The objective of ISLES is to perform a null test of Newton's law in space with a resolution of one part in 10^5 or better at 100 μm. The experiment will be cooled to ≤ 2 K, which permits superconducting magnetic levitation of the test masses. To minimize Newtonian errors, ISLES employs a near null source, a circular disk of large diameter-to-thickness ratio. Two test masses, also disk-shaped, are suspended on the two sides of the source mass at a nominal distance of 100 μm. The signal is detected by a superconducting differential accelerometer. A ground test apparatus is under construction.

1. Objective of ISLES

The Newtonian inverse-square ($1/r^2$) law is a cornerstone of General Relativity. Its validity has been demonstrated to one part in 10^8 at $10^7 \sim 10^9$ km and to one part in $10^3 \sim 10^4$ at 1 cm $\sim$ 10 km (Adelberger *et al.*, 1991). The interest in testing Newton's law, at the shortest range possible, has been renewed by a recent suggestion that the $1/r^2$ law may be violated below 1 mm as a manifestation of extra dimensions in spacetime (Arkani-Hamed *et al.*, 1999). The objective of ISLES (Inverse-Square Law Experiment in Space) is to perform a null test of Newton's law in space with a resolution of one part in 10^5 or better at ranges between 100 μm to 1 mm.

Figure 1 shows the existing limits for the $1/r^2$ law at ranges below 1 mm (Hoyle *et al.*, 2001; Long *et al.*, 2003) and the anticipated sensitivities of ISLES on board the ISS, plus expected sensitivities for its free-flyer and ground versions, plotted as functions of the range λ. The expected resolution of ISLES (at 2σ) on the ISS is $|\alpha| = 2 \times 10^{-5}$ at $\lambda = 100$ μm and $|\alpha| = 2 \times 10^{-2}$ at $\lambda = 10$ μm, where the total potential is written as

$$V(r) = -\frac{GM}{r}(1 + \alpha \, e^{-r/\lambda}). \quad (1)$$

This resolution represents an improvement over the existing limit at $\lambda = 100$ μm by six orders of magnitude. The improvement at shorter ranges is even greater. The free-flyer version improves the resolution by another two orders of magnitude. ISLES is also capable of detecting the axion, a candidate dark-matter particle and will probe the extra dimensions down to a few μm.
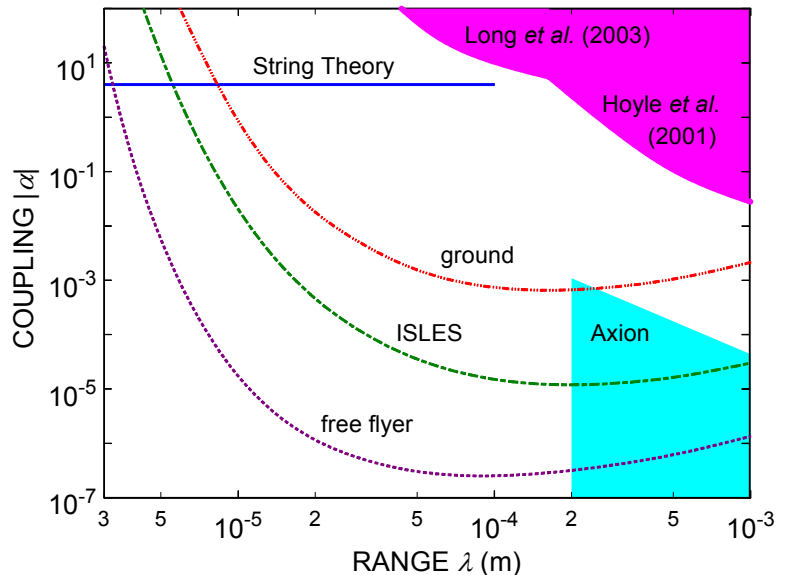

Figure 1. Sensitivity of ISLES versus the existing limit.

2. Scientific Value of Short-Range $1/r^2$ Law Test

Search for extra dimensions. String theories can be consistently formulated only in nine spatial dimensions. Because the space we observe is three-dimensional, the extra dimensions must be hidden. It is possible to have dimensions that affect gravity but not elementary particles, if elementary particles are localized on a three-dimensional subspace ("brane") embedded in a higher-dimensional space.

String theory is defined in terms of a fundamental scale M_*. If there are n compact dimensions with radii $R_1, R_2, \ldots R_n$, Gauss's law implies that the Planck mass M_{Pl} is related to M_* by

$$M_{Pl}^2 \approx M_*^{2+n} R_1 R_2 \ldots R_n \ . \tag{2}$$

As we probe distances shorter than one of the radii R_i, a new dimension opens up and changes the r dependence of the gravitational force law.

Cosmological and astrophysical constraints give a bound $M_* > 100$ TeV (Cullen and Perelstein, 1999; Hall and Smith, 1999), with the most stringent bound, $M_* > 1700$ TeV, coming from the evolution of neutron stars (Hannestad and Raffelt, 2002). For two large extra dimensions of the same magnitude, this most stringent bound corresponds to $R_1 \approx R_2 \leq 40$ nm. While this is beyond the reach of our experiment, there are untested cosmological assumptions going into these bounds. Another interesting scenario is the case of two or more large extra dimensions with $R_1 \gg R_2, \ldots, R_n$. Since Eq. (2) depends only on the product, we can have $M_* \geq 100$ TeV while still having R_1 near the experimental limit.

Thus new developments in string theories raise the possibility that there may be deviations from Newton's law between micron and millimeter length scales. These developments represent the first prediction of a string theory that can be tested, and a discovery of such a deviation from the $1/r^2$ law would be ground breaking. A null result would also be significant in that, in addition to extending the limits of the $1/r^2$ law and General Relativity, it will put constraints on the string scale and on the sizes of any possible extra dimension.

Search for the axion. In strong interactions, non-perturbative effects induce violations of parity (P) and charge conjugation-parity (CP) symmetries, parameterized by a dimensionless angle θ. The *a priori* expectation for the magnitude of θ is of the order of unity, but no such violations of P or CP have been observed in strong interactions. In particular, present upper bounds on the neutron electric dipole moment (Altarev *et al.*, 1992) require $\theta \leq 3 \times 10^{-10}$.

Peccei and Quinn (1977) developed an attractive resolution of this strong CP problem. One ramification of their theory is the existence of a new light-mass boson, the *axion* (Weinberg, 1978; Wilczek, 1978). The axion mediates a short-range mass-mass interaction. The upper bound $\theta \leq 3 \times 10^{-10}$ corresponds to a violation of the $1/r^2$ law at the level of $|\alpha| \approx 10^{-3}$ at $\lambda = 200$ µm, which is well within the reach of our experiment.

The axion could also solve the major open question in astrophysics: the composition of dark matter. Although neutrino mass, MACHOs (MAssive Compact Halo Objects), and many hypothetical particles have been offered as explanations, the solution remains elusive. The axion is one of the strongest candidates for the cold dark matter (Turner, 1990). Confirmation (or rejection) of this prediction would therefore have a major impact in our understanding of the universe, from its most microscopic constituents to its grand scale.

3. Principle of Experiment

Newtonian null source. To maximize the masses that can be brought to within 100 μm from each other, flat disk geometry is used for both the source and test masses. An infinite plane slab is a Newtonian null source. We approximate this null source of Newtonian gravity by using a circular disk of a sufficiently large diameter-to-thickness ratio. Figure 2 shows the configuration of the source and test masses with associated coils and capacitor plates.

Levitated test masses. Two disk-shaped superconducting test masses are suspended on the two sides of the source mass and are coupled magnetically to form a differential accelerometer. The average position of the test masses with respect to the housing are measured with capitors C_1 and C_2, while the motions induced in the levitated test masses are detected by sensing coils (L_{S1} and L_{S2}).

In Earth's gravity (1 g), it is difficult to suspend two flat disks on two sides of the source mass at such proximity without significantly modifying the geometry and stiffening the differential mode, thus degrading the resolution of the experiment. In micro-gravity, each test mass can be suspended by applying only minute forces from a pancake coil (L_{S1} or L_{S2}) and a small ring coil (L_{R1} or L_{R2}) coupled to a narrow slanted rim of the test mass.

Figure 2. Configuration of the source and test masses.

Second harmonic detection. As the source mass is driven at frequency f_S along the symmetry axis, the first-order Newtonian fields arising from the finite diameter of the source mass are canceled upon differential measurement, leaving only a second-order error at $2f_S$. By symmetry, the Yukawa signal of Eq. (1) also appears at $2f_S$. The second harmonic detection, combined with the common-mode rejection ratio (CMRR) of the detector, reduces source-detector vibration coupling by over 300 dB.

Expected signal. The design allows a source displacement of up to ± 50 μm. The differential acceleration signals expected from the Newtonian force errors (with 90% correction) and from the Yukawa forces with $|\alpha| = 10^{-5}$ and $\lambda = 100$ μm are plotted in Figure 3 as a function of the source mass position. The rms amplitude of the Yukawa signal, corresponding to a ± 50-μm displacement, is $8.5 \times 10^{-12}\ \alpha$ m s^{-2}. The rms amplitude of the Newtonian term, arising from the finite diameter of the source mass, is 1.0×10^{-16} m s^{-2} before compensation. The Newtonian error will be computed and removed to $\le 10\%$, which is trivial.
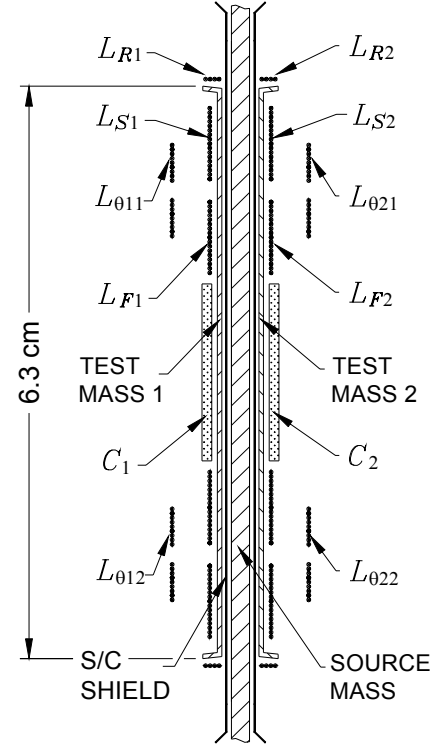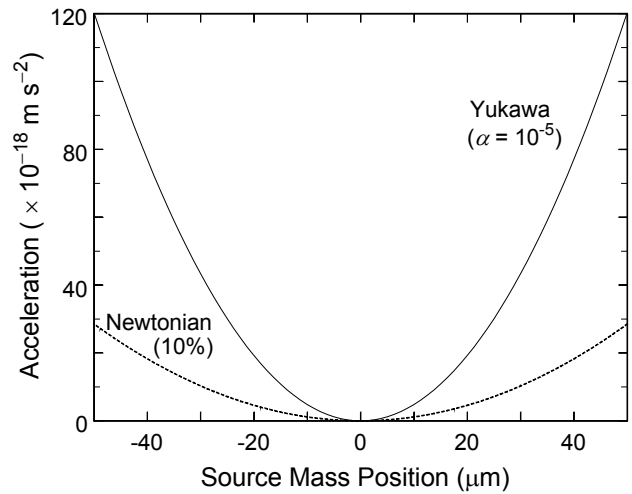

Figure 3. Newtonian (compensated) and Yukawa signals versus source mass position.

4. Experimental Hardware

Overview of the apparatus. Figure 4 shows a cross-sectional view of the apparatus for the ISS experiment. The entire housing is fabricated from niobium (Nb). The source mass is suspended by cantilever springs at the edge and driven magnetically. A thin Nb shield provides electrostatic and magnetic shielding between the source and each test mass. The test masses are suspended and aligned by magnetic fields from various coils. Two auxiliary superconducting accelerometers are mounted on two sides of the housing to provide linear and angular acceleration signals as well as a gravity gradient signal.

The entire assembly weighs 6.0 kg and fits within the 20-cm diameter envelope of the LTMPF instrument well. The apparatus is fastened to the second-stage thermal platform of the Cryo Insert, where the temperature will be stabilized to ≤ 5 μK. The detector orientation is chosen so that its sensitive axis is aligned with the pitch (y) axis of the ISS. This orientation minimizes the centrifugal acceleration noise acting on the test masses.

Figure 4. Cross section of the ISLES apparatus.

Source and test masses. The source mass is a disk 2.0 mm thick by 140 mm in diameter, with mass $M = 510$ g. The source mass, cantilever springs, and rim are machined out of a single plate of Ta. Ta is chosen for its high density (16.6 g cm^{-3}) and its relatively high H_c. Each test mass is a Nb disk 0.25 mm thick by 63 mm in diameter, with a rim 0.25 mm thick by 2.0 mm wide, which has 5° slant from the axis. The mass of each test mass is $m = 7.5$ g.

Superconducting circuitry. Schematics of the superconducting circuits for the detector are shown in Figure 5. These circuits are similar to the standard differencing circuit used at the University of Maryland in the superconducting gravity gradiometer (SGG) (Moody *et al.*, 2002). The test masses are suspended radially by storing persistent currents I_{R1} and I_{R2} in ring coils L_{R1} and L_{R2}, as shown in Figure 5(a). Due to the slanted rim of the test masses, currents I_{R1} and I_{R2} will also exert an axially outward force on the test masses. This outward force is balanced by the axially inward forces provided by the currents in the sensing, alignment, and feedback coils.

The scale factors of the component accelerometers are matched by adjusting currents I_{S1} and I_{S2} in pancake coils L_{S1} and L_{S2}, shown in Figure 5(b). The SQUID measures the differential acceleration a_D, or gravity gradient, along the y-axis. To align an individual test mass parallel to its shield as well as the other test mass, two alignment circuits are provided for each test mass, one per degree of freedom. Figure 5(c) shows the alignment circuit of test mass 1 about the x-axis. To suppress the nonlinearity of the scale factors, a feedback is applied to the test masses, which *actively* stiffens the modes. The common-mode (CM) and differential-mode (DM) outputs i_{FC}
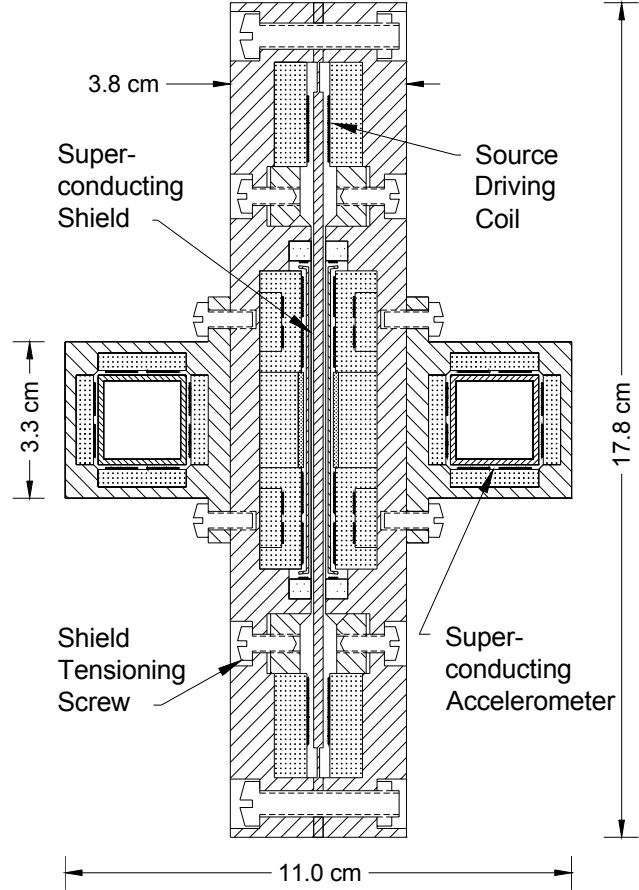
(a) Radial suspension circuit

(b) Sensing circuit

(c) Alignment circuit

(d) Feedback circuit
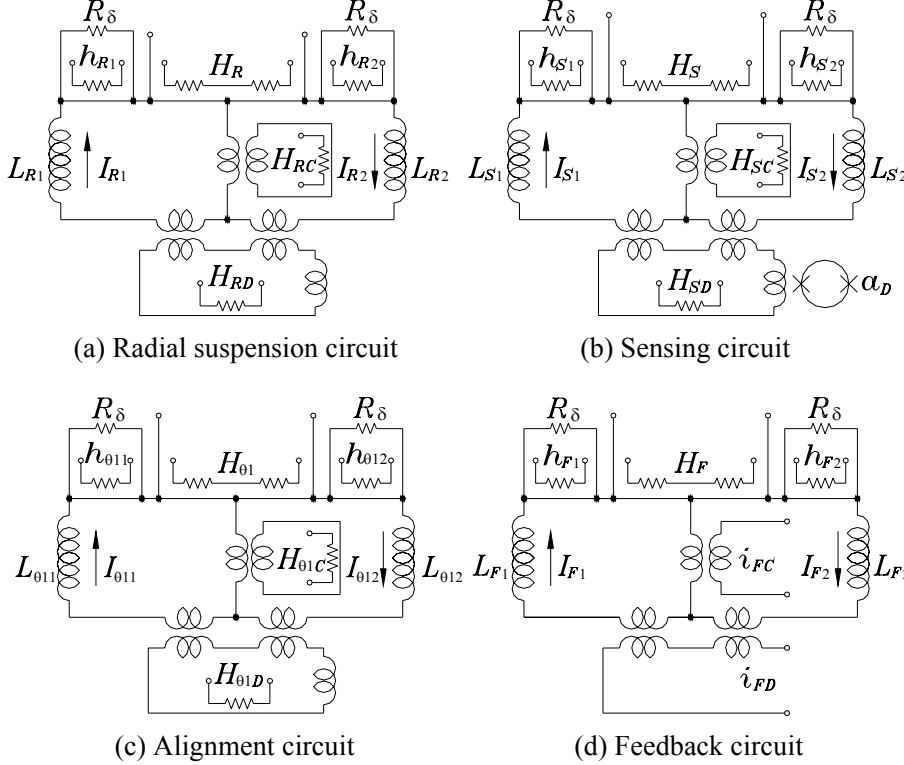
Figure 5. Superconducting circuits for the detector.

and i_{FD} are fed back to the test masses, as shown in Figure 5(d). The CM output is derived from the auxiliary accelerometers.

Coarse and fine heat-switches. To be able to control the magnetic fluxes trapped in various superconducting loops with sufficient precision in the noisy environment of the ISS, two sets of heat-switches are provided: coarse heat-switches, H_{ij}'s, with an L/R time constant of $\sim$ 10 ms, and fine heat-switches, h_{ij}'s, with a time constant of $\sim$ 100 s. With 1-ms time resolution, fluxes can then be adjusted in the aligning, supension, and readout coils to one part in 10^5. This gives the ability to match the scale factors to 10^{-5} and to align the sensitive axes to 10^{-5} rad, resulting in an initial CMRR of 10^5 in all three linear degrees of freedom.

Auxiliary superconducting accelerometers. Figure 4 shows two three-axis auxiliary superconducting accelerometers mounted symmetrically on the two sides of the instrument housing. Each test mass is a hollow 20-g Nb cube, suspended and sensed by Nb pancake coils on its six faces. The accelerometers are coupled to SQUIDs to measure three linear (a_i) and two angular (α_i) acceleration components, plus a gravity gradient component (Γ_{ij}). The unmeasured component α_y is not needed for error compensation.

Error compensation. Linear and angular accelerations are rejected to 10^{-5} and 10^{-4} m, respectively, by adjusting persistent currents in the sensing and alignment circuits. To improve the rejection further, we apply error compensation techniques that have been demonstrated with our SGG (Moody *et al.*, 2002). During the experiment, the linear and angular accelerations of the platform, measured by the auxiliary accelerometers, are multiplied by the predetermined error coefficients (transfer functions) and are subtracted from the detector output. By applying the compensation factor 10^3 to the noise levels, demonstrated in the laboratory, the linear and the angular acceleration rejections are improved to 10^8 and 10^{-7} m, respectively.

Due to the short but finite baseline ($\ell \approx 2.5$ mm), the $1/r^2$ law detector is a gravity gradiometer that is sensitive to attitude modulation of Earth's gravity gradient, to acceleration noise from ISS, and to centrifugal accelerations. The auxiliary gradiometer measures exactly the same gradient noise, except for gravity disturbances from nearby objects (< 1 m). This noise can thus be removed from the detector output by applying the same correlation method.

5. Error Budget

Metrology errors. The effects from the finite diameter of the source and the dynamic mass of the suspension springs are corrected to 10% and 20%, respectively. Linear taper and linear density variation of the source produce second order errors, which become negligible. The test masses tend to rotate slowly about the sensitive axis, averaging out the asymmetry about the axis. Hence only the radial taper and the radial density variation are important. Due to the null nature of the source, test mass metrology is not important, except for the extended rim. The rim dimension is fabricated to 2.5 μm tolerance. The total metrology error is 1.5×10^{-17} m s^{-2}.

Intrinsic instrument noise. The intrinsic power spectral density of a superconducting differential accelerometer is given (Chan and Paik, 1987; Moody *et al.*, 2002) by

$$S_a(f) = \frac{8}{m} \left[\frac{k_B T \omega_D}{Q_D} + \frac{\omega_D^2}{2\eta\beta} E_A(f) \right], \tag{3}$$

where m is the mass of each test mass, $\omega_D = 2\pi f_D$ and Q_D are the differential-mode resonance frequency and quality factor for the test mass motions, β is the electromechanical energy coupling coefficient from the test mass motions to the electrical circuits, η is the electrical energy coupling coefficient of the SQUID, and $E_A(f)$ is the input energy resolution of the SQUID.

Equation (3) shows that f_D is a critical parameter for the intrinsic noise. The microgravity environment on ISS, in principle, allows a suspension 10^6 times softer than on the ground, which corresponds to $f_D < 0.01$ Hz. On the other hand, the test mass displacement in response to the ISS vibration must be minimized to reduce errors due to electric charge, patch-effect fields, self-gravity of the ISS, and most importantly the nonlinearity of the scale factors. Further, the test mass suspension must be stiff enough to keep the test masses from bumping into the housing before the feedback loop is closed. This requirement leads to $f_C \geq 0.2$ Hz. Ideally, one would increase f_C as much as possible, while keeping f_D low. Unfortunately, the nonlinearity of the coils couples a fraction of the CM stiffness to DM, providing a practical limit: $f_C/f_D \leq 4$. Therefore, $f_C \geq 0.2$ Hz implies $f_D \geq 0.05$ Hz.

Substituting $f_D = 0.05$ Hz, $T = 2$ K, $m = 7.5$ g, $Q_D = 10^6$, $\beta = \eta = 0.5$, and typical SQUID noise $E_A(f) = 10^{-30}$ $(1 + 0.1$ Hz$/f)$ J Hz^{-1}, we find the intrinsic noise of the instrument to be $S_a^{1/2}(f) = 7.0 \times 10^{-14}$ m s^{-2} Hz$^{-1/2}$ at $f = 0.02$ Hz.

Acceleration Noise. The y-axis acceleration measured by a SAMS II accelerometer in the US Lab on a typical day corresponds to 3×10^{-6} m s^{-2} Hz$^{-1/2}$ at 0.02 Hz. Assuming that the ISLES detector experiences the same acceleration at its position on the ISS, this noise is reduced to 3×10^{-14} m s^{-2} Hz$^{-1/2}$ by the net CMRR of 10^8. The angular acceleration noise is reduced to 2×10^{-14} m s^{-2} Hz$^{-1/2}$ by the net error coefficient of 10^{-7} m. The centrifugal acceleration noise is negligible. The nonlinearity noise will be reduced to $< 10^{-14}$ m s^{-2} Hz$^{-1/2}$ under a feedback control, which stiffens CM to 10 Hz. The total acceleration noise then becomes 6.3×10^{-14} m s^{-2} Hz$^{-1/2}$ at $f = 0.02$ Hz.

Gravity noise. Helium tide is absent due to the Earth-fixed orientation of the ISS. Helium sloshing is of minor concern since it is expected to occur at a sufficiently low frequency, ~ 2.5 mHz. The gravity noise from modulation of the Earth's gravity gradient and from ISS self-gravity, including the activities of astronauts, along with the centrifugal acceleration, will be taken out by the error compensation scheme described above.

Magnetic crosstalk. Trapped flux is not of concern as long as the flux is strongly pinned. Flux creep will be minimized by cooling and performing the experiment in a low magnetic field. For this purpose, LTMPF is equipped with a Cryoperm magnetic shield.

With the high magnetic field required to drive the source mass, magnetic crosstalk between the source and the detector is a very important potential source of error. To solve this problem, the entire detector housing is machined out of Nb and a thin Nb shield is provided between the source and each test mass. High-purity Nb will be used. The Nb will be heat-treated to bring the material very close to a type-I superconductor, thus minimizing flux penetration. The superconducting shield is expected to provide over 200-dB isolation (Rigby *et al.*, 1990). This shielding, combined with 60-dB rejection from the second harmonic detection, should provide the required isolation between the source drive signal and the test masses in excess of 260 dB.

Electric charge effects. Levitated test masses in orbit will accumulate electric charge from cosmic rays and from high-energy protons as the spacecraft traverses through the South Atlantic Anomaly. Scaling from the charge computed for STEP test masses (Blaser *et al.*, 1996) and correcting for differences in test mass shapes, we find the total charge accumulated in each test mass over the duration of the experiment to be $Q \approx 1.5 \times 10^{-13}$ C.

The charge trapped in the test mass will induce image charges on the neighboring coils and superconducting ground planes. These charges will generate a differential force $Q^2/\varepsilon_0 A$, where ε_0 is the permittivity of vacuum and A is the area of the test mass. The force results in the maximum differential displacement at the end of the mission:

$$x_{D,\text{max}} = \frac{Q^2}{\varepsilon_0 A} \frac{1}{m\omega_D^2} \approx 7 \times 10^{-9}\,\text{m} . \tag{4}$$

This displacement affects the CMRR through mismatches in the accelerometers. With the initial coil gap of 10^{-4} m and a mismatch of 10%, we find that the CMRR is affected by only 7 ppm. This charging-induced error should allow the passive CMRR to remain at the required level of 10^5 throughout the mission. So it appears that ISLES does not require a discharging system. We are planning to carry out a more refined analysis of trapped charge for ISLES.

The energetic charged particles will also impart momentum and cause heating of the test masses. For the STEP study, these effects were found to be less important than the electrostatic force. In addition, the patch-effect potential will be modulated as charge builds up in the test masses, causing a time-varying acceleration. These ac disturbances occur mostly outside the signal band and therefore are averaged out. The Casimir force is not of concern for the present experiment where the gap between the masses is $\geq$ 10 µm (Lamoreaux, 1997).

Temperature noise. The modulation of the penetration depth of a superconductor with temperature and residual thermal expansion coefficients of materials give rise to temperature sensitivity in a superconducting accelerometer. These occur through temperature gradients and mismatches in the accelerometers (Chan and Paik, 1987). From our experience with the SGG, however, this noise is expected to be negligible with the temperature stabilized to 5 µK.

Total errors. Table 1 combines all the errors for the ISS experiment. To reduce the random noise to the levels listed, a 90-day integration period was assumed. Dominant error sources are the intrinsic noise of the differential accelerometer and the platform noise. These errors can be reduced by at least two orders of magnitude by going to a free-flyer.

6. Expected Resolution

By equating the total error with the expected Yukawa signal, we compute the minimum detectable $|\alpha|$. Figure 1 shows the 2σ errors plotted as a function of λ. The best resolution of ISLES on board ISS is $|\alpha| = 2 \times 10^{-5}$ at $\lambda = 100$ μm ~ 1 mm. Extra dimensions will be searched to $R_2 \geq 5$ μm and axions with strength 10 - 100 times below the maximum will be detected.

The resolution of the experiment could be improved by reducing several errors. The metrology and density errors could be reduced by fabricating the source mass out of a crystalline material such as sapphire or quartz, which can be optically polished. The masses would then be coated with a thin layer of Nb. The vibration noise can be improved by several orders of magnitude by going to a free-flyer. Lower vibration levels will allow much softer suspension of the test masses and thus will result in higher instrument sensitivity. The quieter platform will also allow a smaller gap between the masses. With these improvements, a free-flyer ISLES is expected to achieve the resolution depicted by the bottom curve in Figure 1. A free-flyer option of ISLES is under investigation.

Figure 1 also shows the expected sensitivity of our ground experiment. Under 1-g, the test masses will be suspended mechanically by cantilever springs similar to the source mass. The resulting stiffness of the DM modes (≥ 5 Hz) will compromise the resolution of the experiment to $|\alpha| = 10^{-3}$ at $\lambda = 100$ μm. However, this resolution already improves over the existing limit by four orders of magnitude and will be a great stepping stone for a space experiment.

Error Source	Error ($\times 10^{-18}$ m s^{-2})
Metrology	15
Random	(90 days)
Intrinsic	25
ISS vibration	23
Gravity noise	< 1
Vibration coupling	< 1
Magnetic coupling	< 10
Electric charge	< 10
Other (30% margin)	33
Total	52

Table 1. Error budget.

7. Ground Test Apparatus

In order to set a milestone for the $1/r^2$ law test and work out the operational procedures for the orbital experiment, we are constructing a ground test apparatus. Figure 6 is an expanded cross section of the apparatus. A major departure from the space instrument is the mechanical suspension of the test masses.

This ground experiment will provide an opportunity to demonstrate the required scale factor match and axis alignment of the test masses. In addition, the integrity of the superconducting shield and the level of magnetic crosstalk will be investigated. In the process of designing and carrying out error analysis for the ground experiment, we have discovered that the mechanical cross coupling through the source-driven distortion of the housing is a critical error source. To decouple the detector sufficiently from this distortion, we have found it necessary to insert a weak mechanical link between the outer rim, which supports the source mass, and the inner test mass blocks (see Figure 6). This feature will also be incorporated into the design of ISLES instrument.

ISLES will use the SGG technology fully developed at the University of Maryland. The SGG has been used to perform a null test of Newton's law at sensitivity ten times beyond that of the other methods at 1-meter distance (Moody and Paik, 1993). The instrument proposed for ISLES is very similar to the existing SGG. The experimental procedure and error analysis are also similar in many ways to those in the meter-scale $1/r^2$ law test, already carried out with the

SGG. However, the present short-range experiment is much more sensitive to the density inhomogeneity and dimensional errors of the source mass.

The meter-scale experiment employed a Gaussian null detector (Paik, 1979), which made it relatively insensitive to the source errors. In the present experiment, the source itself must produce a uniform field. The test masses are located so close (~ 100 μm) to the surfaces of the source mass that they will be directly sensitive to the imperfections of the source mass. At present, we are exerting a major effort on understanding and controlling the source metrology errors.
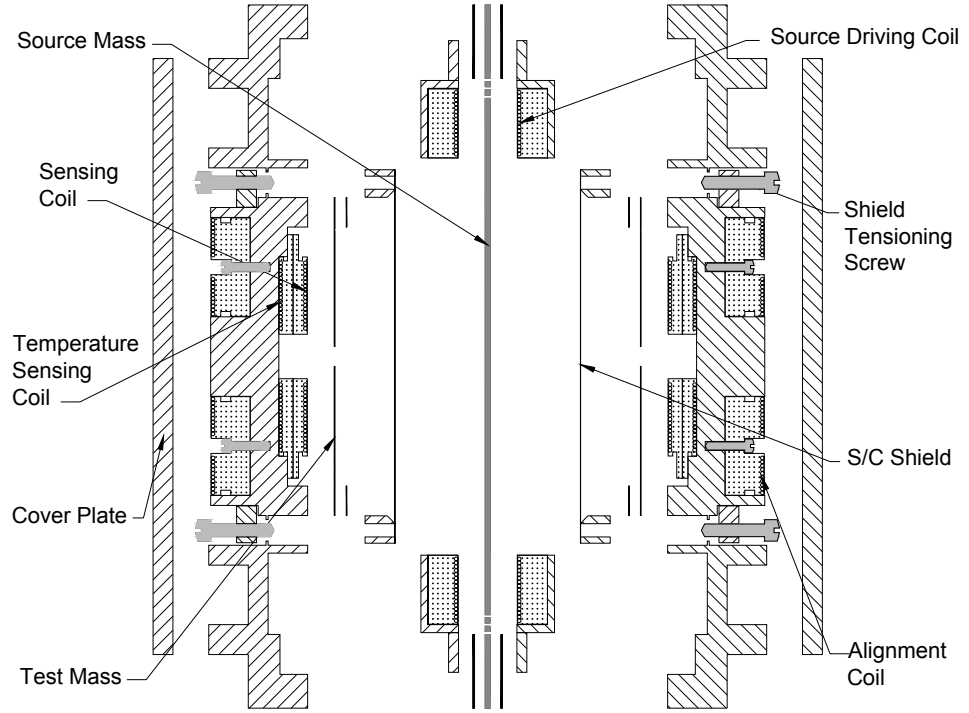
Figure 6. Expanded cross section of the ground experiment.

References

Adelberger, E. G. *et al*. (1991)*, Ann. Rev. Nucl. Part. Sci.* **41**, 269.
Altarev, I. S. *et al*. (1992), *Phys. Lett. B* **276**, 242.
Arkani-Hamed, N., Dimopoulos, S., and Dvali, G. (1999), *Phys. Rev. D* **59**, 086004.
Blaser, J.-P. *et al*. (1996), *STEP*, Report on the Phase A Study, SCI(96)5.
Chan, H. A. and Paik, H. J. (1987), *Phys. Rev. D* **35**, 3551.
Cullen, S. and Perelstein, M. (1999), preprint hep-ph/9903422.
Hall, L. J. and Smith, D. (1999), *Phys. Rev. D* **60**, 085008.
Hannestad, S. and Raffelt, G. G. (2002), *Phys. Rev. Lett*. **88**, 071301.
Hoyle, C. D. *et al*. (2001), *Phys. Rev. Lett*. **86**, 1418.
Lamoreaux, S. K. (1997), *Phys. Rev. Lett*. **78**, 5.
Long, J. C. *et al*. (2003), *Nature* **421**, 922.
Moody, M. V. and Paik, H. J. (1993), *Phys. Rev. Lett*. **70**, 1195.
Moody, M. V., Canavan E. R., and Paik, H. J. (2002), *Rev. Sci. Instrum*. **73,** 3957.
Paik, H. J. (1979), *Phys. Rev. D* **19**, 2320.
Peccei, R. D. and Quinn, H. (1977), *Phys. Rev. Lett*. **38**, 1440.
Rigby, K. W., Marek, D., and Chui, T. C. P. (1990), *Rev. Sci. Inst.* **2**, 834.
Turner, M. S. (1990), *Phys. Rep*. **197**, 67.
Weinberg, S. (1978), *Phys. Rev. Lett*. **40**, 223.
Wilczek, F. (1978), *Phys. Rev. Lett*. **40**, 279.

Microwave Cavity Clocks On Space Station

J. A. Lipa, J. A. Nissen, S. Wang, D. A. Stricker and D. Avaloff
Physics Department, Stanford University, Stanford, CA 94305, USA

We describe the status of a microwave cavity clock experiment to perform improved tests of Local Position Invariance and Lorentz Invariance on the International Space Station in conjunction with atomic clocks. Significant improvements over present bounds are expected in both cases. The oscillators can also be used to enhance the performance of atomic clocks at short time scales for other experiments.

The Laser Astrometric Test of Relativity (LATOR) Mission

Slava G. Turyshev[a], Michael Shao[a] and Kenneth Nordtvedt, Jr.[b]

[a]*Jet Propulsion Laboratory, California Institute of Technology,
Pasadena, CA 91109 U.S.A.*[1]

[b]*Northwest Analysis, 118 Sourdough Ridge Road, Bozeman, MT 59715 U.S.A.*[1]

August 15, 2004

Abstract

This paper discusses new fundamental physics experiment that will test relativistic gravity at the accuracy better than the effects of the second order in the gravitational field strength, $\propto G^2$. The Laser Astrometric Test Of Relativity (LATOR) mission uses laser interferometry between two micro-spacecraft whose lines of sight pass close by the Sun to accurately measure deflection of light in the solar gravity. The key element of the experimental design is a redundant geometry optical truss provided by a long-baseline (100 m) multi-channel stellar optical interferometer placed on the International Space Station (ISS). The spatial interferometer is used for measuring the angles between the two spacecraft and for orbit determination purposes. In Euclidean geometry, determination of a triangle's three sides determines any angle therein; with gravity changing the optical lengths of sides passing close by the Sun and deflecting the light, the Euclidean relationships are overthrown. The geometric redundancy enables LATOR to measure the departure from Euclidean geometry caused by the solar gravity field to a very high accuracy.

LATOR will not only improve the value of the parameterized post-Newtonian (PPN) γ to unprecedented levels of accuracy of 1 part in 10^8, it will also reach ability to measure effects of the next post-Newtonian order (c^{-4}) of light deflection resulting from gravity's intrinsic non-linearity. The solar quadrupole moment parameter, J_2, will be measured with high precision, as well as a variety of other relativistic effects including Lense-Thirring precession. LATOR will lead to very robust advances in the tests of Fundamental physics: this mission could discover a violation or extension of general relativity, or reveal the presence of an additional long range interaction in the physical law. There are no analogs to the LATOR experiment; it is unique and is a natural culmination of solar system gravity experiments.

1 Introduction

Einstein's general theory of relativity (GR) began with its empirical success in 1915 by explaining the anomalous perihelion precession of Mercury's orbit, using no adjustable theoretical parameters. Shortly thereafter, Eddington's 1919 observations of star lines-of-sight during a solar eclipse confirmed the doubling of the deflection angles predicted by GR as compared to Newtonian and Equivalence Principle arguments. From these beginnings, the general theory of relativity has been verified at ever higher accuracy. Thus, microwave ranging to the Viking Lander on Mars yielded accuracy ∼0.1% in the tests of GR [1–3]. The astrometric observations of quasars on the solar background performed with Very-Long Baseline Interferometry (VLBI)

---

improved the accuracy of the tests of gravity to $\sim 0.03\%$ [4–6]. Lunar Laser Ranging (LLR), a continuing legacy of the Apollo program, provided $\sim 0.01\%$ verification of the general relativity via precision measurements of the lunar orbit [7–14]. Finally, the recent experiments with the Cassini spacecraft may improve the accuracy of the tests to $\sim 0.008\%$ [15]. As a result, by now not only the "non-relativistic," Newtonian regime is well understood, but also the first "post-Newtonian" approximation is also well-studied, making general relativity the standard theory of gravity when astrometry and spacecraft navigation are concerned.

However, the continued inability to merge gravity with quantum mechanics and recent observations in cosmology indicate that the pure tensor gravity of general relativity needs modification or augmentation. Recent work in scalar-tensor extensions of gravity which are consistent with present cosmological models [16, 17] motivate new searches for very small deviations of relativistic gravity in the solar system, at levels of 10^{-5} to 10^{-7} of the post-Newtonian effects or essentially to achieve accuracy that enables measurement of the effects of the 2nd order in the gravitational field strength ($\propto G^2$). This will require a several order of magnitude improvement in experimental precision from present tests. At the same time, it is well understood that the ability to measure the second order light deflection term would enable one to demonstrate even higher accuracy in measuring the first order effect, which is of the utmost importance for the gravitational theory and is the challenge for the 21st century Fundamental physics.

When the light deflection in solar gravity is concerned, the magnitude of the first order effect as predicted by GR for the light ray just grazing the limb of the Sun is ~ 1.75 arcsecond. The effect varies inversely with the impact parameter. The second order term is almost six orders of magnitude smaller resulting in ~ 3.5 microarcseconds (μas) light deflection effect, and which falls off inversely as the square of the light ray's impact parameter [18–22]. The relativistic frame-dragging term[2] is ± 0.7 μas, and contribution of the solar quadrupole moment, J_2, is sized as 0.2 μas (using the value of the solar quadrupole moment $J_2 \simeq 10^{-7}$. The small magnitudes of the effects emphasize the fact that, among the four forces of nature, gravitation is the weakest interaction; it acts at very long distances and controls the large-scale structure of the universe, thus, making the precision tests of gravity a very challenging task.

The LATOR mission concept will directly address the challenges discussed above. The test will be performed in the solar gravity field using optical interferometry between two micro-spacecraft. Precise measurements of the angular position of the spacecraft will be made using a fiber coupled multi-chanel led optical interferometer on the International Space Station (ISS) with a 100 m baseline. The primary objective of the LATOR Mission will be to measure the gravitational deflection of light by the solar gravity to accuracy of 0.1 picoradians, which corresponds to $\sim$10 picometers on a 100 m interferometric baseline.

In conjunction with laser ranging among the spacecraft and the ISS, LATOR will allow measurements of the gravitational deflection by a factor of 30,000 better than has previously been accomplished. In particular, this mission will not only measure the key[3] parameterized post-Newtonian (PPN) γ to unprecedented levels of accuracy of one part in 10^8, it will also reach ability to measure the next post-Newtonian order (c^{-4}) of light deflection resulting from gravity's intrinsic non-linearity. As a result, this experiment will measure values of other PPN parameters such as δ to 1 part in 10^3 (never measured before), the solar quadrupole moment

---

[2]Gravitomagnetic frame dragging is the effect in which both the orientation and trajectory of objects in orbit around a body are altered by the gravity of the body's rotation. It was studied by Lense and Thirring in 1918.

[3]The Eddington parameter γ, whose value in general relativity is unity, is perhaps the most fundamental PPN parameter, in that $(1 - \gamma)$ is a measure, for example, of the fractional strength of the scalar gravity interaction in scalar-tensor theories of gravity. Within perturbation theory for such theories, all other PPN parameters to all relativistic orders collapse to their general relativistic values in proportion to $(1 - \gamma)$.

parameter J_2 to 1 part in 20, and the frame dragging effects on light due to the solar angular momentum to precision of 1 parts in 10^2.

The LATOR mission technologically is a very sound concept; all technologies that are needed for its success have been already demonstrated as a part of the JPL's Space Interferometry Mission (SIM) development.[4] The LATOR concept arose from several developments at NASA and JPL that initially enabled optical astrometry and metrology, and also led to developing expertize needed for the precision gravity experiments. Technology that has become available in the last several years such as low cost microspacecraft, medium power highly efficient solid state lasers, and the development of long range interferometric techniques make possible an unprecedented factor of 30,000 improvement in this test of general relativity possible. This mission is unique and is the natural next step in solar system gravity experiments which fully exploits modern technologies.

LATOR will lead to very robust advances in the tests of Fundamental physics: this mission could discover a violation or extension of general relativity, or reveal the presence of an additional long range interaction in the physical law. With this mission testing theory to several orders of magnitude higher precision, finding a violation of general relativity or discovering a new long range interaction could be one of this era's primary steps forward in Fundamental physics. There are no analogs to the LATOR experiment; it is unique and is a natural culmination of solar system gravity experiments.

This paper organized as follows: Section 2 provides more information about the theoretical framework, the PPN formalism, used to describe the gravitational experiments in the solar system. This section also summarizes the science motivation for the precision tests of gravity that recently became available. Section 3 provides the overview for the LATOR experiment including the preliminary mission design. In Section 4 we discuss the next steps that will taken in the development of the LATOR mission.

2   Scientific Motivation

2.1   PPN Parameters and Their Current Limits

Generalizing on a phenomenological parameterization of the gravitational metric tensor field which Eddington originally developed for a special case, a method called the parameterized post-Newtonian (PPN) metric has been developed (see [7, 8, 22–25]. This method represents the gravity tensor's potentials for slowly moving bodies and weak interbody gravity and is valid for a broad class of metric theories including general relativity as a unique case. The several parameters in the PPN metric expansion vary from theory to theory, and they are individually associated with various symmetries and invariance properties of underlying theory. Gravity experiments can be analyzed in terms of the PPN metric, and an ensemble of experiments will determine the unique value for these parameters, and hence the metric field, itself.

In locally Lorentz-invariant theories the expansion of the metric field for a single, slowly-rotating gravitational source in PPN parameters is given by:

$$g_{00} = 1 - 2\frac{M}{r}\left(1 - J_2\frac{R^2}{r^2}\frac{3\cos^2\theta - 1}{2}\right) + 2\beta\frac{M^2}{r^2} + \mathcal{O}(c^{-6}),$$

$$g_{0i} = 2(\gamma + 1)\frac{[\vec{J} \times \vec{r}]_i}{r^3} + \mathcal{O}(c^{-5}),$$

---

[4]Accuracy of 5 picometers was already demonstrated in our SIM-related studies.

$$g_{ij} = -\delta_{ij}\left[1 + 2\gamma\frac{M}{r}\left(1 - J_2\frac{R^2}{r^2}\frac{3\cos^2\theta - 1}{2}\right) + \frac{3}{2}\delta\frac{M^2}{r^2}\right] + \mathcal{O}(c^{-6}), \qquad (1)$$

where M is the mass of the Sun, R is the radius of the Sun, $\vec{J}$ is the angular momentum of the Sun, J_2 is the quadrupole moment of the Sun, and r is the distance between the observer and the center of the Sun. β, γ, δ are the PPN parameters and in GR they are all equal to l. The term M/r in the g_{00} equation is the Newtonian limit; the terms multiplied by the post-Newtonian parameters β, γ, are post-Newtonian terms. The term multiplied by the post-post-Newtonian parameter δ also enters the calculation of the relativistic light deflection.

This PPN expansion serves as a useful framework to test relativistic gravitation in the context of the LATOR mission. In the special case, when only two PPN parameters (γ, β) are considered, these parameters have clear physical meaning. Parameter γ represents the measure of the curvature of the space-time created by a unit rest mass; parameter β is a measure of the non-linearity of the law of superposition of the gravitational fields in the theory of gravity. GR, which corresponds to $\gamma = \beta = 1$, is thus embedded in a two-dimensional space of theories. The Brans-Dicke is the best known theory among the alternative theories of gravity. It contains, besides the metric tensor, a scalar field and an arbitrary coupling constant ω, which yields the two PPN parameter values $\gamma = (1+\omega)/(2+\omega)$, and $\beta = 1$. More general scalar tensor theories yield values of β different from one.

PPN formalism proved to be a versatile method to plan gravitational experiments in the solar system and to analyze the data obtained [7, 8, 22-30]. Different experiments test different combinations of these parameters (for more details, see [24]). The most precise value for the PPN parameter γ is at present given by Eubanks et al [4] as: $|\gamma - 1| = 0.0003$, which was obtained by means of astrometric VLBI. The secular trend of Mercury's perihelion, when describe in the PPN formalism, depends on another linear combination of the PPN parameters γ and β and the quadrupole coefficient $J_{2\odot}$ of the solar gravity field: $\lambda_\odot = (2 + 2\gamma - \beta)/3 + 0.296 \times J_{2\odot} \times 10^4$. The combination of parameters $\lambda_\odot = 0.9996 \pm 0.0006$ was obtained with the Mercury ranging data [31]. The PPN formalism has also provided a useful framework for testing the violation of the Strong Equivalence Principle (SEP) for gravitationally bound bodies. In that formalism, the ratio of passive gravitational mass M_G to inertial mass M_I of the same body is given by $M_G/M_I = 1 - \eta U_G/(M_0 c^2)$, where M_0 is the rest mass of this body and U_G is the gravitational self-energy. The SEP violation is quantified by the parameter η, which is expressed in terms of the basic set of PPN parameters by the relation $\eta = 4\beta - \gamma - 3$. Analysis of planetary ranging data recently yielded an independent determination of parameter γ [14, 32, 33]: $|\gamma - 1| = 0.0015 \pm 0.0021$; it also gave β with accuracy at the level of $|\beta - 1| = -0.0010 \pm 0.0012$. Finally, with LLR finding that Earth and Moon fall toward the Sun at rates equal to 1.5 parts in 10^{13}, even in a conservative scenario where a composition dependence of acceleration rates masks a gravitational self energy dependence η is constrained to be less than 0.0008 [33]; without such accidental cancelation the η constraint improves to 0.0003.

The technology has advanced to the point that one can consider carrying out direct tests in a weak field to second order in the field strength parameter, GM/Rc^2. Although any measured anomalies in first or second order metric gravity potentials will not determine strong field gravity, they would signal that modifications in the strong field domain will exist. The converse is perhaps more interesting: if to high precision no anomalies are found in the lowest order metric potentials, and this is reinforced by finding no anomalies at the next order, then it follows that any anomalies in the strong gravity environment are correspondingly quenched. We shall discuss the recent motivations for the precision gravity tests below in more details.

2.2 Motivations for Precision Gravity Experiments

After almost ninety years since general relativity was born, Einstein's theory has survived every test. Such a longevity, along with the absence of any adjustable parameters, does not mean that this theory is absolutely correct, but it serves to motivate more accurate tests to determine the level of accuracy at which it is violated. A significant number of these tests were conducted over the last 35 years. As an upshot of these efforts, most alternative theories have been put aside; only those theories of gravity flexible enough have survived, the accommodation being provided by the free parameters and the coupling constant of the theory.

Recently considerable interest has been shown in the physical processes occurring in the strong gravitational field regime. It should be noted that general relativity and some other alternative gravitational theories are in good agreement with the experimental data collected from the relativistic celestial mechanical extremes provided by the relativistic motions in the binary millisecond pulsars. However, many modern theoretical models, which include general relativity as a standard gravity theory, are faced with the problem of the unavoidable appearance of space-time singularities. It is generally suspected that the classical description, provided by general relativity, breaks down in a domain where the curvature is large, and, hence, a proper understanding of such regions requires new physics.

The continued inability to merge gravity with quantum mechanics indicates that the pure tensor gravity of general relativity needs modification or augmentation. The tensor-scalar theories of gravity, where the usual general relativity tensor field coexists with one or several long-range scalar fields, are believed to be the most promising extension of the theoretical foundation of modern gravitational theory. The superstring, many-dimensional Kaluza-Klein, and inflationary cosmology theories have revived interest in the so-called "dilaton fields," i.e. neutral scalar fields whose background values determine the strength of the coupling constants in the effective four-dimensional theory. The importance of such theories is that they provide a possible route to the quantization of gravity. Although the scalar fields naturally appear in the theory, their inclusion predicts different relativistic corrections to Newtonian motions in gravitating systems. These deviations from GR lead to a violation of the Equivalence Principle (either weak or strong or both), modification of large-scale gravitational phenomena, and generally lead to space and time variation of physical "constants." As a result, this progress has provided new strong motivation for high precision relativistic gravity tests.

The recent theoretical findings suggest that the present agreement between Einstein's theory and experiment might be naturally compatible with the existence of a scalar contribution to gravity. In particular, Damour and Nordtvedt [16, 17] (see also [34–37] for non-metric versions of this mechanism) have recently found that a scalar-tensor theory of gravity may contain a "built-in" cosmological attractor mechanism towards GR. A possible scenario for cosmological evolution of the scalar field was given in [12, 17]. Their speculation assumes that the parameter $\frac{1}{2}(1 - \gamma)$ was of order of 1 in the early universe, at the time of inflation, and has evolved to be close to, but not exactly equal to, zero at the present time (Figure 1 illustrates this mechanism in more details). The expected deviation from zero may be of the order of the inverse of the redshift of the time of inflation, or somewhere between 1 part per 10^5 and 1 part per 10^7 depending on the total mass density of the universe: $1 - \gamma \sim 7.3 \times 10^{-7}(H_0/\Omega_0^3)^{1/2}$, where Ω_0 is the ratio of the current density to the closure density and H_0 is the Hubble constant in units of 100 km/sec/Mpc. This recent work in scalar-tensor extensions of gravity that are consistent with, indeed often part of, present cosmological models motivates new searches for very small deviations of relativistic gravity in the solar system, at levels of 10^{-5} to 10^{-7} of the post-Newtonian effects.
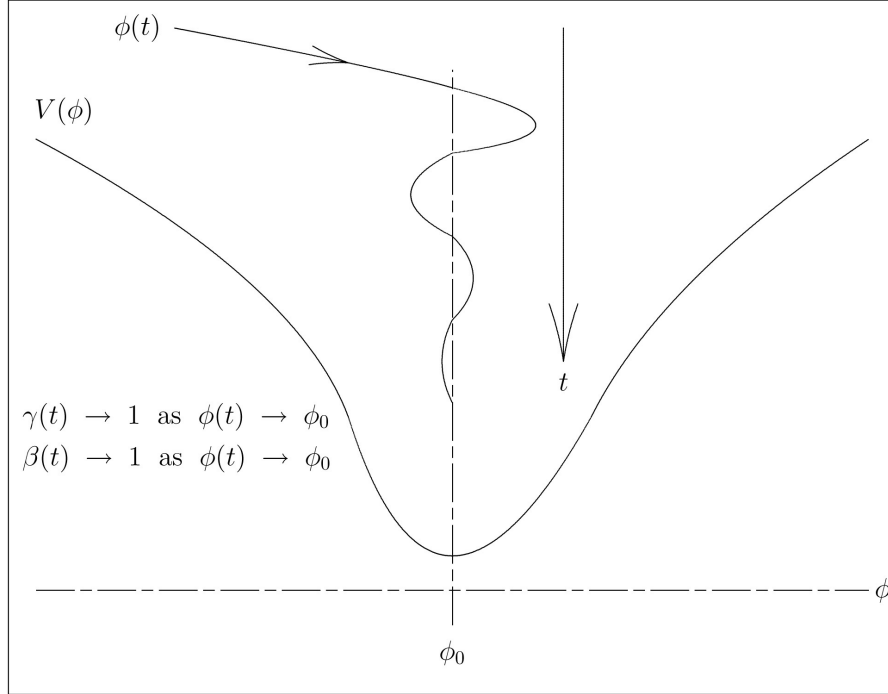
Figure 1: Typical cosmological dynamics of a background scalar field is shown if that field's coupling function to matter, $V(\phi)$, has an attracting point ϕ_0. The strength of the scalar interaction's coupling to matter is proportional to the derivative (slope) of the coupling function, so it weakens as the attracting point is approached, and both the Eddington parameters γ and β (and all higher structure parameters as well) approach their pure tensor gravity values in this limit. But a small residual scalar gravity should remain today because this dynamical process is not complete, and that is what experiment seeks to find.

The theoretical arguments above have been unexpectedly joined by a number of experimental results that motivate more-precise gravitational experiments. Among those are the recent cosmological discoveries and the possible time variation detected in the fine structure constant. In particular, recent astrophysical measurements of the angular structure of the cosmic microwave background [38], the masses of large-scale structures [39], and the luminosity distances of type Ia supernovae [40, 41] have placed stringent constraints on the cosmological constant Λ and also have led to a revolutionary conclusion: the expansion of the universe is accelerating. The implication of these observations for cosmological models is that a classically evolving scalar field currently dominates the energy density of the universe. Such models have been shown to share the advantages of Λ: compatibility with the spatial flatness predicted inflation; a universe older than the standard Einstein-de Sitter model; and, combined with cold dark matter, predictions for large-scale structure formation in good agreement with data from galaxy surveys. Compared to the cosmological constant, these scalar field models are consistent with the supernovae observations for a lower matter density, $\Omega_0 \sim 0.2$, and a higher age, $(H_0 t_0) \approx 1$. If this is indeed the case, the level $\gamma - 1 \sim 10^{-6} - 10^{-7}$ would be the lower bound for the present value of PPN parameter γ [16, 17]. Combined with the fact that scalar field models imprint distinctive signatures on the cosmic microwave background (CMB) anisotropy, they remain currently viable and should be testable in the near future.

This completely unexpected discovery demonstrates the importance of testing the important

ideas about the nature of gravity. We are presently in the "discovery" phase of this new physics, and while there are many theoretical conjectures as to the origin of a non-zero Λ, it is essential that we exploit every available opportunity to elucidate the physics that is at the root of the observed phenomena.

There is also experimental evidence for time-variability in the fine structure constant, α, at the level of $\dot{\alpha}/(\alpha H_0) \sim 10^{-5}$ [42]. This is very similar to time variation in the gravitational constant, which is at the post-Newtonian level expressed as $\dot{G}/(GH_0) \approx \eta = 4\beta - \gamma - 3$, thus providing a tantalizing motivation for further tests of the SEP (Strong Equivalence Principle) parameter η. A similar conclusion resulted from the recent analysis performed in [30, 44, 45]. These new findings necessitate the measurements of γ and β in the range from 10^{-6} to 10^{-8} to test the corresponding gravitational scenario, thus requiring new gravitational physics missions.

Even in the solar system, GR still faces challenges. There is the long-standing problem of the size of the solar quadrupole moment and its possible effect on the relativistic perihelion precession of Mercury (see review in [24]). The interest in lies in the study of the behavior of the solar quadrupole moment versus the radius and the heliographic latitudes. This solar parameter has been very often neglected in the past, because it was rather difficult to determine an accurate value. The improvement of our knowledge of the accuracy of J_2 is certainly due to the fact that, today, we are able to take into account the differential rotation with depth. In fact, the quadrupole moment plays an important role in the accurate computation of several astrophysical quantities, such as the ephemeris of the planets or the general relativistic prediction for the precession of the perihelion of Mercury and other minor planets such as Icarus. Finally, it is necessary to accurately know the value of the quadrupole moment to determinate the shape of the Sun, that is to say its oblateness. Solar oblateness measurements by Dicke and others in the past gave conflicting results for J_2 (reviewed on p. 145 of [46]). A measurement of solar oblateness with the balloon-borne Solar Disk Sextant gave a quadrupole moment on the order of 2×10^{-7} [47]. Helioseismic determinations using solar oscillation data have since implied a small value for J_2, on the order of $\sim 10^{-7}$, that is consistent with simple uniform rotation [24, 48, 49]. However, there exist uncertainties in the helioseismic determination for depths below roughly $0.4\ R_\odot$, which might permit a rapidly rotating core. LATOR can measure J_2 with accuracy sufficient to put this issue to rest.

Finally, there is now multiple evidence indicating that 70% of the critical density of the universe is in the form of a "negative-pressure" dark energy component; there is no understanding as to its origin and nature. The fact that the expansion of the universe is currently undergoing a period of acceleration now seems inescapable: it is directly measured from the light-curves of several hundred type Ia supernovae [40, 41, 50], and independently inferred from observations of CMB by the WMAP satellite [51] and other CMB experiments [52, 53]. Cosmic speed-up can be accommodated within general relativity by invoking a mysterious cosmic fluid with large negative pressure, dubbed dark energy. The simplest possibility for dark energy is a cosmological constant; unfortunately, the smallest estimates for its value are 55 orders of magnitude too large (for reviews see [54, 55]). Most of the theoretical studies operate in the shadow of the cosmological constant problem, the most embarrassing hierarchy problem in physics. This fact has motivated a host of other possibilities, most of which assume $\Lambda = 0$, with the dynamical dark energy being associated with a new scalar field (see [56] and references therein). However, none of these suggestions is compelling and most have serious drawbacks. Given the challenge of this problem, a number of authors considered the possibility that cosmic acceleration is not due to some kind of stuff, but rather arises from new gravitational physics (see discussion in [56–59]). In particular, extensions to general relativity in a low curvature regime were shown to predict an experimentally consistent universe evolution without the need for dark energy.

These dynamical models are expected to produce measurable contribution to the parameter γ in experiments conducted in the solar system also at the level of $1 - \gamma \sim 10^{-7} - 10^{-9}$, thus further motivating the relativistic gravity research. Therefore, the PPN parameter γ may be the only key parameter that holds the answer to most of the questions discussed above.

In summary, there are a number of theoretical reasons to question the validity of GR. Despite the success of modern gauge field theories in describing the electromagnetic, weak, and strong interactions, it is still not understood how gravity should be described at the quantum level. In theories that attempt to include gravity, new long-range forces can arise in addition to the Newtonian inverse-square law. Even at the purely classical level, and assuming the validity of the Equivalence Principle, Einstein's theory does not provide the most general way to generate the space-time metric. Regardless of whether the cosmological constant should be included, there are also important reasons to consider additional fields, especially scalar fields. The LATOR mission is designed to address theses challenges.

2.3 Possible Improvement of PPN Parameters in the Near Future

Prediction of possible deviation of PPN parameters from the general relativistic values provides a robust theoretical paradigm and constructive guidance for experiments that would push beyond the present empirical upper bound on γ of $|\gamma - 1| < 3 \times 10^{-4}$ (obtained by astrometric VLBI [4]). In addition to experiments, which probe parameter γ, any experiment pushing the present upper bounds on β (i.e. $|\beta - 1| < 5 \times 10^{-4}$ from Anderson et al. [14, 33] or LLR constraint on parameter $\eta = 4\beta - \gamma - 3 \leq 3 \times 10^{-4}$ [29, 33, 44, 45]) will also be of great interest. Note that the Eddington parameter γ, whose value in general relativity is unity, is perhaps the most fundamental PPN parameter, in that $(1 - \gamma)$ is a measure, for example, of the fractional strength of the scalar gravity interaction in scalar-tensor theories of gravity. Within perturbation theory for such theories, all other PPN parameters to all relativistic orders collapse to their general relativistic values in proportion to $(1 - \gamma)$. Therefore, measurement of the first order light deflection effect at the level of accuracy comparable with the second-order contribution would provide the crucial information separating alternative scalar-tensor theories of gravity from general relativity [22].

By testing gravity at the level of accuracy needed to see the effects of the second order, one does not simply discriminate among the alternative theories of gravity; in effect, one obtains the critical information on the beginning, current evolution and ultimate future of our universe. The recent remarkable progress in observational cosmology has put general relativity at a test again by suggesting a non-Einsteinian model of universe's evolution. From the theoretical standpoint, the challenge is even stronger - if the gravitational field is to be quantized, the general theory of relativity will have to be modified. This is why the recent advances in the scalar-tensor extensions of gravity, which are consistent with the current inflationary model of the Big Bang, have motivated a new search for a very small deviation of from Einstein's theory, at the level of three to five orders of magnitude below the level tested by experiment.

Tests of fundamental gravitational physics feature prominently among NASA's goals, missions, and programs. Among the future NASA missions that will study the nature of gravity, we discuss here the missions most relevant to LATOR science.

- Gravity Probe-B will be able to improve the test of the geodetic precession; it will also provide the test the relativistic Lense-Thirring precession. The goal is to measure the geodetic precession effect to 2 parts in 10^5 and to measure the frame-dragging effect to 3 parts in 10^3. As a result, this experiment will permit direct measurement of the parameter

γ with accuracy of $\sim 5 \times 10^{-5}$.

- – While the LATOR's accuracy to measure the Lense-Thirring precession will be limited by the small value of the solar angular momentum, the PPN parameter γ will be measured with an accuracy of almost 3.5 orders of magnitude better than that expected with GP-B.

- An improvement in measuring the PPN parameter γ is expected from the Cassini mission. There was a successful solar conjunction experiment in 2002,[5] which allowed studying the gravitational time delay effect. It is expected that this experiment will yield parameter γ to an accuracy of $\sim 5.7 \times 10^{-5}$ [15, 60].

  - – The LATOR mission will perform an experiment essentially very similar to the Cassini conjunction experiments. However, the accuracy of measuring parameter γ will be almost 4 orders of magnitude better. This improvement is due to the optical technologies proposed for LATOR that enable to conduct the light deflection experiment to be conducted almost at the limb of the Sun.

- Data at mm-accuracy is expected from the new LLR ranging station constructed by the APOLLO project [61]. This new technology will result in the measurements of PPN parameter $\eta = 4\beta - 3 - \gamma$ with accuracy of one part in 10^5 [9, 10, 61]. LLR contribution to the relativistic tests of gravity comes from its ability to study the lunar orbit to a high accuracy. As such, LLR is basically a β experiment rather than a γ experiment, primarily testing the non-linearity of gravity theory.[6]

  - – The LATOR mission will benefit from the technologies developed for LLR over the more than 35-years history of this experiment. However, LATOR will be able to directly measure the PPN parameter γ with an accuracy of almost 4 orders of magnitude better than currently available.

- A configuration similar to the geometry of the Cassini conjunction experiments may be utilized for the microwave ranging between the Earth and a lander on Mars. If the lander will be equipped with a Cassini-class X- and Ka-band communication system, the measurement of the PPN parameter γ is possible with an accuracy of $\sim$1 part in 10^6 [62].

  - – As oppose to any scenario involving ranging out to the Mars vicinity, the LATOR mission will not be affected by the difficulty of the asteroid modeling problem. This will allow LATOR to outperform such a mission by at least two orders of magnitude.

- An ambitious test of one of the foundations of general relativity – the Equivalence Principle – is proposed for the STEP (Space Test of Equivalence Principle) mission that is currently being developed by the Stanford GB-P group. The experiment will be able to search for a violation of the Equivalence Principle with a fractional acceleration accuracy of $\Delta a/a \sim 10^{-18}$ [63, 64].

  - – The STEP mission will be able to test very precisely the non-metric breakdowns of metric gravity; however, the results of this mission will say nothing about metric

---

[5]Becasue of the reaction wheel malfunctioning, the 2003 Cassini spacecraft solar conjunction experiment unfortunately did not produce useful data for the tests of relativity [60].

[6]For LLR the PPN parameter γ is usually evaluated by other means, including Sun-induced time delay on interplanetary ranging and ray bending using VLBI [33].

gravity itself. The LATOR mission is designed specifically to test the metric nature of the gravitational interaction. It will be able to test a number of relativistic effects predicted by the metric gravity and will significantly improve the accuracy for several of these tests. In particular, the LATOR's accuracy will be sufficient to measure effects of the second post-Newtonian order of light deflection resulting from gravity's intrinsic non-linearity (further testing the metric structure of the gravitational field); it will provide the value for the solar quadrupole moment parameter, J_2 (currently unknown, limited to $\sim 10^{-7}$), and will measure the relativistic frame-dragging effect.

Concluding, we point out that the recent progress in relativistic gravity research resulted in a significant tightening of the existing bounds on the PPN parameters obtained at the first post-Newtonian level of accuracy. However, this improvement is not sufficient to lead to ground-breaking tests of Fundamental physical laws addressed in Section 2.2. This is especially true, if the cosmological attractor discovered in [4] is more robust, time variation in the fine structure constant will be confirmed in other experiments and various GR extensions will demonstrate feasibility of these methods for cosmology and relativistic gravity. The LATOR mission is proposed to directly address the challenges discussed above. We shall now discuss the LATOR mission in more details.

3   Overview of LATOR

The LATOR experiment uses laser interferometry between two micro-spacecraft (placed in heliocentric orbits, at distances ~ 1 AU from the Sun) whose lines of sight pass close by the Sun to accurately measure deflection of light in the solar gravity.[7] Another component of the experimental design is a long-baseline (~ 100 m) multi-channel stellar optical interferometer placed on the International Space Station (ISS). Figure 2 shows the general concept for the LATOR missions including the mission-related geometry, experiment details and required accuracies.

3.1   Mission Design

The LATOR mission consists of two low cost micro-spacecraft[8] with three interferometric links between the craft and a beacon station on the ISS. One of the longest arms of the triangle ($\sim$ 2 AU) passes near the Sun. The two spacecraft are in the helio-centric orbits and use lasers to measure the distance between them and a beacon station on the ISS. The laser light passes close to the Sun, which causes the light path to be both bent and lengthen. One spacecraft is at the limb of the Sun, the other one is $\sim 1°$ away, as seen from the ISS. Each spacecraft uses laser ranging to measure the distance changes to the other spacecraft. The spatial interferometer is for measuring the angles between the two spacecraft and for the orbit determination purposes.

As evident from Figure 2, the key element of the LATOR experiment is a redundant geometry optical truss to measure the departure from Euclidean geometry caused by Gravity. The triangle in the figure has three independent quantities but the three arms are monitored with laser metrology. From three measurements one can calculate the Euclidean value for any angle in this triangle. In Euclidean geometry these measurements should agree to high accuracy.

---

[7]A version of LATOR with a ground-based receiver was proposed in 1994 (performed under NRA 94-OSS-15) [65]. Due to atmospheric turbulence and seismic vibrations that are not common mode to the receiver optics, a very long baseline interferometer (30 km) was proposed. This interferometer could only measure the differential light deflection to an accuracy of 0.1 μas, with a spacecraft separation of less than 1 arc minutes.

[8]The goal is to launch both spacecraft on a single Delta II launch vehicle.

The LATOR Mission:
Relativistic Deflection of Light

"Reference" spacecraft

$D_{R\text{-}Earth} \sim 2\ AU \quad \approx 0.3 \cdot 10^9\ km$

$\theta \sim 1°$

ISS

Earth

$D_{R\text{-}T} \sim 0.03\ AU \quad \approx 5 \cdot 10^6\ km$

Sun

Apparent position of the "Target" spacecraft

$D_{T\text{-}Earth} \sim 2\ AU \quad \approx 0.3 \cdot 10^9\ km$

Expected accuracies:

$\Delta D_{R,T\text{-}Earth} \approx 15\ cm$

$\Delta D_{R\text{-}T} \approx 1\ cm$

$\Delta \theta \approx 0.1\ picorad$

True position of the "Target" spacecraft

Measured: 3 lengths & 1 angle

Geometric redundancy allows for accurate measurement of the relativistic gravitational deflection of light to 1 part in 10^8.
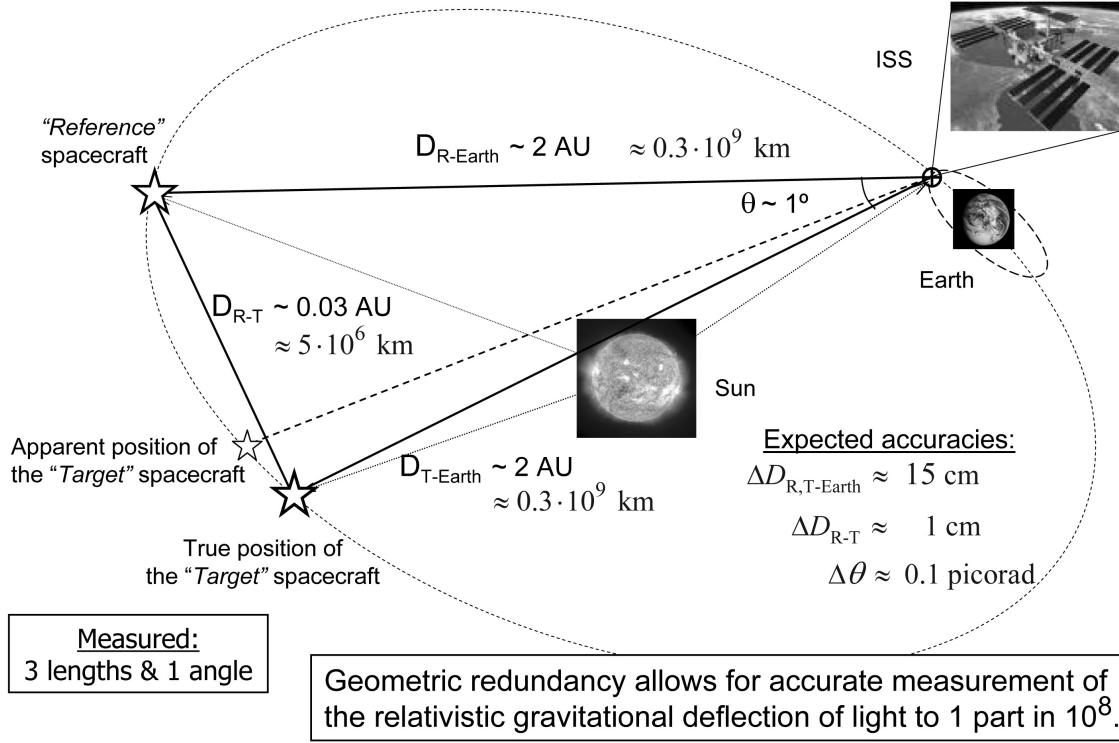
Figure 2: Geometry of the LATOR experiment to measure deviations from the Euclidean geometry in the solar gravitational field.

This geometric redundancy enables LATOR to measure the departure from Euclidean geometry caused by the solar gravity field to a very high accuracy. The difference in the measured angle and its Euclidean value is the non-Euclidean signal. To avoid having to make absolute measurements, the spacecraft are placed in an orbit where their impact parameters, the distance between the beam and the center of the Sun, vary significantly from $10R_\odot$ to $1R_\odot$ over a period of ~ 20 days.

The shortening of the interferometric baseline (as compare to the previously studied version [65]) is achieved solely by going into space to avoid the atmospheric turbulence and Earth's seismic vibrations. On the space station, all vibrations can be made common mode for both ends of the interferometer by coupling them by an external laser truss. This relaxes the constraint on the separation between the spacecraft, allowing it to be as large as a few degrees, as seen from the ISS. Additionally, the orbital motion of the ISS provides variability in the interferometer's baseline projection as needed to resolve the fringe ambiguity of the stable laser light detection by an interferometer.

The first order effect of light deflection in the solar gravity caused by the solar mass monopole is 1.75 arcseconds (see Table 1 for more details), which corresponds to a delay of $\sim$0.85 mm on a 100 m baseline. We currently are able to measure with laser interferometry distances with an accuracy (not just precision but accuracy) of < 1 picometer. In principle, the 0.85

Table 1: Comparable sizes of various light deflection effects in the solar gravity field.

Effect	Analytical Form	Value (μas)	Value (pm)
First Order	$2(1+\gamma)\frac{M}{R}$	1.75×10^6	8.487×10^8
Second Order	$([2(1+\gamma)-\beta+\frac{3}{4}\delta]\pi - 2(1+\gamma)^2)\frac{M^2}{R^2}$	3.5	1702
Frame-Dragging	$\pm 2(1+\gamma)\frac{J}{R^2}$	± 0.7	± 339
Solar Quadrupole	$2(1+\gamma)J_2\frac{M}{R}$	0.2	97

mm gravitational delay can be measured with 10^{-9} accuracy versus 10^{-4} available with current techniques. However, we use a conservative estimate for the delay of 10 pm, which would produce the measurement of γ to accuracy of 1 part in 10^{-8} (i.e., improving the accuracy in determining this parameter by a factor of 30,000) rather than 1 part in 10^{-9}. The second order light deflection is approximately 1700 pm and with 10 pm accuracy it could be measured with accuracy of $\sim 1 \times 10^{-3}$, including first ever measurement of the PPN parameter δ. The frame dragging effect would be measured with $\sim 1 \times 10^{-2}$ accuracy and the solar quadrupole moment (using the theoretical value of the solar quadrupole moment $J_2 \simeq 10^{-7}$) can be modestly measured to 1 part in 20, all with respectable signal to noise ratios.

The laser interferometers use $\sim$2W lasers and $\sim$20 cm optics for transmitting the light between spacecraft. Solid state lasers with single frequency operation are readily available and are relatively inexpensive. For SNR purposes we assume the lasers are ideal monochromatic sources. For simplicity we assume the lengths being measured are 2AU $= 3 \times 10^8$ km. The beam spread is 1 μm/20 cm = 5 μrad (1 arcsecond). The beam at the receiver is $\sim$1,500 km in diameter; a 20 cm receiver will detect 1.71×10^2 photons/sec assuming 50% q.e. detectors. Five picometer (pm) resolution for a measurement of γ to $\sim 10^{-8}$ is possible with approximately 10 seconds of integration.

As a result, the LATOR experiment will be capable of measuring the angle between the two spacecraft to ~ 0.01 μas, which allows light deflection due to gravitational effects to be measured to one part in 10^8. Measurements with this accuracy will lead to a better understanding of gravitational and relativistic physics. In particular, with LATOR, measurements of the first order gravitational deflection will be improved by a factor of 30,000. LATOR will also be capable of distinguishing between first order ($\sim M/R$) and second order ($\sim M^2/R^2$) effects. All effects, including the first and second order deflections, as well as the frame dragging component of gravitational deflection and the quadrupole deflection will be measured astrometrically. We now outline the basic elements of the LATOR trajectory and optical design.

3.2 Trajectory – a 3:2 Earth Resonant Orbit

The objective of the LATOR mission includes placing two spacecraft into a heliocentric orbit with a one year period so that observations may be made when the spacecraft are behind the Sun as viewed from the ISS. The observations involve the measurement of the distance of the two spacecraft using an interferometer on-board the ISS to determine the bending of light by the Sun. The two spacecraft are to be separated by about 1°, as viewed from the ISS.

One trajectory option would be to use a Venus flyby to place the spacecraft in a 1 year orbit (perihelion at Venus orbit ∼0.73 AU and aphelion ∼1.27 AU). One complication of this approach is that the Venus orbit is inclined about 3.4° with respect to the ecliptic and the out-of-plane position of Venus at the time of the flyby determines the orbit inclination [66]. The LATOR observations require that the spacecraft pass directly behind the Sun, i.e., with essentially no orbit inclination. In order to minimize the orbit inclination, the Venus flyby would need to occur near the time of Venus nodal crossing (i.e., around 7/6/2011). An approach with a type IV trajectory and a single Venus flyby requires a powered Venus flyby with about 500 to 900 m/s. However, a type I trajectory to Venus with two Venus gravity assists would get LATOR into a desirable 1 year orbit at Earth's opposition. This option requires no Δv and provides repeated opportunities for the desired science observations. At the same time this orbit has a short launch period ∼17 days which motivated us to look for an alternative.

A good alternative to the double Venus flyby scenario was found when we studied a possibility of launching LATOR into the orbit with a 3:2 resonance[9] with the Earth [66]. For this orbit, in 13 months after the launch, the spacecraft are within ∼ 10° of the Sun with first occultation occuring in 15 months after launch (See Figures 3 and 4). At this point, LATOR is orbiting at a slower speed than the Earth, but as LATOR approaches its perihelion, its motion in the sky begins to reverse and the spacecraft is again occulted by the Sun 18 months after launch. As the spacecraft slows down and moves out toward aphelion, its motion in the sky reverses again and it is occulted by the Sun for the third and final time 21 months after launch. This entire process will again repeat itself in about 3 years after the initial occultation; however, there may be a small maneuver required to allow for more occultations. Therefore, to allow for more occultations in the future, there may be a need for an extra few tens of m/s of Δv.

The C_3 required for launch will vary between ∼10.6 km^2/s^2 – 11.4 km^2/s^2 depending on the time of launch, but it is suitable for a Delta II launch vehicle. The desirable ∼ 1° spacecraft separation (as seen from the Earth) is achieved by performing a 30 m/s maneuver after the launch. This results in the second spacecraft being within ∼ 0.6° – 0.9° separation during the entire period of 3 occultations by the Sun.

Figures 3 and 4 show the trajectory and the occultations in more details. The first figure is the spacecraft position in the solar system showing the Earth's and LATOR's orbits (in the 3:2 resonance) relative to the Sun. The epoch of this figure shows the spacecraft passing behind the Sun as viewed from the Earth. The second figure shows the trajectory when the spacecraft would be within 10 degrees of the Sun as viewed from the Earth. This period of 280 days will occur once every 3 years, provided the proper maneuvers are performed. The two similar periodic curves give the Sun-Earth-Probe angles for the 2 spacecraft; whereas the lower smooth curve gives the angular separation of the spacecraft as seen from the Earth. We intend to further study this trajectory as the baseline option for the LATOR mission.

3.3   Optical Design

A single aperture of the interferometer on the ISS consists of three 10 cm diameter telescopes. One of the telescopes with a very narrow bandwidth laser line filter in front and with an InGAs camera at its focal plane, sensitive to the 1.3 μm laser light, serves as the acquisition telescope to locate the spacecraft near the Sun.

---

[9]The 3:2 resonance occurs when the Earth does 3 revolutions around the Sun while the spacecraft does exactly 2 revolutions of a 1.5 year orbit. The exact period of the orbit may vary slightly (<1%) from a 3:2 resonance depending on the time of launch.
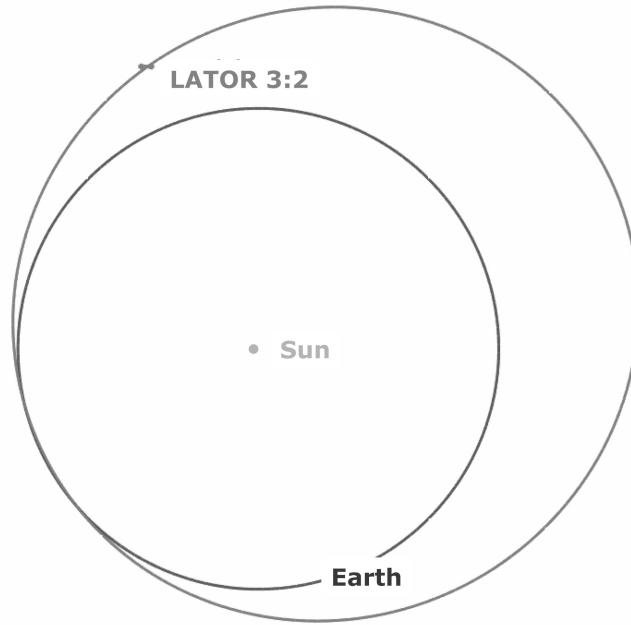
Figure 3: View from the North Ecliptic of the LATOR spacecraft in a 3:2 resonance. The epoch is taken near the first occultation.
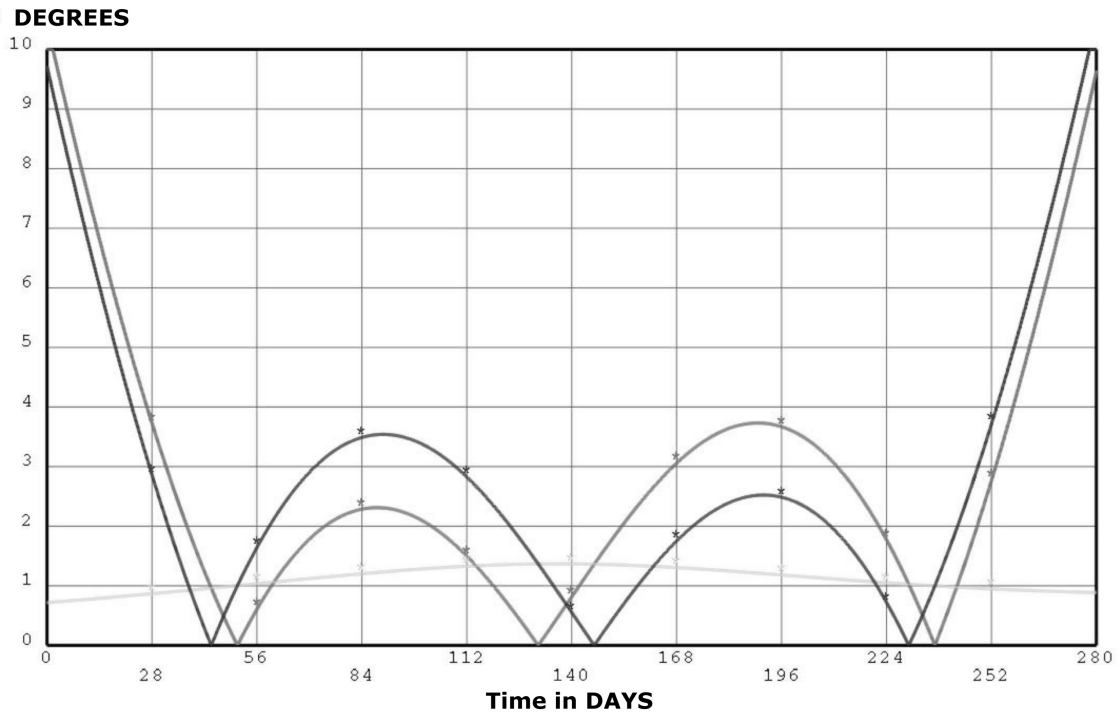

Figure 4: The Sun-Earth-Probe angle during the period of 3 occultations (two periodic curves) and the angular separation of the spacecraft as seen from the Earth (lower smooth line). Time shown is days from the moment when one of the spacecraft is at $10°$ distance from the Sun.

The second telescope emits the directing beacon to the spacecraft. Both spacecraft are served out of one telescope by a pair of piezo controlled mirrors placed on the focal plane. The properly collimated laser light ($\sim$10W) is injected into the telescope focal plane and deflected in the right direction by the piezo-actuated mirrors.

The third telescope is the laser light tracking interferometer input aperture, which can track both spacecraft at the same time. To eliminate beam walk on the critical elements of this telescope, two piezo-electric X-Y-Z stages are used to move two single-mode fiber tips on a spherical surface while maintaining focus and beam position on the fibers and other optics. Dithering at a few Hz is used to make the alignment to the fibers and the subsequent tracking of the two spacecraft completely automatic. The interferometric tracking telescopes are coupled together by a network of single-mode fibers whose relative length changes are measured internally by a heterodyne metrology system to an accuracy of less than 10 picometer.

The spacecraft are identical in construction and contain a relatively high powered (2 W), stable (2 MHz per hour $\sim$ 500 Hz per second), small cavity fiber-amplified laser at 1.3 μm. Three quarters of the power of this laser is pointed to the Earth through a 20 cm aperture telescope and its phase is tracked by the interferometer. With the available power and the beam divergence, there are enough photons to track the slowly drifting phase of the laser light. The remaining part of the laser power is diverted to another telescope, which points toward the other spacecraft. In addition to the two transmitting telescopes, each spacecraft has two receiving telescopes. The receiving telescope on the ISS, which points toward the area near the Sun, has laser line filters and a simple knife-edge coronagraph to suppress the Sun light to 1 part in 10,000 of the light level of the light received from the space station. The receiving telescope that points to the other spacecraft is free of the Sun light filter and the coronagraph.

In addition to the four telescopes they carry, the spacecraft also carry a tiny (2.5 cm) telescope with a CCD camera. This telescope is used to initially point the spacecraft directly toward the Sun so that their signal may be seen at the space station. One more of these small telescopes may also be installed at right angles to the first one to determine the spacecraft attitude using known, bright stars. The receiving telescope looking toward the other spacecraft may be used for this purpose part of the time, reducing hardware complexity. Star trackers with this construction have been demonstrated many years ago and they are readily available. A small RF transponder with an omni-directional antenna is also included in the instrument package to track the spacecraft while they are on their way to assume the orbital position needed for the experiment.

The LATOR experiment has a number of advantages over techniques that use radio waves to measure gravitational light deflection. Advances in optical communications technology allow low bandwidth telecommunications with the LATOR spacecraft without having to deploy high gain radio antennae needed to communicate through the solar corona. The use of the monochromatic light enables the observation of the spacecraft almost at the limb of the Sun, as seen from the ISS. The use of narrow-band filters, coronagraph optics and heterodyne detection will suppress background light to a level where the solar background is no longer the dominant noise source. In addition, the short wavelength allows much more efficient links with smaller apertures, thereby eliminating the need for a deployable antenna. Finally, the use of the ISS will allow conducting the test above the Earth's atmosphere – the major source of astrometric noise for any ground based interferometer. This fact justifies LATOR as a space mission.

4 Conclusions

The LATOR mission aims to carry out a test of the curvature of the solar system's gravity field with an accuracy better than 1 part in 10^8. In spite of the previous space missions exploiting radio waves for tracking the spacecraft, this mission manifests an actual breakthrough in the relativistic gravity experiments as it enables taking full advantage of the optical techniques that recently became available. Our next steps will be to perform studies of trajectory configuration and conduct a mission design including the launch vehicle choice trade studies. Our analysis will concentrate on the thermal design of the instrument, analysis of the launch options and configuration, estimates of on-board power and weight requirements, as well as analysis of optics and vibration contamination for the interferometer. We also plan to develop an end-to-end mission simulation, including a detailed astrometric model and the mission error budget.

The LATOR experiment technologically is a very sound concept; all technologies that are needed for its success have been already demonstrated as a part of the JPL's Space Interferometry Mission development. The concept arose from several developments at NASA and JPL that initially enabled optical astrometry and metrology, and also led to developing expertise needed for the precision gravity experiments. Technology that has become available in the last several years, such as low cost microspacecraft, medium power highly efficient solid state lasers for space applications, and the development of long range interferometric techniques, makes the LATOR mission feasible. The LATOR experiment does not need a drag-free system but uses a geometric redundant optical truss to achieve a very precise determination of the interplanetary distances between the two micro-spacecraft and a beacon station on the ISS. The interest of the approach is to take advantage of the existing space-qualified optical technologies leading to an outstanding performance in a reasonable mission development time. The availability of the space station makes this mission concept realizable in the very near future; the current mission concept calls for a launch as early as in 2009 at a cost of a NASA MIDEX mission.

LATOR will lead to very robust advances in the tests of Fundamental physics: this mission could discover a violation or extension of general relativity or reveal the presence of an additional long range interaction in the physical law. There are no analogs to the LATOR experiment; it is unique and is a natural culmination of solar system gravity experiments.

References

[1] Reasenberg, R. D. et al. "Viking relativity experiment: Verification of signal retardation by solar gravity," Astrophys. J. Lett., 234, L219-L221 (1979).

[2] Shapiro, I. I., Counselman, C. C., III, & King, R. W., "Verification of the Principle of Equivalence for Massive Bodies," Phys. Rev. Lett., 36, 555 (1976).

[3] Shapiro, I. I., et al., "The Viking relativity experiment," JGR, 82, 4329-4334 (1977).

[4] Eubanks T. M., et al., "Advances in Solar System Tests of Gravity." In: Proc. of The Joint APS/AAPT 1997 Meeting, 18-21 April 1997, Washington D.C. BAAS, Abstract #K 11.05, 1997, unpublished.

[5] Robertson, D. S., Carter, W. E., & Dillinger, W. H., Nature, 349, 768 (1991).

[6] Lebach, D. E., Corey, B. E., Shapiro, I. I., Ratner, M. I., Webber, J. C., Rogers, A. E. E., Davis, J. L. & Herring, T. A., Phys. Rev. Lett., 75, 1439 (1995).

[7] Nordtvedt, K., Jr., "Testing Relativity with Laser Ranging to the Moon," Phys. Rev., 170, 1168 (1968).

[8] Nordtvedt, K., Jr., "Lunar Laser Ranging Re-examined: The Non-Null Relativistic Contribution," Phys. Rev. D 43, 10 (1991).

[9] Nordtvedt, K., Jr., "Optimizing the observation schedule for tests of gravity in lunar laser ranging and similar experiments," Class. Quantum Grav. 15, 3363 (1998).

[10] Nordtvedt, K., "30 years of lunar laser ranging and the gravitational interaction," CQG 16, A101 (1999).

[11] Nordvedt, K., Jr. "Gravitomagnetic interaction and laser ranging to Earth satellites," Phys. Rev. Lett. 61, 2647-2649 (1988).

[12] Nordtvedt, K., Jr., "Lunar Laser Ranging - A Comprehensive Probe of Post-Newtonian Gravity," arXiv:gr-qc/0301024.

[13] Williams, J. G., Newhall, X X, & Dickey, J. O., "Relativity Parameters Determined from Lunar Laser Ranging," Phys. Rev. D 53, 6730 (1996).

[14] Williams, J. G., Anderson, J. D., Boggs, D. H., Lau, E. L., & Dickey, J. O., "Solar System Tests for Changing Gravity," AAS Meeting, Pasadena, CA, June 3-7, 2001, BAAS 33, 836 (2001).

[15] Iess L., Giampieri, G., Anderson, J. D., & Bertotti, B., Class. Quant. Gr. 16, 1487 (1999).

[16] Damour, T. & Nordtvedt, K. Jr, "General Relativity as a Cosmological Attractor of Tensor Scalar Theories," Phys. Rev. Lett., 70, 2217-2219 (1993).

[17] Damour, T. & Nordtvedt, K. Jr., "Tensor-scalar cosmological models and their relaxation toward general relativity," Phys. Rev. D48, 3436 (1993).

[18] Epstein, R. & I. I. Shapiro, Phys. Rev. D 22, 2947 (1980).

[19] Fishbach, E. & Freeman, B. S. Phys. Rev. D 22, 2950 (1980).

[20] Richter, G. W. & Matzner, R. A., "2nd-order contributions to relativistic time delay in the parametrized post-Newtonian formalism," Phys. Rev. D 26, 1219 (1982).

[21] Richter, G. W. & Matzner, R. A., Phys. Rev. D 26, 2549 (1982); Phys. Rev. D 28, 3007 (1983).

[22] Nordtvedt, K. Jr., "Probing Gravity to the 2nd Post-Newtonian Order and to one part in 10^7 Using the Sun," ApJ 320, 871-874 (1987).

[23] Nordtvedt, K., Jr., "Equivalence Principle for Massive Bodies. I. Phenomenology," Phys. Rev., 169, 1014 (1968); Nordtvedt, K., Jr., "Equivalence Principle for Massive Bodies. II. Theory," Phys. Rev., 169, 1017 (1968).

[24] Will, C. M., Theory and Experiment in Gravitational Physics, Cambridge, 1993.

[25] Will, C. M. and K. Nordtvedt, Jr., ApJ 177, 757 (1972).

[26] Nordtvedt, K., Jr., Class. Quant. Grav. 13, A11 (1996).

[27] Nordtvedt, K., Jr., "The relativistic orbit observables in lunar laser ranging," Icarus, 114, 51 (1995).

[28] Will, C. M., "General Relativity at 75: How Right was Einstein?" Science 250, 770 (1990); Will, C.M., "The Confrontation between General Relativity and Experiment," (2001) [arXiv:grqc/0103036].

[29] Anderson, J. D., Gross, M., Nordtvedt, K. L. & Turyshev, S. G., ApJ, 459, 365 (1996).

[30] Bender, P. L., Currie, D. C., Dicke, R. H., Eckhardt, D. H., Faller, J. E., Kaula, W. M., Mulholand, J. D., Plotkin, H. H., Poultney, S. K., Silverberg, E. C., Wilkinson, D. T., Williams, J. G. & Alley, C. O., "The Lunar Laser Ranging Experiment," Science, 182, 229 (1973).

[31] Pitjeva, E. V., Celest. Mech. & Dyn. Astr. 55, 313 (1993).

[32] Anderson, J. D., Lau, E. L., Turyshev, S. G., Williams, J. G., Nieto, M. M., "Recent Results for Solar-System Tests of General Relativity," presented at 200-th AAS Meeting, Albuquerque, NM (2-6 June 2002). Paper #12.06. BAAS 34, 833 (2002).

[33] Anderson, J. D. & Williams, J. G., "Long-Range Tests of the Equivalence Principle," Classical and Quantum Gravity, 18, 2447-2456 (2001).

[34] Damour, T., Gibbons, G. W., and Gundlach, G., Phys. Rev. Lett. 64, 123 (1990).

[35] Damour, T. & Taylor, J. H., Phys. Rev. D 45, 1840 (1992).

[36] Damour, T. & Polyakov, A. M., "String Theory and Gravity," Gen. Relativ. Gravit., 26, 1171 (1994).

[37] Damour, T. & Polyakov, A. M., "The string dilaton and a least coupling principle," Nucl. Phys., B 423, 532 (1994).

[38] de Bernardis, P., et al., "A Flat Universe From High-Resolution Maps of the Cosmic Microwave Background Radiation," Nature, 404, 955 (2000).

[39] Peacock, et al., "A measurement of the cosmological mass density from clustering in the 2dF galaxy redshift survey," Nature, 410, 169 (2001).

[40] Perlmutter, S., et al. [Supernova Cosmology Project Collaboration], "Measurements of Omega and Lambda from 42 High-Redshift Supernovae," ApJ 517, 565 (1999).

[41] Riess, A., et al., "Observational Evidence from Supernovae for an Accelerating Universe and a Cosmological Constant," [Supernova Search Team Collaboration], Astron. J. 116, 1009 (1998) [arXiv:astro-ph/9805201].

[42] Murphy, M. T., et al., "Possible evidence for a variable fine structure constant from QSO absorption lines: motivations, analysis and results," Mon. Not. Royal Astron. Soc., 327, 1208 (2001) [arXiv:astro-ph/0012419].

[43] Banks, T., Dine, M., Douglas, M. R., "Time-Varying alpha and Particle Physics," PRL 88, 131301 (2002).

[44] Adelberger, E. G., "New Tests of Einstein's Equivalence Principle and Newton's inverse-square law," Classical and Quantum Gravity, 18, 2397 (2001).

[45] Baessler, S., Heckel, B., Adelberger, E., Gundlach, J., Schmidt, U. & Swanson, H.E., PRL 83, 3585 (1999).

[46] Ciufolini, I. and J. A. Wheeler, Gravitation and Inertia, Princeton, 1995.

[47] Lydon and Sofia, Phys. Rev. Lett. 76, 177 (1996).

[48] Brown et al., Astrophys. J. 343, 526 (1989).

[49] Gough, D. & Toomre, J., "Seismic Observations of the Solar Interior," Ann. Rev. Astron. Aph. 29, 627 (1991).

[50] Tonry, J. L., et al., arXiv:astro-ph/0305008.

[51] Bennett, C. L., et al., [WMAP Science Team] arXiv:astro-ph/0302207.

[52] Halverson, N. W., et al., Astrophys. J. 568, 38 (2002)

[53] Netterfield, C. B., et al. [Boomerang Collaboration], Astrophys. J. 571, 604 (2002).

[54] Carroll, S. M., Living Rev. Rel. 4, 1 (2001).

[55] Peebles, P. J., & Ratra, B., Rev. Mod. Ph. 75, 599 (2003)

[56] Carroll, S. M., Duvvuri, V., Trodden, M., & Turner, M., arXiv:astro-ph/0306438.

[57] Carroll, S. M., Hoffman, M., & Trodden, M., arXiv:astro-ph/0301273.

[58] Dvali, G., & Turner, M. S., arXiv:astro-ph/0301510.

[59] Freese, K. & Lewis, M., Phys. Lett. B 540, 1 (2002).

[60] Anderson, J. D., Lau, E. L., Giampieri, G., arXiv:gr-qc/0308010.

[61] Murphy, T. W., Jr., et al., "The Apache Point Observatory Lunar Laser-Ranging Operation (APOLLO)," Proceedings of 12th International Workshop on Laser, Ranging, Matera, Italy, November 2000, in press, 2002.

[62] Turyshev, S. G., JPL Interoffice Memorandum, #03-3262-027, September, 2003.

[63] Mester, J., Torii, R., Worden, P., Lockerbie, N., Vitale, S., & Everitt, C. W. F., "The STEP Mission: principles and baseline design," CQG 18, 2475 (2001).

[64] Worden, P., Mester, J., & Torii, R., "STEP error model development," CQG 18, 25432550 (2001).

[65] Shao, M. et al., "Laser Astrometric Test of Relativity (LATOR)." JPL Technical Memorandum, October 1996

[66] Gerber, A., et al., "LATOR 2003 Mission Analysis," JPL Advanced Project Design Team (Team X) Report #X-618, July 1, 2003.

Bound on Lorentz and CPT Violating Boost Effects for the Neutron

Ronald Walsworth
Harvard-Smithsonian Center for Astrophysics

A search for a sidereal annual variation in the frequency difference between co-located ^{129}Xe and ^{3}He Zeeman masers sets a limit of approximately 10^{-27} GeV on the coupling of the neutron to the time component of a possible background Lorentz and CPT violating tensor field.

Tests of Lorentz and CPT Invariance in Space *

Matthew Mewes

Physics Department, Indiana University,
Bloomington, IN 47405, U.S.A.

Abstract

I give a brief overview of recent work concerning possible signals of Lorentz violation in sensitive clock-based experiments in space. The systems under consideration include atomic clocks and electromagnetic resonators of the type planned for flight on the International Space Station.

1   Introduction

In this contribution to the proceedings of the 2003 NASA/JPL Workshop on Fundamental Physics in Space, I review recent work aimed at understanding possible tests of Lorentz and CPT symmetries in experiments mounted on space platforms such as the International Space Station (ISS) [1].

A realistic description of nature at the Planck scale remains a major goal of theoretical physics. A direct experimental search for Planck-scale effects does not seem feasible using current technology. However, it has been shown that Planck-scale theories may lead to small violations in fundamental symmetries such as Lorentz and CPT covariance in the low-energy effective theory [2]. Such violations might arise out of the nonlocal properties of string theory. Lorentz and CPT symmetries have also been studied in the context of noncommuting geometries [3] and supersymmetry [4].

Lorentz transformations are in general comprised of rotations and boosts. CPT is the combination of the discrete transformations charge conjugation C, space inversion P and time reversal T. There is a general result known as the CPT theorem which states that a Lorentz-covariant theory is also covariant under the combined transformation CPT [5].

In recent years, a number of sensitive experiments have tested Lorentz and CPT to unprecedented levels [6]. The increased activity in the field has been motivated in part by the development of a general Lorentz- and CPT-violating Standard-Model

1

Extension (SME) [7]. The SME has provided a theoretical framework for many tests of Lorentz and CPT covariance including experiments involving atomic systems [8, 9, 10, 11, 12, 13, 14], photons [15, 16, 17, 18, 19], hadrons [20, 21], muons [22], and electrons [23, 24].

One particularly sensitive class of experiments involves extremely precise clocks and resonators. A number of experiments of this type are under development to test relativity principles on the ISS. These include the atomic-clock based experiments ACES [25], PARCS [26], RACE [27] and a resonant-cavity experiment, SUMO [28]. Some of the best constraints on Lorentz and CPT violation have been achieved in Earth-based atomic-clock experiments [8, 9, 10, 11, 12]. Recently, similar techniques have been used in Earth-based experiments involving superconducting microwave cavities [15] and cryogenically cooled optical cavities [16] that probed previously untested regions of coefficient space. The basic principle behind all these experiments is to search for variations in frequencies of resonant systems as the Earth rotates. The space-based versions will look for variations as the satellite orbits the Earth.

Here, I review recent theoretical studies concerning the effects of Lorentz and CPT violation on atomic clocks [13, 14] and resonant cavities [19] aboard orbiting platforms such as the ISS. A brief discussion of the SME and the QED limit can be found in Section 2. A general discussion of the types of signals one expects from Lorentz violation are described in Section 3. Some results in atomic clocks and in resonant cavities are given Sections 3.1 and 3.2. Some advantages of space-based experiments are described in Section 4.

2   Lorentz-Violating QED

The purpose of the SME is the characterization of all possible types of Lorentz violation in a single local relativistic quantum field theory. Under mild assumptions, one finds that the form of the theory is restricted to the usual Standard-Model lagrangian supplemented by terms that consist of Standard-Model field combinations multiplied by small constant coefficients [7]. Each term must form a scalar under Lorentz transformations of the observer so that coordinate invariance is satisfied. Often one restricts attention to renormalizable terms. However, the nonrenormalizable sector is known to be important at very high energies [29].

The QED limit of the SME serves as a toy-model example of this general framework. It also has physical significance since many systems are accurately represented by this limit. The renormalizable sector of the QED extension is given by the lagrangian

$$
\begin{aligned}
\mathcal{L} \;=\;& \tfrac{1}{2} i \bar{\psi} \Gamma^\nu \overleftrightarrow{D}_\nu \psi - \bar{\psi} M \psi - \tfrac{1}{4} F^{\mu\nu} F_{\mu\nu} \\
& - \tfrac{1}{4} (k_F)_{\kappa\lambda\mu\nu} F^{\kappa\lambda} F^{\mu\nu} + \tfrac{1}{2} (k_{AF})^\kappa \epsilon_{\kappa\lambda\mu\nu} A^\lambda F^{\mu\nu},
\end{aligned}
\tag{1}
$$

2

where D_μ is the usual covariant derivative and

$$\Gamma^\nu = \gamma^\nu + c^{\mu\nu}\gamma_\mu + d^{\mu\nu}\gamma_5\gamma_\mu + e^\nu + if^\nu\gamma_5 + \tfrac{1}{2}g^{\lambda\mu\nu}\sigma_{\lambda\mu}, \tag{2}$$

$$M = m + a_\mu\gamma^\mu + b_\mu\gamma_5\gamma^\mu + \tfrac{1}{2}H_{\mu\nu}\sigma^{\mu\nu}. \tag{3}$$

The small coefficients $c^{\mu\nu}$, $d^{\mu\nu}$, $H_{\mu\nu}$ and $(k_F)_{\kappa\lambda\mu\nu}$ introduce Lorentz violation and are CPT even. Meanwhile, e^ν, f^ν, $g^{\lambda\mu\nu}$, a_μ, b_μ and $(k_{AF})^\kappa$ are Lorentz violating and CPT odd. Note that taking these coefficients to zero yields the usual QED.

The experiments considered in this work search for frequency shifts due to the above coefficients. For atomic clocks, the frequency is typically determined by Zeeman transitions. The presence of Lorentz and CPT violation results in small shifts in these transitions that depend on the coefficients in the modified QED associated with each of the particle species: protons, neutrons and electrons. These coefficients are denoted a_μ^w, b_μ^w, $c_{\mu\nu}^w$, $d_{\mu\nu}^w$, e_ν^w, f_ν^w, $g_{\lambda\mu\nu}^w$, $H_{\mu\nu}^w$, where the $w = p, n, e$ labels the species [12].

In practice, only certain combinations of coefficients appear. These are commonly denoted by tilde coefficients $\tilde{b}_3^w$, $\tilde{c}_q^w$, $\tilde{d}_3^w$, $\tilde{g}_d^w$, $\tilde{g}_q^w$, where I have assumed that the quantization axis is along the 3 direction. As an example of the relationship between the tilde coefficients and those in Eq. (3) consider b_3^e. It is related to the coefficients in the QED for electrons by the expression $\tilde{b}_3^e = b_3^e - m_e d_{30}^e + m_e g_{120}^e - H_{12}^e$. The subscript 3 refers to the quantization axis in the laboratory which in this example was chosen to be in the 3 direction. The subscripts d and q refer to the dipole and quadrupole nature of those terms.

A similar tilde decomposition is useful in the photon sector. The presence of Lorentz violation leads to similar shifts in the resonant frequencies of cavities. When calculating these shifts it is useful to work with the usual electric and magnetic fields. In terms $\vec{E}$ and $\vec{B}$, the $(k_F)_{\kappa\lambda\mu\nu}$ term in the lagrangian (1) may be written

$$-\tfrac{1}{4}(k_F)_{\kappa\lambda\mu\nu}F^{\kappa\lambda}F^{\mu\nu} = \tfrac{1}{2}\tilde{\kappa}_{\mathrm{tr}}(\vec{E}^2 + \vec{B}^2) + \tfrac{1}{2}\vec{E}\cdot(\tilde{\kappa}_{e+} + \tilde{\kappa}_{e-})\cdot\vec{E}$$
$$-\tfrac{1}{2}\vec{B}\cdot(\tilde{\kappa}_{e+} - \tilde{\kappa}_{e-})\cdot\vec{B} + \vec{E}\cdot(\tilde{\kappa}_{o+} + \tilde{\kappa}_{o-})\cdot\vec{B}. \tag{4}$$

The subscripts e, o and tr refer to their O(3) properties. The coefficients $\tilde{\kappa}_{\mathrm{tr}}$, $\tilde{\kappa}_{e+}$ and $\tilde{\kappa}_{e-}$ are parity even while $\tilde{\kappa}_{o+}$ and $\tilde{\kappa}_{o-}$ are parity odd. The single coefficient $\tilde{\kappa}_{\mathrm{tr}}$ is rotationally invariant while the others are 3×3 traceless matrices that violate rotational symmetry.

The above decomposition is motivated by constraints on birefringence of light originating from very distant galaxies. Nonzero coefficients $\tilde{\kappa}_{e+}$ and $\tilde{\kappa}_{o-}$ cause birefringence in light as it traverses empty space resulting in a well defined energy dependence in its polarization. Spectropolarimetric observations of light emitted from distant radio galaxies places a limit on this effect and leads to constraints on the order of $\sim 10^{-32}$ on $\tilde{\kappa}_{e+}$ and $\tilde{\kappa}_{o-}$ [19].

3

3   Signatures of Lorentz Violation

In the event of appreciable Lorentz violation, we would expect experiments to depend on their orientation since rotations are a subgroup of Lorentz transformations. The Lorentz group also contains boosts which implies we would expect velocity dependence as well. A common approach in tests of Lorentz covariance is to search for these types of dependences by looking for variations in some observable as the Earth rotates and orbits the Sun. The rotation of the Earth causes changes in the orientation of the apparatus, while the orbital motion results in changes in velocity. Note that boost effects resulting from the change in velocity are typically suppressed by a factor of $\beta_\oplus \sim 10^{-4}$, the velocity of the Earth around the Sun.

To understand how the orientation and velocity dependence is quantified, we must define at least two frames of reference. The first is the laboratory frame with coordinates $(0, 1, 2, 3)$.[1] The clock or cavity is at rest in this frame which simplifies calculations. In these experiments the Lorentz violation typically leads to frequency shifts that are linear in the tilde coefficients discussed in the previous section. However, these tilde coefficients are not necessarily constant since they are associated with the $(0, 1, 2, 3)$ frame which is not inertial.

To express the frequency shifts in terms of constant coefficients we must choose an inertial frame of reference. The conventional choice is a standard Sun-centered celestial equatorial frame with coordinates (T, X, Y, Z). This frame may be considered inertial for all practical purposes and provides a common set of coefficients which all experiments can refer to. We can relate the coefficients in the $(0, 1, 2, 3)$ frame to those in the (T, X, Y, Z) frame by a Lorentz transformation which is time-dependent since the laboratory frame is in constant motion. For Earth-based experiments this typically introduces a periodic variation at the Earth's rotation rate $\omega_\oplus \simeq 2\pi/(23$ h, 56 min.) and at $2\omega_\oplus$, providing a signal for Lorentz violation. Similar variations at the orbital frequency $\omega_s \simeq 92$ min. and $2\omega_s$ occur in experiments aboard the ISS.

3.1   Atomic Clocks in Space

As an example, here I briefly discuss how atomic-clock experiments on the ISS could be used to search for Lorentz violation. For details I refer the reader to the recent analyses found in Refs. [13, 14].

A typical clock-comparison experiment consists of two co-located clocks using different atomic species or operating on different transitions. Each species and transition responds differently to Lorentz violation. If we compare the signals from the two clocks we may be able to detect a relative shift in their frequencies. For simplicity, one clock could operate on a transition that is known to be insensitive to Lorentz violation [12].

---

[1]A standard set of frames for Earth-based and satellite-based experiments is defined in Ref. [19].

4

Consider a clock at rest in the ISS frame with its quantization axis along the 3 direction. In general, the frequency shift depends on the combinations $\tilde{b}_3^w$, $\tilde{c}_q^w$, $\tilde{d}_3^w$, $\tilde{g}_d^w$, $\tilde{g}_q^w$. The instantaneous values of these coefficients determine the frequency of the clock at any point in the orbit. Expressing these coefficients in terms of Sun-frame coefficients reveals time dependence not present in the absence of Lorentz violation. It is this time dependence that provides a discernible signal for violations in Lorentz and CPT covariance.

The full expressions relating the coefficients in each frame are rather lengthy. However, to first order in small velocities, they take the form [14]:

$$
\begin{aligned}
\tilde{b}_3, \tilde{d}_3, \tilde{g}_d &= \cos \omega_s T_s [\sim] + \sin \omega_s T_s [\sim] \\
&\quad + \beta_s \cos 2\omega_s T_s [\sim] + \beta_s \sin 2\omega_s T_s [\sim] + \beta_s [\sim], \quad (5) \\
\tilde{c}_q, \tilde{g}_q &= \beta_s \cos \omega_s T_s [\sim] + \beta_s \sin \omega_s T_s [\sim] \\
&\quad + \cos 2\omega_s T_s [\sim] + \sin 2\omega_s T_s [\sim] + [\sim], \quad (6)
\end{aligned}
$$

where each $[\sim]$ indicates a different linear combination of the Sun-frame tilde coefficients $\tilde{b}_T$, $\tilde{b}_X$, $\tilde{b}_Y$, $\tilde{b}_Z$, $\tilde{g}_T$, $\cdots$. The quantities $\omega_s \simeq 2\pi/92$ min. and $\beta_s \simeq 10^{-5}$ are the frequency and velocity of the ISS orbit and T_s is the time with an appropriately chosen zero. Note that the $2\omega_s$ variations in the vector and dipole coefficients and the ω_s variations in the quadrupole terms are suppressed by β_s.

3.2 Resonant Cavities in Space

Also slated to fly aboard the ISS is the SUMO experiment [28]. This experiment utilizes superconducting microwave oscillators. The frequencies of resonant cavities are also shifted by Lorentz violation. However, they are sensitive to the photon sector of the QED extension. A detailed analysis of the effects of the $\tilde{\kappa}$ coefficients on the resonant frequencies of cavities can be found in Ref. [19]. The results relevant to SUMO are summarized below.

The cavities used in SUMO are cylindrical with circular cross section and operate in the fundamental TM_{010} mode. Working in a frame where the symmetry axis coincides with 3 axis, a perturbative calculation finds that the frequency shift is linear in the coefficient combinations $(3\tilde{\kappa}_{e+} + \tilde{\kappa}_{e-})^{33}$ and $\tilde{\kappa}_{\mathrm{tr}}$. The frequency shift is easily generalized to a cavity that is at rest in the laboratory but arbitrarily oriented with its symmetry axis denote by a unit vector $\hat{N}$. The result is the fractional-frequency shift

$$
\frac{\delta \nu}{\nu} = -\tfrac{1}{4}\hat{N}^j \hat{N}^k (3\tilde{\kappa}_{e+} + \tilde{\kappa}_{e-})^{jk} - \tilde{\kappa}_{\mathrm{tr}} , \quad (7)
$$

where the indices sum over laboratory-frame coordinates, $j, k = 1, 2, 3$. This expression is valid in any laboratory frame at rest with respect to the cavity.

In order to fully understand the effects of Lorentz violation on a cavity in orbit, we must transform the coefficients to the Sun-centered frame. To first order in the

5

boost velocity, the answer can be written

$$\frac{\delta\nu}{\nu} = -\tfrac{1}{4}\hat{N}^j\hat{N}^k R^{jJ}R^{kK}(\tilde{\kappa}_{e'})^{JK} - \tfrac{1}{2}(\delta^{jk} + \hat{N}^j\hat{N}^k)R^{jJ}R^{kK}\epsilon^{JPQ}\beta^Q(\tilde{\kappa}_{o'})^{KP} - \tilde{\kappa}_{\mathrm{tr}} \ , \quad (8)$$

where for convenience we define

$$(\tilde{\kappa}_{e'})^{JK} = 3(\tilde{\kappa}_{e+})^{JK} + (\tilde{\kappa}_{e-})^{JK} \ , \quad (\tilde{\kappa}_{o'})^{JK} = 3(\tilde{\kappa}_{o-})^{JK} + (\tilde{\kappa}_{o+})^{JK}. \quad (9)$$

The uppercase indices represent the Sun-centered coordinates, $J, K = X, Y, Z$. The matrix R is the rotation between the two frames and β is the velocity of the laboratory in the Sun frame. Inserting the explicit time-dependent expressions R and β leads to periodic variations similar to the atomic-clock case.

A number of different experiments are possible. For example, a cavity could be compared to an atomic clock. The clock could be used as reference by choosing a transition that is insensitive to Lorentz violation. This setup would only be sensitive to violations in the photon sector. In contrast, operating the clock on a transition sensitive to Lorentz violation would provide sensitivity to combinations of photon and fermion coefficients.

It is also possible to construct cavities that are insensitive to given tilde coefficients. For example, geometries exist that support modes that are insensitive to $\tilde{\kappa}_{e-}$. With the constraints from birefringence, this leaves only the β suppressed variations due to $\tilde{\kappa}_{o+}$. Therefore, cavities might serve as reference frequencies for atomic clocks.

Traditionally, two cavities oriented at right angles are used in tests of relativity. This method could also be implemented in space-based experiments. In two-cavity experiments, the quantity of interest is normally the beat frequency obtained by combining their signals. On the ISS, this will take the form

$$\frac{\nu_{beat}}{\nu} \equiv \frac{\delta\nu_1}{\nu} - \frac{\delta\nu_2}{\nu} = \mathcal{A}_s \sin \omega_s T_s + \mathcal{A}_c \cos \omega_s T_s + \mathcal{B}_s \sin 2\omega_s T_s + \mathcal{B}_c \cos 2\omega_s T_s + \mathcal{C}, \quad (10)$$

where the amplitudes $\mathcal{A}_s$, $\mathcal{A}_c$, $\mathcal{B}_s$, and $\mathcal{B}_c$ are linear combinations of the tilde coefficients. These are typically rather cumbersome [19] but depend on the orientation of the cavity pair in the laboratory and on the orientation of the orbital plane with respect to the Sun-centered frame.

It can be shown that orienting a cavity with $\hat{N}$ in the orbital plane maximizes the sensitivity to the second harmonics, at leading order in β and that orienting a cavity so that $\hat{N}$ is 45° out of the plane maximizes sensitivity to the first harmonics. Therefore, a sensible configuration might have one cavity in the orbital plane and one 45° out of it.

4   Advantages of Space-Based Experiments

There are several advantages to space-based experiments over their ground-based counterparts. A major advantage stems from the relatively short orbital period of the

Coefficient	Birefringence	Microwave	Optical
$(\tilde{\kappa}_{e+})^{JK}$	-32	*	*
$(\tilde{\kappa}_{o-})^{JK}$	-32	*	*
$(\tilde{\kappa}_{e-})^{XX} - (\tilde{\kappa}_{e-})^{YY}$	n/a	-13	-15
$(\tilde{\kappa}_{e-})^{ZZ}$	n/a	-	-
$(\tilde{\kappa}_{e-})^{XY}, (\tilde{\kappa}_{e-})^{XZ}, (\tilde{\kappa}_{e-})^{YZ}$	n/a	-13	-15
$(\tilde{\kappa}_{o+})^{XY}, (\tilde{\kappa}_{o+})^{XZ}, (\tilde{\kappa}_{o+})^{YZ}$	n/a	-9	-11
$\tilde{\kappa}_{\text{tr}}$	n/a	-	-

Table 1: Existing bounds for cosmological birefringence [19], microwave cavities [15] and optical cavities [16]. A star indicates that constraints probably exist. However, to date, no analysis has included these coefficients.

ISS. In Earth-based experiments, the relevant period is one sidereal day. Comparing this to the 92 min. period of the ISS orbit implies that an experiment on the ISS could acquire a comparable dataset in approximately one-sixteenth the time.

Another advantage arises from the properties of the ISS orbital plane. For fixed Earth-based experiments, there are combinations of coefficients such as $\tilde{b}_Z$ and $(\tilde{\kappa}_{e-})^{ZZ}$ that do not contribute to sidereal variations and are therefore unobservable.[2] This is due to the constancy of the Earth's rotational axis which is fixed and points in the $\hat{Z}$ direction. The analogous direction in the case of the ISS is given by its orbital axis. However, this axis precesses about the $\hat{Z}$ axis at an angle of approximately $52°$, implying that there is no analogous set of inaccessible coefficients.

One last major advantage is due to β suppressed terms like those that appear in Eqs. (5) and (6). Note that similar $\beta_\oplus$ and β_s suppressed terms appear in the [$\sim$] combinations of Eqs. (5) and (6) and in the amplitudes of Eq. (10). These terms are due to the changing velocity of the ISS in the Sun frame and introduce new time dependences and sensitivities to coefficient combinations that do not appear when considering rotational effects alone. Analogous terms do arise in Earth-based experiments. However, the terms that introduce new time dependences are suppressed by the smaller laboratory velocity $\beta_L \lesssim 1.5 \times 10^{-6} \ll \beta_s$.

5   Summary and Discussion

Table 1 lists the approximate base-10 logarithm of existing constraints on Lorentz violation in the photon sector. Ground-based experiments involving microwave [15] and optical [16] cavities have measured all components of $\tilde{\kappa}_{e-}$ and $\tilde{\kappa}_{o+}$ except $(\tilde{\kappa}_{e-})^{ZZ}$. A space-based experiment could immediately access the unconstrained coefficient $(\tilde{\kappa}_{e-})^{ZZ}$. Improved sensitivities are also expected. It has been estimated that SUMO

---

[2]Coefficients of this type can be accessed with the use of a turntable as in Ref. [24].

7

Coefficient	Proton	Neutron	Electron
$\tilde{b}_X,\ \tilde{b}_Y$	-27[-27]	[-31]	-27[-29]
$\tilde{b}_Z$	-27	-	-27[-28]
$\tilde{b}_T$	-23	-	-23
$\tilde{g}_T$	-23	-	-23
$\tilde{H}_{JT}$	-23	-	-23
$\tilde{d}_\pm$	-23	-	-23
$\tilde{d}_Q$	-23	-	-23
$\tilde{d}_{JK}$	-23	-	-23
$\tilde{d}_X,\ \tilde{d}_Y$	-25[-25]	[-29]	-22[-22]
$\tilde{d}_Z$	-25	-	-22
$\tilde{g}_{DX}, \tilde{g}_{DY}$	-25[-25]	[-29]	-22[-22]
$\tilde{g}_{DZ}$	-25	-	-22
$\tilde{g}_{JK}$	-21	-	-18
$\tilde{g}_c$	-23	-	-23
$\tilde{c}_{TJ}$	-20	-	-
$\tilde{c}_-$	-25	[-27]	-
$\tilde{c}_Q$	-25	-	-
$\tilde{c}_X,\ \tilde{c}_Y$	-25	[-25]	-
$\tilde{c}_Z$	-25	[-27]	-
$\tilde{c}_{TJ}$	-21	-	-
$\tilde{g}_-$	$\star[\star]$	$[\star]$	-
$\tilde{g}_Q$	$\star$	-	-
$\tilde{g}_{TX},\ \tilde{g}_{TY}$	$\star[\star]$	$[\star]$	-
$\tilde{g}_{TZ}$	$\star[\star]$	$[\star]$	-

Table 2: Estimated sensitivity to tilde coefficients for ISS experiments with ^{133}Cs and ^{87}Rb clocks taken from Ref. [14]. Existing bounds [8, 9, 10, 11, 24] are shown in brackets. A star indicates possible sensitivity in realistic nuclear model.

8

may be able to achieve sensitivity at the level of 10^{-17} [15].

The above discussion could can also be applied to optical-cavity experiments. Currently, the most precise measurements of $\tilde{\kappa}_{e-}$ and $\tilde{\kappa}_{o+}$ are from an optical-cavity experiment [16] and space-based versions such as those proposed for the OPTIS experiment [30] could also yield interesting results.

Note that the rotationally invariant component $\tilde{\kappa}_{\text{tr}}$ is also unconstrained. This is because, at order β, it results in unobservable constant shifts. However, it becomes important at order β^2 and could be accessed at interesting levels in experiments involving larger boosts or better sensitivity.

Table 2 lists the estimates given in Ref. [14] for the sensitivities of ^{133}Cs and ^{87}Rb clocks on the ISS. The brackets indicate measurements from current ground-based experiments. The table illustrates the main advantage of space-based clock-comparison experiments. The additional freedom in the motion of the ISS results in access to a much larger portion of the coefficient space.

Future clock-comparison experiments in space will probe regions of coefficient space difficult to access on Earth. They will do it more quickly and perhaps with better sensitivity than their ground-based counterparts.

References

[1] See, for example, *The International Space Station Users' Guide,* Release 2.0, NASA, 2000.

[2] V.A. Kostelecký and R. Potting, Nucl. Phys. B **359**, 545 (1991); Phys. Lett. B **381**, 89 (1996); Phys. Rev. D **63**, 046007 (2001); V.A. Kostelecký and S. Samuel, Phys. Rev. D **39**, 683 (1989); Phys. Rev. Lett. **63**, 224 (1989); Phys. Rev. D **40**, 1886 (1989). V.A. Kostelecký, M. Perry, and R. Potting, Phys. Rev. Lett. **84**, 4541 (2000).

[3] S.M. Carroll *et al.*, Phys. Rev. Lett. **87**, 141601 (2001); Z. Guralnik, R. Jackiw, S.Y. Pi, and A.P. Polychronakos, Phys. Lett. B **517**, 450 (2001); C.E. Carlson, C.D. Carone, and R.F. Lebed, Phys. Lett. B **518**, 201 (2001); A. Anisimov, T. Banks, M. Dine, and M. Graesser, Phys. Rev. D **65**, 085032 (2002); I. Mocioiu, M. Pospelov, and R. Roiban, Phys. Rev. D **65**, 107702 (2002); M. Chaichian, M.M. Sheikh-Jabbari, and A. Tureanu, hep-th/0212259; J.L. Hewett, F.J. Petriello, and T.G. Rizzo, Phys. Rev. D **66**, 036001 (2002).

[4] M.S. Berger and V.A. Kostelecký, Phys. Rev. D **65**, 091701(R) (2002).

[5] O.W. Greenberg, Phys. Rev. Lett. **89**, 231602 (2002); hep-ph/0305276.

[6] For recent overviews of various experimental and theoretical approaches to Lorentz and CPT violation, see, for example, V.A. Kostelecký, ed., *CPT and Lorentz Symmetry II*, World Scientific, Singapore, 2002.

9

[7] D. Colladay and V.A. Kostelecký, Phys. Rev. D **55**, 6760 (1997); **58**, 116002 (1998).

[8] V.W. Hughes, H.G. Robinson, and V. Beltran-Lopez, Phys. Rev. Lett. **4** (1960) 342; R.W.P. Drever, Philos. Mag. **6** (1961) 683; J.D. Prestage *et al.*, Phys. Rev. Lett. **54** (1985) 2387; S.K. Lamoreaux *et al.*, Phys. Rev. A **39** (1989) 1082; T.E. Chupp *et al.*, Phys. Rev. Lett. **63** (1989) 1541.

[9] C.J. Berglund *et al.*, Phys. Rev. Lett. **75** (1995) 1879; L.R. Hunter *et al.*, in V.A. Kostelecký, ed., *CPT and Lorentz Symmetry,* World Scientific, Singapore, 1999.

[10] D. Bear *et al.*, Phys. Rev. Lett. **85**, 5038 (2000).

[11] D.F. Phillips *et al.*, Phys. Rev. D **63**, 111101 (2001); M.A. Humphrey *et al.*, physics/0103068; Phys. Rev. A **62**, 063405 (2000).

[12] V.A. Kostelecký and C.D. Lane, Phys. Rev. D **60**, 116010 (1999); J. Math. Phys. **40**, 6245 (1999).

[13] R. Bluhm *et al.*, Phys. Rev. Lett. **88**, 090801 (2002).

[14] R. Bluhm *et al.*, hep-ph/0306190.

[15] J. Lipa *et al.*, Phys. Rev. Lett. **90**, 060403 (2003).

[16] H. Müller *et al.*, physics/0305117.

[17] S.M. Carroll, G.B. Field, and R. Jackiw, Phys. Rev. D **41**, 1231 (1990); V.A. Kostelecký and M. Mewes, Phys. Rev. Lett. **87**, 251304 (2001).

[18] R. Jackiw and V.A. Kostelecký, Phys. Rev. Lett. **82**, 3572 (1999); C. Adam and F.R. Klinkhamer, Nucl. Phys. B **657**, 214 (2003); H. Müller, C. Braxmaier, S. Herrmann, A. Peters, and C. Lämmerzahl, Phys. Rev. D **67**, 056006 (2003); T. Jacobson, S. Liberati, and D. Mattingly, hep-ph/0209264; V.A. Kostelecký, M. Perry, and R. Lehnert, astro-ph/0212003; V.A. Kostelecký and A.G.M. Pickering, Phys. Rev. Lett., in press (hep-ph/0212382); R. Lehnert, gr-qc/0304013; G.M. Shore, gr-qc/0304059.

[19] V.A. Kostelecký and M. Mewes, Phys. Rev. D **66**, 056005 (2002).

[20] KTeV Collaboration, H. Nguyen, in Ref. [6]; OPAL Collaboration, R. Ackerstaff *et al.*, Z. Phys. C **76**, 401 (1997); DELPHI Collaboration, M. Feindt *et al.*, preprint DELPHI 97-98 CONF 80 (1997); BELLE Collaboration, K. Abe *et al.*, Phys. Rev. Lett. **86**, 3228 (2001); BaBar Collaboration, B. Aubert *et al.*, hep-ex/0303043; FOCUS Collaboration, J.M. Link *et al.*, Phys. Lett. B **556**, 7 (2003).

10

[21] V.A. Kostelecký and R. Potting, Phys. Rev. D **51**, 3923 (1995); D. Colladay and V.A. Kostelecký, Phys. Lett. B **344**, 259 (1995); Phys. Rev. D **52**, 6224 (1995); Phys. Lett. B **511**, 209 (2001); V.A. Kostelecký and R. Van Kooten, Phys. Rev. D **54**, 5585 (1996); O. Bertolami *et al.*, Phys. Lett. B **395**, 178 (1997); V.A. Kostelecký, Phys. Rev. Lett. **80**, 1818 (1998); Phys. Rev. D **61**, 016002 (2000); **64**, 076001 (2001); N. Isgur *et al.*, Phys. Lett. B **515**, 333 (2001).

[22] V.W. Hughes *et al.*, Phys. Rev. Lett. **87**, 111804 (2001); R. Bluhm *et al.*, Phys. Rev. Lett. **84**, 1098 (2000).

[23] H. Dehmelt *et al.*, Phys. Rev. Lett. **83**, 4694 (1999); R. Mittleman *et al.*, Phys. Rev. Lett. **83**, 2116 (1999); G. Gabrielse *et al.*, Phys. Rev. Lett. **82**, 3198 (1999); R. Bluhm *et al.*, Phys. Rev. Lett. **82**, 2254 (1999); Phys. Rev. Lett. **79**, 1432 (1997); Phys. Rev. D **57**, 3932 (1998).

[24] B. Heckel, in Ref. [6]; L.-S. Hou, W.-T. Ni, and Y.-C.M. Li, Phys. Rev. Lett. **90**, 201101 (2003); R. Bluhm and V.A. Kostelecký, Phys. Rev. Lett. **84**, 1381 (2000).

[25] P. Laurent *et al.*, Eur. Phys. J. D **3** (1998) 201.

[26] N. Ashby, in Ref. [6].

[27] C. Fertig *et al.*, Proceedings of the Workshop on Fundamental Physics in Space, Solvang, June 2000; and in Ref. [6].

[28] S. Buchman *et al.*, Adv. Space Res. **25**, 1251 (2000); J. Nissen *et al.*, in Ref. [6].

[29] V.A. Kostelecký and R. Lehnert, Phys. Rev. D **63**, 065008 (2001); V.A. Kostelecký, C.D. Lane, and A.G.M. Pickering, Phys. Rev. D **65**, 056006 (2002).

[30] C. Lämmerzahl *el al.*, Class. Quant. Gravity **18**, 2499 (2001).

11

Prospects for an Improved Measurement or Experimental Limit on *G-dot*

Alvin J. Sanders
Department of Physics and Astronomy,
University of Tennessee,
Knoxville, TN 37996-1200, U.S.A.,
and
Engineering Science and Technology Division
Oak Ridge National Laboratory
PO Box 2008
Building 5800, Mail Stop 6054
Oak Ridge, TN 37831-6054
E-mail: ASanders@utk.edu

ABSTRACT

The orbital motion of an ultra-drag-free satellite, such as the large test body of the SEE (Satellite Energy Exchange) satellite, known as the "Shepherd," may possibly provide the best test for time variation of the gravitational constant G at the level of parts in 10^{14}. Scarcely anything could be more significant scientifically than the incontestable discovery that a fundamental "constant" of Nature is not constant. A finding of non-zero *(G-dot)/G* would clearly mark the boundaries where general relativity is valid, and specify the onset of new physics. The requirements for measuring *G-dot* at the level proposed by SEE will require great care in treating perturbation forces. In the present paper we concentrate on the methods for dealing with the gravitational field due to possible large manufacturing defects in the SEE observatory. We find that, with adequate modeling of the perturbation forces and cancellation methods, the effective time-averaged acceleration on the SEE Shepherd will be $\sim 10^{-18}$ *g* (10^{-17} m/s^2).

1. Introduction

A thorough understanding of the gravitational force—especially a satisfactory quantum theory of gravity—is the missing link in efforts to achieve a satisfactory unification theory. The question of whether the gravitational constant G is truly constant or whether it might be time-varying is of particular importance to modern theories of gravitation and, hence, to efforts to achieve a satisfactory unification theory. A striking feature of recent theories of quantum gravity and string theory is that they cannot retain a constant G, but rather require various secular rates of change. Their predictions of *(G-dot)/G* are typically $\sim 10^{-13}$/yr to $\sim 10^{-11}$/yr. Moreover, a test of *(G-dot)/G* is one of the very few ways of discriminating among various modern theories [see, for example, Marciano, 1984; Bronnikov, Ivashchuk & Melnikov, 1988; Melnikov, 1994; Drinkwater *et al*. 1999; and Ivashchuk & Melnikov, 2000].

It was of course Dirac's original conjecture about variation of the fundamental constants, summarized in his "Large Numbers Hypothesis," that opened the door to initial speculations in this area, and his original concept of two metrics (one for "mechanical," *i.e*., orbital processes and another for "atomic" processes) still echoes today in the theories discussing extra dimensions. By roughly mid-century, the scalar-tensor theories of gravity were essentially the first to make

87

quantitative predictions of a non-zero *(G-dot)/G*. The essential feature was that the gravitational field would have a secular change . Such theories, particularly that of Brans and Dicke, were hotly debated within the context of general relativity, and eventually gave way to increasingly precise experimental confirmations of general relativistic predictions. However, perhaps the most striking thing about the debate at that point in time was that a non-zero *(G-dot)/G* lay outside of the predictions of general relativity; hence, if some evidence for it could be discovered, then Einsteinian geometrodynamics would be incomplete, at best.

Although a number of different theoretical models have subsequently been proposed, experimental/observational evidence is still not sufficiently precise to discriminate among the predictions of different theories with respect to *G-dot* and other variables and, hence, to assess the validity of alternative models.

The question of the variability of *G* has taken on increasing urgency in recent years. One important new motivation for the measurement of *(G-dot)/G* has arisen within the context of attempts to reveal the presence of a dynamical background energy in the universe, the so-called "dark energy" or quintessence." Chiba (1999), for instance, has pointed out that a dynamical coupling of the quintessence field to the gravitational field can give rise to a *(G-dot)/G* effect, and he has used the existing experimental values to constrain the size of such a coupling. For a review, see Uzan (2003).

The best tests of *G-dot* at present are observational tests from Lunar Laser Ranging (LLR). The basic approach of LLR analysis is to disentangle a number of different effects—Newtonian, Einsteinian, and putative post-Einsteinian—relating to the motion of the Moon in search of putative post-Einsteinian effects, such as the Nordtvedt effect, other Universal Free Fall violations, and non-zero G-dot [Nordtvedt, 1996, 2002, & 2003]. To date no violations have been found. The present limit on *G-dot* is $\sim 10^{-12}$/yr [Pitjeva, 1997; Williams *et al.*, 2001; Williams *et al.*, in press].

There is now reason to believe that the orbital motion of a near-Earth satellite can be made so nearly drag free by design that it may effectively play the role of the Moon and provide a test for time variation of the gravitational constant *G* at the level of parts in 10^{14}—about two orders of magnitude beyond both the current observational results and the predictions of most current theories. To wit, we believe that the large test body of the SEE (Satellite Energy Exchange) satellite [Sanders & Deeds, 1992 and 1993, and Sanders *et al.*, 1993, and Sanders & Gillies 1998a], known as the "Shepherd," could play this role. The methods for a test of *G-dot* by SEE are closely analogous to those of LLR, with the notable exception that LLR is entirely *observational*, while the use of a drag-free artificial satellite essentially comprises a *controlled experiment* with very fine accuracy.

There has never been a credible laboratory measurement of *(G-dot)/G* (using test masses in a controlled situation) at cosmologically interesting levels of precision. Although there have been perhaps a dozen laboratory experiments proposed to measure *(G-dot)/G*, none of them has been successfully carried out at cosmologically significant levels of interest. The existing data through 1997 are reviewed by Gillies (1997).

In short, it would be very significant scientifically to discover that a fundamental "constant" of Nature is not constant. Nothing could do more to invigorate interest in new theories, most of which do allow for time variation of *G* and other fundamental "constants." A finding of non-zero *(G-dot)/G* would of course require modification of general relativity, since it assumes a constant value of *G*. More broadly, this would clearly mark the boundaries where general relativity is valid, and specify the onset of new physics. The very precise *experimental* data to be provided by a SEE mission augurs for significant advances in gravitation theory, with concordant implications for unification theory.

3. Experimental method for determining *(G-dot)/G* on the SEE mission

The experimental approach to measuring *(G-dot)/G* by a SEE mission is described in a previous article [Sanders *et al.*, 2000]. The main idea is to use the orbital period as a clock running in comparison with atomic clocks and to infer a possible change in *G* from the dependence of the period on *G*. Thus, unless the orbital period is constant except for various known and/or characterizeable perturbations, *G* will be shown to be changing (strictly speaking, we can look only for changes in the product M_EG). We have shown that the accuracy with which *(G-dot)/G* may be measured is limited by (1) available position resolution if the observation time is less than one year and (2) accuracy in accounting for perturbations if the observation time is greater than one year [Sanders *et al.*, 2000]. The capability for measuring time will not be a limiting factor in measuring *(G-dot)/G*, assuming the next generation of atomic clocks is available.

## 4. Expected Error Budget for *G-dot* Determination by SEE

Great caution is required in satellite design to make the Shepherd as nearly drag-free as possible. The various perturbing effects that are thought to have the potential to contribute to error in the measurement of *G*–dot on a SEE mission are being evaluated. The status of this evaluation is shown in Table 1 [after Sanders *et al.*, 2000].

Table 3. Error Budget for *G*-dot (One-Year and Four-Year Observation Periods)

Error Source	Average Force $(\times 10^{-17}$ N)	$\delta(G\text{-dot}/G)$ $(\times 10^{-15})$		Brief Comments (details below)
		1 yr	4 yrs	
Tracking error	NA	15.6	2.0	GPS/SLR accuracy = 1 cm
Timekeeping error	NA	~1	~1	Next generation clocks
Blackbody radiation	10.0	8.6	4.3	$\Delta\Theta < 0.1$ mK
Electrostatic forces	<15	<10	<5	Surface potential < 6.4 mV
Lorentz forces	small	zero	zero	Perpendicular to velocity
Earth's field	<1.4	<0.9	<0.5	With GRACE or equivalent
Capsule mass defects	22.2	15	7.4	Many defects ~10 mg
Gravity of particle	<0.22	<0.15	<0.08	Newton's 3rd law
Shepherd's moments	small	small?	small?	Not evaluated yet
Outgassing jets	small	small	small	Obviate by baking
Total	**NA**	**25**	**10**	

The *(G-dot)/G* error budget is summarized by Figure 1 below. The top row from Table 1 (tracking error) appears in Figure 1 as a line that decreases as $t^{-3/2}$. The second row (timekeeping) appears as the horizontal line at 10^{-15}/yr. The collective effect of all other items in Table 1 appears in Figure 1as the line that decreases as $t^{-1/2}$. The total error in Figure 1 is shown as the hyperbola-like curve, which exceeds 10^{-13}/yr if the observation time is a few months, and which falls below 10^{-14}/yr when the observation time is more than 4 years.

Figure 1 .
Error Budget for *G/G*
by Class of Source

Log(observation time in sec)
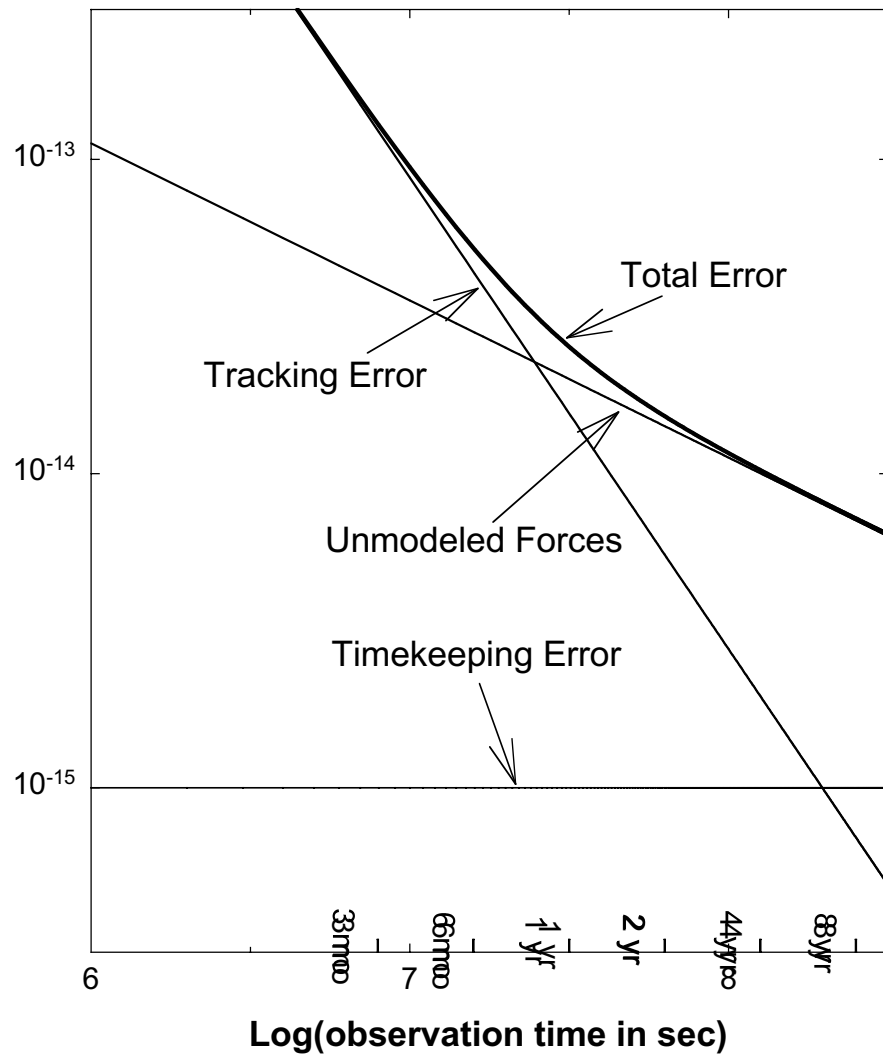
5. Perturbations--Internal Gravitational Field of SEE Observatory

In this section we focus on the effects due to the gravitational field of the SEE observatory itself. The original article on SEE pointed out that it is possible, in principle, to distribute the mass of any closed container such that the gravitational field on the interior is zero [Sanders & Deeds, 1992; U.S. Patent No. 5,427,335, June 27, 1995]. In practice, the desired distribution cannot of course be realized exactly, and it is therefore necessary to develop strategies to cope with the "mass defects"

which will inevitably exist [Sanders & Gillies, 1996a; Sanders & Gillies, 1996a; Sanders & Gillies, 1996b; Sanders & Gillies, 1997; Sanders & Gillies, 1998b]. We have previously investigated the perturbations due to a large number of small, randomly-located point-like mass defects in the side walls of the SEE experimental chamber [Corcovilos & Gadfort, 1998; Sanders *et al.*, 1999 and Sanders *et al.*, 2000]. In the present paper we consider the perturbation due to a single large mass defect in the end wall of the SEE experimental chamber.

Detailed simulations are of course required to validate data-reduction methods for disentangling the effects of various combinations of mass defects. The original SEE paper pointed out that a Fourier-Bessel expansion of the potential was suitable for this purpose [Sanders & Deeds, 1992], and we subsequently presented the explicit form of the off-axis coefficients [Antonov, 1999]. The role of the spatial Fourier spectrum for treating the potential on axis is illustrated in Sanders *et al.* (1999).

Although comprehensive approaches such as these will be required for reducing the data from the actual mission, elementary calculations of special cases are very helpful for providing insight into the meaning of comprehensive treatments. In this section we consider one such special case—extra mass at one end of the experimental chamber—and we carry out elementary calculations to illustrate the impact on the *G*-dot determination.

It is necessary to distinguish among three stages in the treatment of perturbations due to mass defects:
  (A) How large the mass-defect perturbations actually are. This is essentially an issue of manufacturing tolerances.
  (B) How accurately these perturbations can be *modeled* or mapped, We treat this under the heading of "self calibration" in Sanders & Gillies (1996). The error in this modeling is called the "unmodeled force."
  (C) The extent to which the effects of mass defects can be *canceled*, by varying the orientation of the capsule and the position of the Shepherd, and then averaging over these different configurations. The departure from perfect cancellation is called the "uncanceled force."

These distinctions are discussed in Sanders *et al.* (2000) in the sections titled "The drag-free satellite concept." The concept of Almost-Zero Time-Averaged Drag (AZTAD) satellites, introduced here, is central to SEE's *G*-dot determination.

We now demonstrate that a very large defect will not be deleterious, provided the SEE observatory is *calibrated* ("B" above) and the *unmodeled* force is further suppressed by the *cancellation* methods ("C" above).

For this illustration we suppose that the thickness defect in one endplate of the observatory chamber is manufactured 50 microns too thick (an enormous error!). We trace the implications of this mass defect as if the chamber were otherwise perfectly manufactured (*i.e.*, the SEE observatory would have zero internal field if the thickness of the endplate were correct). The distance of the Shepherd from the heavier endplate is typically ~1 m, so it will experience a perturbation force of about

$$F = GMm/r^2 \cong 1.4 \times 10^{-9} \text{ N}$$

Here we have taken the radius of the endplate as 50 cm and its density as 2700 kg/m^3, so the mass defect *m* is 106 g. We take the mass of the Shepherd as *M*=200 kg.

This perturbative force will of course be in the *forward* direction when the heavy end is in the front end of the observatory, and the force will point *backward* when the heavy end is in the back. In

either case, the force can be measured by observing the relative motion of the Shepherd and a Particle. The *relative* acceleration of the Shepherd and Particle will be greater when the Shepherd is near the heavy endplate than when it is near the "good" endplate. From observations of such differences, the potential field of the SEE observatory can be mapped. For simplicity we assume that the Particle is located far from either end, so that the interaction between the Particle and the endplate defect may be neglected.

When the Shepherd is near the "heavy" endplate, it experiences an additional acceleration of $F/M \cong$ 7.0×10^{-12} m/s^2 that does not occur when it is near the "good" endplate. Therefore the size of the net impact of the perturbation during a four-hour observation, may be roughly estimated as a differential displacement equal to

$$1/2 \ a \ t^2 = 7.2 \times 10^{-4} \ m$$

when the Shepherd is near the heavy endplate.

Such a large difference (0.72 mm) would of course be an obvious effect. The question is, just how accurately can it be measured? This will determine *how accurately* the potential field of the capsule can be mapped (modeled). The SEE experimental design calls for the measurement accuracy of the relative positions of the test bodies to be known to less than a micron. A 1-micron difference in, say, four hours of observation (two orbital revolution) corresponds to an acceleration difference δa equal to 1×10^{-14} m/s^2 (*i.e.*, $1/2 \ \delta a \ t^2 = 1 \times 10^{-6}$ m). In turn, this corresponds to a 70-nm error in the thickness of the end wall. That is, an additional 70 nm (150 mg) in the end wall would cause the test-body separation to increase or decrease by an additional 1 micron, which is large enough to be measurable. Thus, the ability to detect test-body positions to <1 micron is equivalent to being sensitive to a thickness difference between the two end walls with a resolution of <70 nanometers on the basis of observation of the Particle and Shepherd for four hours near the heavy end and four hours near the good end.

The above calculations demonstrates that—remarkably—although the defect in the end-wall thickness may be very large (50 microns), the resulting difference in the potential may be detected with a resolution equivalent to ~70 nm in endplate thickness.

Moreover, we note that this result is *not a function of the size of the defect*. The reader may easily demonstrate this fact by repeating the above algebra with a different assumption about the manufacturing defect (for example, a 5-micron or 500-micron error in thickness); the result will be that the detection resolution would be unchanged (still ~70 nm).

The discussion to this point entails effects of modeling (mapping, calibrating) of the perturbation forces, *not* cancellation.

Cancellation procedures can result in a further dramatic reduction in the actual time-averaged force on the Shepherd, which is what affects the *G*-dot measurement. Here is the cancellation procedure: Consider the axial component of the un-modeled force along any line parallel to the axis of the SEE observatory. This function may be of course decomposed into the sum of two functions—one even and one odd—and the choice of origin is arbitrary. For any two points located symmetrically with respect to the origin, signs of the odd part of the force are opposite, while those of the even part are the same. To say that the sign of the even part remains the same means that, if the even force on a test body is *forward* when it is in one end of the capsule, then the force will also be forward when the test body is in the opposite end of the capsule. Now, if the capsule is "flipped"—turned 180 degrees, so that the back end becomes the front end—this force will reverse direction: the even force on the test body will now be *backwards* (in both ends of the capsule). The odd part of the

force of course still switches sign when the Shepherd moves from one end of the capsule to the other, regardless of the orientation of the observatory. We apply these simple principles to the SEE Shepherd. The two orientations of the SEE observatory and the two positions of the test body yield "Four Flight Configurations" here. The cartoon figure below illustrates the four configurations.

Figure 2
The Four Flight Configurations
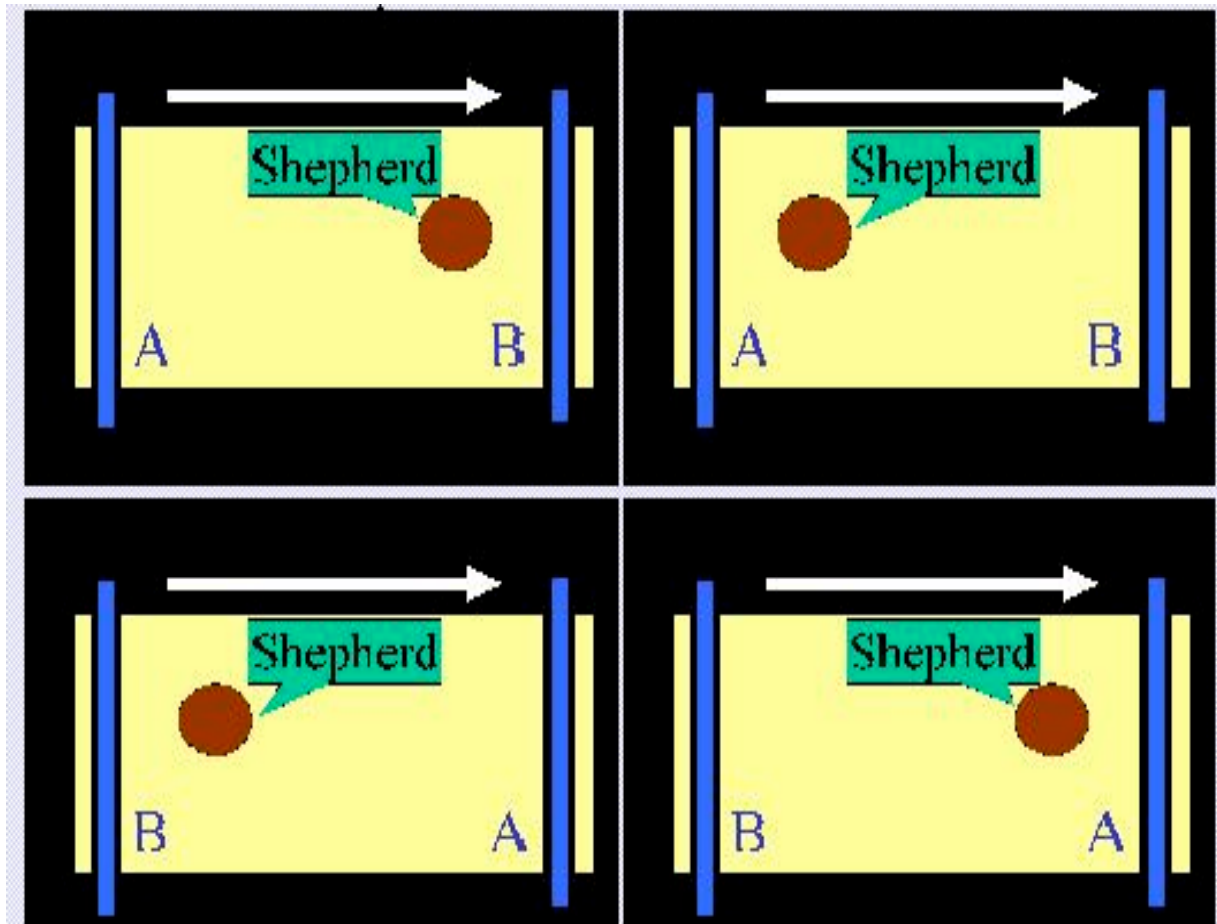
Obviously the sum of the even and odd forces over the Four Flight Configurations is exactly zero. In practice it will not be possible to control the position of the Shepherd exactly, so the two positions will not be quite symmetrically located with respect to the origin. We estimate that it will be easy to control the Shepherd to within a centimeter at all times and to control its *average* position to within a millimeter.

A point of secondary importance is that the Shepherd may be intentionally moved about over a "roaming interval" ~1 or 2 meters in length. There are a number of reasons why this procedure would be more desirable than trying to pin it to a single location at each end. One important benefit of the roaming-interval approach is that it avoids the possibility of accidentally choosing the location at a point where the un-modeled force is changing rapidly. That is, the roaming approach averages over such sensitive locations and less-sensitive locations.

We have previously shown that the time-averaged force on the Shepherd will typically be ~3 orders of magnitude smaller than the un-modeled force, assuming the average position of the Shepherd can be controlled to within a few millimeters [Sanders *et al.*, 1999 and Sanders *et al.*, 2000]. This result was for the case of a large number of small point-mass defects in the walls of the SEE observatory. We now demonstrate that the same cancellation technique is also effective in the case of a large mass defect in the end wall.

The Shepherd will be maneuvered so that it spends equal times in the two Flight Configurations that locate it near the "heavy" endplate, and also equal times in the other two Flight Configurations, in which the Shepherd is near the "good" end of the chamber.

As indicated above, if the mass defect is *m*=106 g, the resulting perturbation would be about

$$F \cong GMm/r^2 \cong 1.4\text{X}10^{-9} \text{ N}$$

This is the approximate **actual perturbation force**.

We would observe this by seeing that the relative acceleration of the two test bodies would be greater when the Shepherd were closer to the "heavy end of the capsule. However, we demonstrated above that, as a consequence of limitations in position-measurement capability, we would make an error in modeling this force that is equivalent to a mass defect of $\delta m \sim 150$ mg (thickness ~70 nm thickness). Therefore, the error in the force map would be

$$\delta F = G M \delta m/r^2 \cong 2\text{x}10^{-12} \text{ N}$$

This is the **un-modeled force** (error in the force calibration).

Now comes the cancellation: The un-modeled force error will be in the *forward* direction in two flight configurations and in the *backward* direction in the other two flight configurations. The time average, taken over all Four Flight Configurations, is exact cancellation in principle. The cancellation will not be exact in practice because the effective distance *r* of the Shepherd from the mass defect cannot be controlled exactly. We assume that the average positioning error is 1 mm (a large value compared with the accuracy of the measurement system). Thus, if *r*~1 m, we choose

r_1=1.000 m and r_2=1.001 m. Therefore the *difference* between the resulting forces, as computed from the force map, is two or three orders of magnitude smaller than the un-modeled force, namely:

$$\delta F_1 - \delta F_2 \; = \; G \, M \, \delta m \, x \, (1/r_1^2 - 1/r_2^2) \cong 4 \times 10^{-15} \text{ N}$$

This is the **un-cancelled force**.

The corresponding un-cancelled acceleration is obtained by dividing out the Shepherd mass, M (200 kg). The result is

$$a \cong 2 \times 10^{-17} \text{ m/s}^2 \cong 2 \times 10^{-18} \text{ g}$$

That is, the time-averaged drag on the Shepherd is $\sim 10^{-18}$ g, *ceteris paribus*.

To avoid misunderstanding, we must emphasize that the above is only a series of illustrative elementary calculations about a *single* mass defect, *viz.* a defect in the thickness of one end wall. This approach is useful for obtaining order-of-magnitude results, but it is no substitute for a comprehensive analysis of the combined impact of multiple mass defects, including large numbers of randomly distributed mass defects, as described in Sanders *et al.* (1999). Our results for multiple mass defects are summarized in Figure 3 of Sanders *et al.* (1999) and the accompanying text.

6. Summary

These results, plus the calculation above of the impacts of a single large defect, show that time-averaged force on the Shepherd will be remarkably small, given proper treatment of the perturbations, even if the perturbations are relatively large. This is a major accomplishment under our NASA Fundamental Physics in Microgravity grant. We regard it as an important advance in experimental gravitation.

7. Discussion in Q&A Period

Question (Ho-Jung Paik): Since the unmodeled force on the Shepherd due to mass defects is constant—has no time variation—how can it have a random-walk character? How can this contribution to the total unmodeled force continue to decrease with time [as $t^{-1/2}$], as shown in Figure 1?

Answer (during session): I believe you are correct.

Later answer: Although it is true in principle that the force *at any given point in the experimental chamber* due to mass defects is not time-varying, the Shepherd will not be located at exactly the intended positions (if it were, then exact cancellation would result, so the time-averaged force would indeed be constant—in fact, zero). Rather, the actual force on the Shepherd will be time-varying because of positioning errors, and this effect is correctly described by a random walk, so the force will vary as $t^{-1/2}$, as shown in Figure 1.

Acknowledgments

Physics in Microgravity Program, NASA Marshall Space Flight Center, and NASA Jet Propulsion Laboratory.

References

Vassil Antonov, "Fourier Coefficients of the Gravitational Potential and Perturbation Forces due to Capsule Mass Defects in Project SEE," University of Tennessee/Oak Ridge National Laboratory internal report, UT Center of Excellence Science Alliance (28 July 1999).

K.A. Bronnikov, V.D. Ivashchuk and V.N. Melnikov; *Nuovo Cim. B* **102**, 209 (1988).

T. Chiba, "Quintessence, the gravitational constant, and gravity," *Phys. Rev. D* **60**, 083508 (1999).

T. Chiba, "Constancy of the Constants of Nature," gr-qc/0110118 (October, 2001).

T.A. Corcovilos & Gadfort T, 1998. "Issue-scoping for Project SEE"; University of Tennessee Technical Report (August 1998).

M. Drinkwater *et al*. MNRAS, 1999, November 1999, astro-ph/9711290.

G.T. Gillies, "The Newtonian gravitational constant: Recent measurements and related studies"; *Reports on Progress in Physics* **60**, 151-225 (1997).

V.D. Ivashchuk and V.N. Melnikov. In : Lecture Notes in Physics, v. 537. *Mathematical and Quantum Aspects of Relativity and Cosmology.* Springer, 2000, p. 214.

V.D. Ivashchuk and V.N. Melnikov, "Multidimensional p-brane Cosmological Models and Billiard Behaviour," In *Proc. 2nd ICRA Network Workshop "The Chaotic Universe"*, World Scientific, Singapore (2000).

W.J. Marcino, "Time variation of the fundamental 'constants' and Kaluza-Klein theories," *Phys. Rev. Lett.* **52**, 489-491 (1984).

V.N. Melnikov, "Fundamental physical constants and their stability," *Int. J. Theor. Phys.* **33** (No. 7), 1569-1579 (1994).

Kenneth Nordtvedt , "Lunar Laser Ranging--a comprehensive probe of post-Newtonian gravity," gr-qc/0301024, for proceedings of Villa Mondragone International School of Gravitation and Cosmology, September, 2002 (2003).

Kenneth Nordtvedt, "Space-Time Variation of Physical Constants and the Equivalence Principle," gr-qc/0212044 (2002).

Kenneth Nordtvedt, "From Newton's moon to Einstein's moon," *Phys. Today* **49** (No. 5), 26-31 (May 1996).

E.V. Pitjeva, In: *Dynamics and Astrometry of Natural and Artificial Celestial Bodies*, Ed. I.M. Wytryszczak, J.H. Lieske and R.A. Feldman (ISBN 0-7923-4574-6) Kluwer Acad. Publ., Dordrecht, Netherlands, 1997, p. 251.

A.J. Sanders, A.D. Alexeev, S.W. Allison, K.A. Bronnikov, J.W. Campbell, M.R. Cates, T.A. Corcovilos, D.D. Earl, T. Gadfort, G.T. Gillies, M.J. Harris, N.I. Kolosnitsyn, M.Yu. Konstantinov, V.N. Melnikov, R.J. Newby, R.G. Schunk, and L.L. Smalley, "Project SEE (Satellite Energy

Exchange): Proposal for Space-based Gravitational Measurements," at the conference The Gravitational Constant: Theory and Experiment 200 Years after Cavendish, November 23-24, 1998, London; published in *Meas. Sci. Technol.* **10** (No. 6), 514-524 (1999).

A.J. Sanders, A.D. Alexeev, S.W. Allison, V. Antonov, K.A. Bronnikov, J.W. Campbell, M.R. Cates, T.A. Corcovilos, D.D. Earl, T. Gadfort, G.T. Gillies, M.J. Harris, N.I. Kolosnitsyn, V.N. Melnikov, R.J. Newby, R.G. Schunk, and L.L. Smalley, "Project SEE (Satellite Energy Exchange): an international effort to develop a space-based mission for precise measurements of gravitation". *Class. Quant. Grav.* **17** (No. 12), 2331-2346 (2000).

Alvin J. Sanders and W. Edward Deeds, "Proposed New Determination of the Gravitational Constant *G* and Tests of Newtonian Gravitation," *Phys. Rev. D.* **46** (No. 2), 489-505 (1992).

Alvin J. Sanders and W. Edward Deeds, "Reply to 'Perturbative Forces in the Proposed Satellite Energy Exchange Experiment'," *Phys. Rev. D.* **47** (No. 8), 3660-3661 (1993).

Alvin J. Sanders, W. Edward Deeds and George T. Gillies, "Proposed New Space-Based Method for More Accurate Gravitational Measurements," in *The Earth and the Universe: Festschrift für Prof. Hans-Jürgen Treder* [retiring as editor of *Annalen der Physik*], edited by Wolfgang Schröder (Bremen, 1993).

Alvin J. Sanders and George T. Gillies, "A Comparative Study of Proposals for Space-Based Determination of the Gravitational Constant *G*," *Rivista del Nuovo Cimento*, **19** (No. 2), 1-54 (1996).

Alvin J. Sanders and George T. Gillies, "Comparison of Proposals for Space-Based Determination of *G*," *Gravitation and Cosmology* **2** (No. 1) 57-60 (1996) (in English and Russian).

A.J. Sanders and G. T. Gillies, "A comparative survey of proposals for space-based determination of the gravitational constant *G*"; *Proc. SPIE* **3116**, 88-96, Small Spacecraft, Space Environments, and Instrumentation Technologies, Oct. 1997.

A.J. Sanders and G.T. Gillies, "Project SEE (Satellite Energy Exchange): Proposed Space-Based Method for More Accurate Gravitational Measurements," in Bergmann, P. G., de Sabbata, V., Gillies, G. T., and Pronin, P. I., eds., *Spin in Gravity: Is it Possible to Give an Experimental Basis to Torsion?* (International School of Cosmology and Gravitation XVth Course), The Science and Culture Series - Physics, No. 16 (World Scientific, Singapore, 1998), pp. 225-230.

A.J. Sanders and G.T. Gillies, "A Comparative Survey of Proposals for Space-Based Determination of the Gravitational Constant *G*," *Loc. cit.,* pp. 231-234.

Jean-Philippe Uzan, "The fundamental constants and their variation: observational and theoretical status" *Rev. Mod. Phys.* **75** (No. 2), 345-712 (April 2003).

J.G. Williams, D.H. Boggs, J.O. Dickey, and W.M. Folkner, "Lunar Laser Tests of Gravitational Physics," *Proceedings of Ninth Marcel Grossmann Meeting*, World Scientific Publ., Ed. R. Jantzen, web version posted 2001, paper version in press.

J.G. Williams, J.D. Anderson, D.H. Boggs, E.L. Lau, and J.O. Dickey, "Solar System Tests for Changing Gravity," Amer. Astron. Soc., Pasadena, CA, June 3-7, 2001, *Bulletin of the American Astronomical Society* **33** 836 (2001).